Ice/hydrology feedback in the Siple Coast, Antarctica, from two-way coupled modeling

by

Koi McArthur

A thesis
presented to the University of Waterloo
in fulfilment of the
thesis requirement for the degree of
Master of Mathematics
in
Applied Mathematics

Waterloo, Ontario, Canada, 2024

Author's Declaration

I hereby declare that I am the sole author of this thesis. This is a true copy of the thesis, including any required final revisions, as accepted by my examiners.

I understand that my thesis may be made electronically available to the public.

Abstract

Subglacial hydrological processes have long been understood to play a critical role in ice dynamics (Budd et al., 1979). Consequently, the recent emergence of complex two-dimensional subglacial hydrology models with both inefficient and efficient drainage components has led to two-way coupling of these complex hydrology models to ice flow models (Cook et al., 2022). Such two-way coupled models bring about questions regarding our implementation of friction in ice flow models and allow us to examine feedback mechanisms between the subglacial hydrological system and the ice sheet. This thesis investigates feedback mechanisms between the subglacial hydrological system and the ice sheet, and analyzes our current implementation of friction in ice flow models. This is accomplished through subglacial hydrology, ice flow, and coupled modeling of the Siple Coast of West Antarctica, which has a history of observable hydrology/ice flow feedback.

We use the Glacier Drainage System (Werder et al., 2013, GlaDS) model as a subglacial hydrology model, and the Shallow Shelf Approximation (Larour et al., 2012, SSA) with a mass transport model as an ice flow model, both of which are implemented in the Ice-Sheet and Sea-Level Systems Model (Larour et al., 2012, ISSM). We model the steady state subglacial hydrology of the Ross Sea subglacial hydrologic catchment, along with ice flow and two-way coupled ice flow/hydrology from 2010-2100 using an SSP585 surface mass balance forcing scenario. We test three different friction laws – the Budd friction law, the Schoof friction law, and a version of the Schoof friction law that we modify to ensure the sliding regime is representative of the cavitation at the glacier bed. Additionally, we test coupling with variable melt from frictional heating of ice, coupling with subglacial lake geometry altering glacier driving stress, and coupling with a combination of the two.

The effective pressure and the modeled sliding regime were found to be largely responsible for the evolution of fast flowing regions of the domain, highlighting the importance of two-way coupled models, which have a cavitation-dependent sliding regime. Feedback mechanisms between the subglacial hydrologic system and the ice sheet were identified, including a negative feedback mechanism that stabilized the basal shear stress and the effective pressure fields when variable melt was available to the subglacial hydrologic system. The inclusion of subglacial lake geometry on the glacier driving stress was found to have a large control on lake depth, with the potential for large speedup events corresponding to the fast filling of subglacial lakes. When all coupling components were active, a negative feedback mechanism between subglacial lake depth, glacier driving stress, and melt water production, which stabilized subglacial lake depth and ice motion was observed.

The methods developed in this thesis and the limitations that we discovered for implementing subglacial processes in ice flow models will be highly valuable to the glaciological

modeling community moving forwards.

Acknowledgements

A big thanks to my supervisor Dr. Christine Dow, only with your supervision the work presented here is possible. You troubleshot problems with me, gave me opportunities to go to conferences and help with field work, kept my degree on track, and edited my work. Thank you for making this degree such an enjoyable experience!

I would like to thank Dr. Marek Stastna for supervising me at the start of my degree, and for giving me valuable instruction on how to succeed in a post graduate program. Every time I took a class from you I gained a better understanding of how to be a researcher.

Thank you Dr. Shivani Ehrenfeucht for troubleshooting modeling issues with me, and for supplying me with example code on how to run two-way coupled models in ISSM. Thank you for attending weekly meetings to help keep my progress in the right direction.

Dr. Felicity McCormack gave me example code to run inversions in ISSM, and was there to bounce ideas off of for my new friction law. I am very grateful for your help.

I would like to acknowledge Dr. Francis Poulin for letting me go to EGU 2023 and not mark any final exams, and Dr. Hans De Sterck for allowing me to write my final remotely in Vienna.

I would like to thank Dr. Mathieu Morlighem for giving me advice for altering ISSM source code, and showing me how to submit changes to the ISSM developer branch.

I would like to thank the Ontario Government for the OGS funding, and the University of Waterloo for additional funding, this funding allowed me to have a larger focus on my research.

Table of Contents

List of Figures

List of Tables

Chapter 1

Introduction

Large ice masses known as glaciers and ice sheets store 68.7 % of the world's fresh water (Shiklomanov, 1993). As these ice bodies lose mass in a warming climate, contributing to global sea level rise (Frederikse et al., 2020), it is important to understand the processes behind this mass loss. Glaciers contribute to sea level rise by two mechanisms: annual surface and basal melt which exceeds accumulation, and increased ice motion and discharge into the ocean, which displaces ocean water. While it is clear that higher air temperature leads to more surface melt resulting in a direct contribution to sea level rise, it is more difficult to understand the processes involved with glacier dynamics and hence the affect of a changing climate on ice motion.

Glaciers and ice sheets move through deforming under their own weight, sliding at their base, and deformation of their underlying material (Cuffey and Paterson, 2010). However, ice deformation is limited, and fast flowing ice is attributed to basal sliding and deformation of the material underlying the glacier. Basal sliding and glacier bed deformation are controlled by the form of the subglacial hydrological system (Iken and Bindschadler, 1986), which is itself controlled by the spatial and temporal distribution of water input (Arnold and Sharp, 2002; Schoof, 2010), ice speed, and glacier and bedrock topography. This is one example of how glaciers are complex systems, which exhibit nonlinear feedback mechanisms. In order to better understand the processes involved with glacier dynamics, this project will focus on the feedback mechanisms between the subglacial hydrological system and the ice sheet. The Siple Coast in Antarctica is a region which has displayed varied patterns of ice motion (Catania et al., 2012), and an active subglacial hydrological system (Siegfried et al., 2016), and it is therefore chosen as the study area for this project.

As glaciers can range on the order of hundreds to thousands of meters thick (Morlighem et al., 2020), there is difficulty involved with making direct observations of subglacial processes. The study of subglacial hydrology and basal sliding has therefore been largely theoretical and mathematical in nature. The advantage of a mathematical approach is that a mathematical model describes a simplified system, which can be tuned to examine the importance of various parameters or processes in question, and has the power of prediction. Though the importance of the feedback mechanisms between subglacial hydrology and ice dynamics has long been acknowledged (Iken and Bindschadler, 1986), coupled subglacial hydrology and ice flow models have been generally targeted towards describing specific events such as jökulhlaups (outburst floods from subglacial lakes) or spring events (Kessler and Anderson, 2004; Flowers et al., 2004, a proglacial flood early in the melt season marking the switch from inefficient to efficient subglacial drainage). However, with the recent development of complex subglacial hydrology models which use two dimensional unstructured meshes and describe a spectrum of inefficient to efficient drainage systems (Werder et al., 2013; Sommers et al., 2018), and friction laws which incorporate the full range of possible sliding regimes in ice flow models (Schoof, 2005; Gagliardini et al., 2007), we have just recently been able to harness the predictive power of mathematical modeling with regards to two-way coupled subglacial hydrology and ice flow models (Cook et al., 2022).

In this introductory chapter Section 1.1 gives a brief introduction of some of the equations describing ice motion. Section 1.2 gives an overview of inefficient distributed and efficient channelized subglacial hydrologic systems. Section 1.3 provides a basis of subglacial hydrology modeling and a summary of notable past studies which incorporate inefficient and efficient subglacial hydrologic systems within a single model. Section 1.4 describes various important sliding laws and friction laws. Section 1.5 describes notable characteristics of the Siple Coast, which is the study location for this project. Section 1.6 describes the layout of this thesis.

1.1 Ice flow modeling

Glaciers flow like viscous fluids (Cuffey and Paterson, 2010). The Cauchy momentum equation given by Eq. (1.1), and the continuity equation given by Eq. (1.2) govern the flow of a fluid.

$$\rho_i \frac{\partial \vec{u}}{\partial t} + \rho_i \left(\vec{u} \cdot \vec{\nabla} \right) \vec{u} = \vec{\nabla} \cdot \sigma + \rho_i \vec{g}. \tag{1.1}$$

$$\vec{\nabla} \cdot \vec{u} = 0. \tag{1.2}$$

Here, $\vec{u}$ is the velocity field, ρ_i is the density of ice, σ is the stress tensor, and $\vec{g}$ is the gravitational acceleration, taken to be the body force. However, even in the most extreme cases of ice motion, acceleration is not on the same scale as the other terms in the momentum equation (Reist, 2005). Therefore the momentum equations are written as Eq. (1.3), also known as the Stokes flow equations.

$$\vec{0} = \vec{\nabla} \cdot \sigma + \rho_i \vec{g}. \tag{1.3}$$

What remains is to have a constitutive relation relating σ to the strain rate $\dot{\varepsilon}$ given by index notation in Eq. (1.4),

$$\dot{\varepsilon} = \frac{1}{2}\left(\frac{\partial u_i}{\partial x_j} + \frac{\partial u_j}{\partial x_i}\right), \tag{1.4}$$

where u_i are the components of the velocity vector and x_i are the components of the position vector. The constitutive relation used in ice dynamics is given by Eq. (1.5) (Glen and Perutz, 1955).

$$\sigma' = 2\mu\dot{\varepsilon}, \quad \sigma' = \sigma + p_i I, \quad \mu = \frac{\tilde{B}}{2\dot{\varepsilon}_e^{\frac{n-1}{n}}}. \tag{1.5}$$

$$\dot{\varepsilon}_e = \sqrt{\frac{1}{2}\dot{\varepsilon}_{ij}\dot{\varepsilon}_{ij}}. \tag{1.6}$$

$$\tilde{B}(T) = \left(A_0 \exp\left(\frac{-Q}{R(T - \beta p_i))}\right)\right)^{\frac{-1}{n}}. \tag{1.7}$$

where σ' is the deviatoric stress, μ is the effective viscosity, p_i is the ice pressure, I is the identity matrix, $\dot{\varepsilon}_e$ is the effective strain rate (a tensor invariant) given in index notation by Eq. (1.6), n is an exponent typically taken to equal 3, which represents the nonlinearity of ice flow, $\tilde{B}$ is the ice rigidity, given as a function of temperature (T) by Eq. (1.7), A_0 is the flow factor, Q is the activation energy required for ice creep, R is the gas constant, and β is the rate of change of melting point with pressure.

Through plugging Eq. (1.5) into Eq. (1.3) and making use of Eq. (1.2) there is a set of four equations in four unknowns, namely the three components of ice velocity (u, v, w) and the pressure p_i. These equations are known as the full Stokes equations and are given by Eq. (1.8).

$$\begin{aligned}
\frac{\partial}{\partial x}\left(2\mu\frac{\partial u}{\partial x}\right)+\frac{\partial}{\partial y}\left(\mu\frac{\partial v}{\partial x}+\mu\frac{\partial u}{\partial y}\right)+\frac{\partial}{\partial z}\left(\mu\frac{\partial w}{\partial x}+\mu\frac{\partial u}{\partial z}\right)-\frac{\partial p_i}{\partial x}&=0,\\
\frac{\partial}{\partial x}\left(\mu\frac{\partial u}{\partial y}+\mu\frac{\partial v}{\partial x}\right)+\frac{\partial}{\partial y}\left(2\mu\frac{\partial v}{\partial y}\right)+\frac{\partial}{\partial z}\left(\mu\frac{\partial w}{\partial y}+\mu\frac{\partial v}{\partial z}\right)-\frac{\partial p_i}{\partial y}&=0,\\
\frac{\partial}{\partial x}\left(\mu\frac{\partial u}{\partial z}+\mu\frac{\partial w}{\partial x}\right)+\frac{\partial}{\partial y}\left(\mu\frac{\partial v}{\partial z}+\mu\frac{\partial w}{\partial y}\right)+\frac{\partial}{\partial z}\left(2\mu\frac{\partial w}{\partial z}\right)-\frac{\partial p_i}{\partial z}-\rho_i g&=0,\\
\frac{\partial u}{\partial x}+\frac{\partial v}{\partial y}+\frac{\partial w}{\partial z}&=0.
\end{aligned} \tag{1.8}$$

From the full Stokes equations various approximations can be made. Notably the Shallow Shelf Approximation (SSA) is a first order approximation to the depth averaged full Stokes equations, assuming that vertical shear is negligible ($\dot{\varepsilon}_{xz}, \dot{\varepsilon}_{yz} << \dot{\varepsilon}_{xx}, \dot{\varepsilon}_{yy}, \dot{\varepsilon}_{zz}, \dot{\varepsilon}_{xy}$), and that the ice pressure is determined by the depth of the ice so that $p_i = \rho_i g(S - z)$, where S is the ice surface elevation. As the depth averaging takes the system from three dimensional to two dimensional the basal shear stress (τ_b) applied as a boundary condition in the full Stokes equations has to be added explicitly in the SSA. The SSA is given by Eq. (1.9),

$$\begin{aligned}
\frac{\partial}{\partial x}\left(4H\bar{\mu}\frac{\partial u}{\partial x}+2H\bar{\mu}\frac{\partial v}{\partial y}\right)+\frac{\partial}{\partial y}\left(H\bar{\mu}\frac{\partial u}{\partial y}+H\bar{\mu}\frac{\partial v}{\partial x}\right)+\tau_{b,x}&=\rho_i g H\frac{\partial S}{\partial x},\\
\frac{\partial}{\partial y}\left(4H\bar{\mu}\frac{\partial v}{\partial y}+2H\bar{\mu}\frac{\partial u}{\partial x}\right)+\frac{\partial}{\partial x}\left(H\bar{\mu}\frac{\partial u}{\partial y}+H\bar{\mu}\frac{\partial v}{\partial x}\right)+\tau_{b,y}&=\rho_i g H\frac{\partial S}{\partial y},
\end{aligned} \tag{1.9}$$

where H is the ice thickness, $\bar{\mu}$ is the depth averaged viscosity, and $\tau_{b,x}$ and $\tau_{b,y}$ are the x and y components of the basal shear stress. A full derivation of the SSA is given by MacAyeal (1989).

The SSA says that the driving stress (the force driving ice motion due to gradients in the ice surface) is balanced by the basal shear stress and ice motion. The basal shear stress often supplies the primary form of resistive stress (Cuffey and Paterson, 2010) and the only form of resistive stress in the SSA and is therefore an important quantity discussed in Section 1.4.

The full Stokes equations or one of their approximations such as the SSA are solved in ice flow modeling to determine the ice velocity. Ice geometry is often updated using a mass transport equation derived from mass balance given by Eq. (1.10),

$$\frac{\partial H}{\partial t} + \vec{\nabla} \cdot (H \vec{u}) = M, \tag{1.10}$$

where $\vec{u}$ is the depth averaged velocity, and M is a source term, which accounts for accumulation and ablation on the ice surface and base.

1.2 The subglacial hydrologic system

Glaciers have complicated hydrologic systems with supraglacial, englacial and subglacial components depicted in Fig. 1.1. Subglacial hydrology has long been an area of interest in the glaciological community, with subglacial water pressure playing an important role in the theory of basal sliding (Budd et al., 1979), which acts as a basal boundary condition in the full Stokes equations and τ_b in the SSA. In the 1970s theories describing channels incised within the glacier (Röthlisberger, 1972) – Röthlisberger channels (R-channels) – and channels incised within the underlying sediment or bedrock (Nye, 1973) – Nye channels – were developed alongside theories of thin sheets of water between the glacier and the glacier bed (Weertman, 1972). The theory of water sheets evolved into a theory of water flowing through cavities in the ice, which were linked together through narrow orifices created from basal sliding over bedrock protrusions (Walder, 1986; Kamb, 1987). By the mid 1980s it was agreed that both efficient drainage systems such as R-channels and Nye channels and inefficient drainage systems such as these linked cavity systems or water sheets are both components of the subglacial hydrologic system (Walder, 1986; Kamb, 1987). The composition of the system was expected to be spatially and temporally variable, and the theory of mechanisms behind switches between inefficient and efficient drainage was developed.

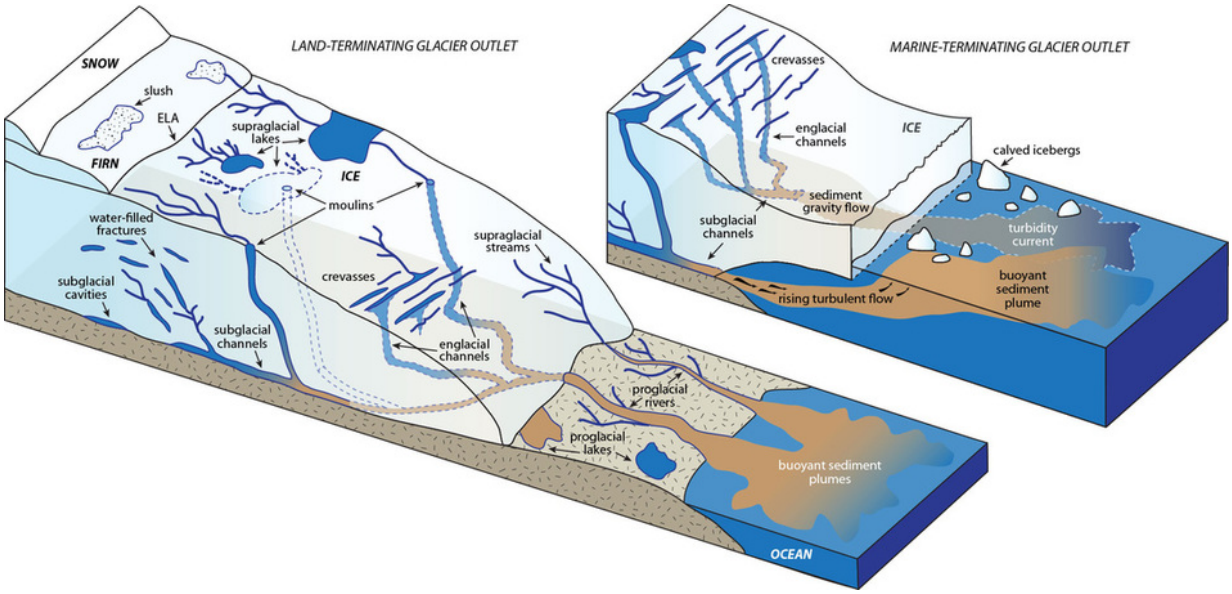

Figure 1.1: Example hydrologic system of Greenland glaciers from Chu (2014).

1.2.1 Channels

Motivated by observations of large subglacial channels draining temperate valley glaciers, Röthlisberger (1972) mathematically described water filled englacial channels of circular cross section and subglacial channels of semi-circular cross section. Röthlisberger assumed that channels experienced steady state water flow, with a balance of opening due to frictional melting of ice caused by instantaneous heat transfer (advection of heat was not considered) and closing due to ice creep (Fig. 1.2). Röthlisberger did not take into account the flow of ice at the bed of the glacier and spatially variable ice overburden pressure. This theory alone would describe an arborescent channel system, but Röthlisberger argued that spatially variable ice pressure would prioritize a single main channel at the bed of the glacier with an additional two channels at the lateral boundaries where water is likely to be input into the subglacial system. Around the time Röthlisberger described R-channels, Nye (1973) described broad narrow channels, which carved into the bedrock beneath the ice. Röthlisberger argued that these channels were less likely to from due to differences of the material being eroded (rock compared to ice) and the possibility for changes in ice pressure to result in the conditions for channel formation to change both spatially and temporally. Weertman (1972) noted that geomorphological evidence of the existence of Nye channels was difficult to come across due to erosion of glacier bed parallel to diminishing channels

under a shrinking glacier. Regardless, he deduced that Nye channels parallel to ice flow would form with overlying R-channels meaning that much of the mathematical treatment of Nye channels could be borrowed from that of R-channels, despite arguing that pressure gradients should drive water away from R-channels and that if Nye channels exist they would play a significant role in the subglacial drainage system. Much of the mathematical theory involving subglacial channelized drainage developed thereafter considers R-channels as opposed to Nye channels.

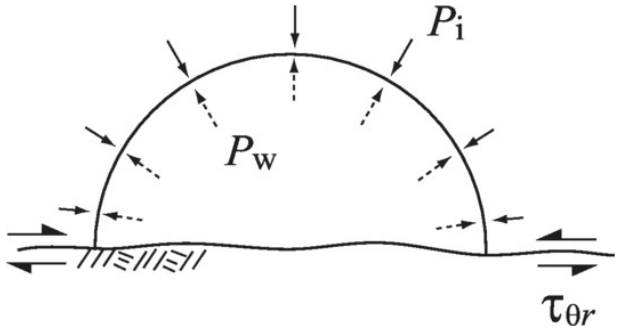

Figure 1.2: R-channel from (Hooke, 2019), which opens due to frictional melting of ice and closes due to ice creep.

In trying to determine characteristics of channelized glacial drainage systems, Shreve (1972) considered two parallel channels carrying some combined constant discharge, which were allowed to exchange water mass with each other. His analysis did not discriminate between supraglacial, englacial, and subglacial hydrology, opting to instead vary the ambient ice pressure surrounding the channels. He found that the larger of the two channels would increase in size at the expense of the smaller channel except when the smallest channels were considered. This was because the melt rate due to viscous dissipation of potential energy per unit channel area is greater in the larger channel, therefore lowering the water pressure of the larger channel compared to the smaller channel. This would favour an arborescent channel system with smaller channels draining into larger ones. Shreve noted that subglacial channels would follow the lines of the greatest decrease in hydraulic potential given by Eq. (1.11),

$$\phi = \phi_0 + p_w + \rho_w g z, \tag{1.11}$$

where ϕ is the hydraulic potential, ϕ_0 is an arbitrary constant, p_w is the water pressure, ρ_w is the density of water, g is the norm of the gravitational acceleration and z is the

elevation. On a level bed slope this would be the direction of surface slope and ice flow; the larger the surface slope of the ice, the larger the role it would play in the direction of subglacial channels.

1.2.2 Hydrology sheet

Weertman (1972) considered a thin sheet of water underneath the glacier allowed to flow freely, and having water pressure equal to ice overburden pressure given by $p_i = \rho_i g H$ where H is the ice thickness. He determined that the surface slope of the glacier plays a much more significant role in the subglacial water pressure gradient than the bed slope with a ratio of the two terms of $\rho_i/(\rho_w - \rho_i) \approx 11$. Weertman also considered when there were irregularities in the bed of the glacier and determined that the high water pressure on the stoss sides of bedrock obstacles would mean virtually no water would be present in these areas, leaving a "punctured" water sheet. Because of the increased pressure on the stoss side of obstacles, to have the average water pressure equal to ice overburden as in his uniform sheet of water, Weertman deduced that water in the punctured water sheet must be less than overburden pressure. Weertman made an extensive analysis of both R-channels and Nye channels within this paper, but ultimately argued that flow from a water sheet into a channelized drainage system was unlikely. When basal shear stresses were taken into account channels would only be able to capture water from some distance beyond the channel given by $R_{\text{crit}} = a(\Delta P/\tau_b)^{n/2}$ where a is the radius of the channel, ΔP is the difference between the water pressure at the channel wall and ice overburden pressure, and τ_b is the basal shear stress. When a is small, ΔP is also small and the channel cannot grow through taking in water from the hydrology sheet. Aside from the a centerline R-channel or Nye channel, Weertman argued that the subglacial hydrological system was dominated by a punctured water sheet.

However, there were arguments against the existence of a subglacial water sheet as well. Nye (1976) argued that due to the importance of ice surface gradients in determining subglacial hydrologic pathways, water in any form of sheet would tend towards areas dictated by ice surface slopes where they would form channels, meaning that sheet drainage would be unstable. He also argued that areas where the hydrology sheet was thicker would tend to have larger discharge and would open faster due to melting, also creating channels. These concerns from Nye were addressed by Walder (1982) who considered sheet flow with variable thickness and temperature. He found that on a planar bed nearly all sheet flow was unstable, but with the roughness of a real bed sheet flow may be stable below some critical sheet thickness, which was sensitive to the bed roughness model assumed.

1.2.3 Linked cavities

Evidence of water-filled cavities underneath the ice (Walder and Hallet, 1979) would eventually lead to the abandonment of the theory of a continuous water sheet, replaced by a system of water filled cavities linked together through narrow channels or orifices (Walder, 1986; Kamb, 1987, Fig. 1.3). Walder (1986) considered cavities formed by ice sliding over a step of bedrock, with the cavity length being determined by the height of the bedrock protrusion, the creep of the ice, and the melting rate of the cavity roof. It was found that, unlike R-channels, basal sliding was the dominant term in the cavity opening rate, as opposed to melt from dissipation of frictional heat. However, with a high enough basal water pressure the opening rate could balance the closing rate of the cavity meaning that the cavity wouldn't close, it would become unstable. This finding was similar to that of Iken (1981) who did not model cavity formation, but found that there was a maximum ratio of the basal shear stress to the effective pressure that the glacier bed could support.

On top of developing a mathematical formulation of water filled cavities, Walder (1986) hypothesized about the switch between cavitized and channelized forms of subglacial drainage. He suggested that an R-channel flowing through a system of cavities may be tapped by those cavities, slowly reducing water discharge and channel size. He noted that in the event of increased basal water input to a cavity/channel system the channels would stabilize at lower water pressure than the cavities, pulling water from them and obtaining even lower water pressures until the cavity system would shut down. In the case of water pressure above the threshold of a stable cavity system, Walder suggested that an arborescent system of R-channels would form, possibly only temporarily.

Through examining data from the 1982-1983 surge of Variegated Glacier in Alaska, Kamb (1987) developed a model of cavities linked together through narrow orifices. He argued that the linking orifices controlled the evolution of the hydraulic system. The geometry of orifices was determined from ice sliding over a step, and over a wavy bed. Unlike channelized drainage, there was a direct (as opposed to inverse) relationship between discharge and water pressure. Because of this direct relationship, a linked cavity system can persist without the water localizing in a central path as with channelized drainage. Like Walder, Kamb found that a linked cavity system required larger water pressure to obtain an equivalent discharge as a channelized system, meaning that once channels begin to form in a hydraulic system with high water pressure, they will be favoured. Kamb noted the instability of the linked cavity system, which arises from the balance of heat dissipation and ice creep, but unlike Walder (1986) framed it as an issue of how much heat dissipation plays a role in orifice opening, not what values of effective pressure can provide a stable linked cavity system.

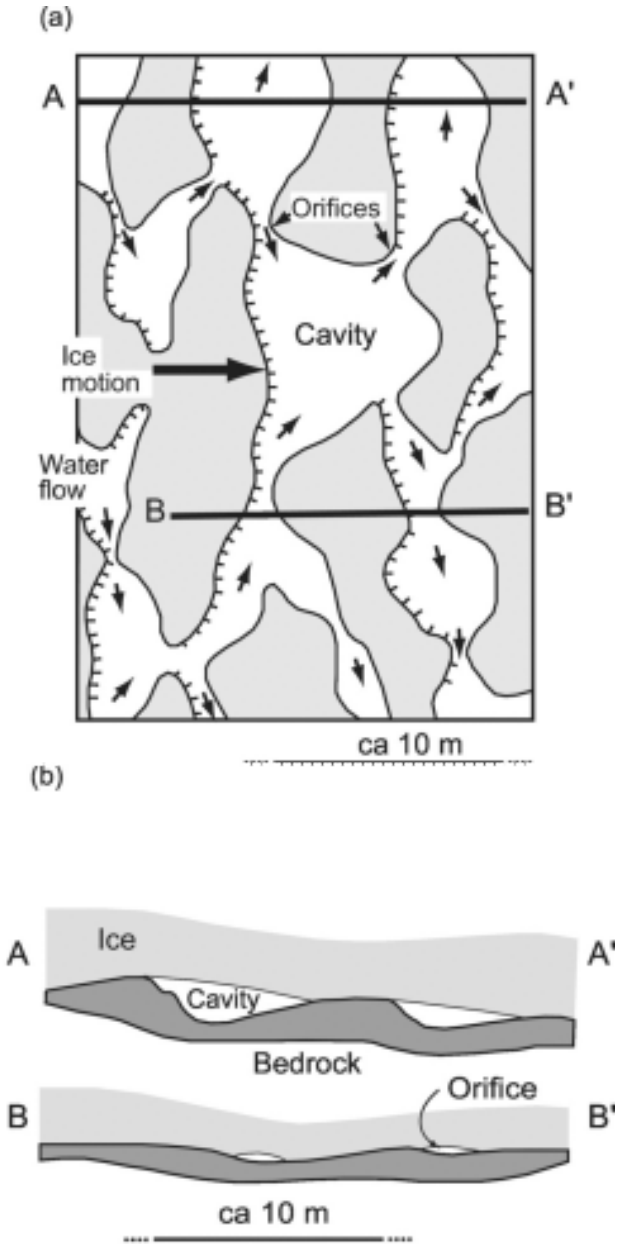

Figure 1.3: Linked cavity system from Hooke (2019), adapted from Kamb (1987). (a) is a top view of the wider cavities connected through the narrow orifices; (b) is the plan view of the cross sections of cavities and orifices.

1.3 Subglacial hydrology modeling

Due to the complicated nature of the subglacial hydrological system having both inefficient and efficient drainage components as discussed in Sections 1.2, there have been a variety of subglacial hydrological models produced by the glaciological community. Though these models differ in their treatment of the multi-component nature of the subglacial hydrological system, they have many similarities in their governing equations. Subglacial hydrology models typically have a conservation of mass equation, and a parameterization relating the fluid velocity to the hydraulic potential (Flowers, 2015). Due to the similarities of the governing equations of most subglacial hydrology models, the novelty of a subglacial hydrology model comes from how it deals with inefficient and efficient drainage and the switch between the two. At the turn of the century came a series of modeling efforts to describe subglacial drainage with both inefficient and efficient drainage components (Flowers and Clarke, 2002; Arnold and Sharp, 2002; Kessler and Anderson, 2004; Flowers et al., 2004). Various approaches were taken, but sophisticated models which allowed for continuous switch between efficient and inefficient drainage over the entirety of a two dimensional model domain were not seen until the 2010s (Schoof, 2010; Werder et al., 2013; Sommers et al., 2018).

1.3.1 Governing equations

Subglacial hydrology models consider the flow of a sheet of water, such as an areally averaged porous water sheet or linked cavity system, or flow through a semi-circular conduit, such as an R-channel. Though the exact system will change the form of the governing equations of the model, similar physical principles are usually considered to arrive at these governing equations.

Conservation of mass requires that the change in sheet thickness h or channel cross sectional area S_c is balanced by water flux to or from the point in question and a source term. For a hydrology sheet, conservation of mass reads as Eq. (1.12) and for a conduit it reads as Eq. (1.13).

$$\frac{\partial h}{\partial t} + \vec{\nabla} \cdot \vec{q} = m_s. \tag{1.12}$$

$$\frac{\partial S_c}{\partial t} + \frac{\partial q_c}{\partial s_c} = m_c. \tag{1.13}$$

Here, $\overrightarrow{q}$ is the sheet discharge, q_c is the conduit discharge, s_c is the conduit coordinate, and m_s and m_c are the water input/source terms for the sheet and conduit respectively. In determining m_s and m_c, melt due to frictional heat, geothermal heat flux, viscous dissipation of heat, and water transfer from the englacial system, the groundwater system, or a connected sheet or conduit are typically considered. The discharge is usually related to the hydraulic potential through an empirical Darcy-Weisbach law, which for a sheet is given by Eq. (1.14) and for a channel is given by Eq. (1.15),

$$\overrightarrow{q} = -k_s h^{\alpha_s} \left| \overrightarrow{\nabla} \phi \right|^{\beta_s - 2} \overrightarrow{\nabla} \phi, \tag{1.14}$$

$$Q = -k_c S_c^{\alpha_c} \left| \frac{\partial \phi}{\partial s_c} \right|^{\beta_c - 2} \frac{\partial \phi}{\partial s_c}, \tag{1.15}$$

where k_s and k_c are the hydraulic conductivities of the sheet and channel respectively and α_i, β_i are exponents controlling the type of flow typically taken to be $\alpha_i = \beta_i = 1$ for laminar and $\alpha_i = 5/4$, $\beta_i = 1/2$ for turbulent. The system can be closed with a parameterization for ϕ, which relates the hydraulic potential/effective pressure/subglacial water pressure to the sheet thickness or conduit cross sectional area. This would result in a first order differential equation for the sheet thickness or the channel cross sectional area in time. Alternatively an equation describing the time evolution of h or S_c could be used as in Eq. (1.16) for a sheet and Eq. (1.17) for a conduit,

$$\frac{\partial h}{\partial t} = \omega_s - \nu_s, \tag{1.16}$$

$$\frac{\partial S_c}{\partial t} = \omega_c - \nu_c, \tag{1.17}$$

where ω_s and ω_c are opening rates for sheets and conduits respectively and ν_s and ν_c are closing rates for sheets and conduits respectively. Sheet opening is typically due to sliding over bedrock obstacles and conduit opening is typically due to melt of ice, however a combination of the two can be used. Closing is usually due to viscous creep of ice. Choosing to parameterize the opening and closing rates of the sheet or conduit would result in a second order partial differential equation for the hydraulic potential and a first order differential equation in time for the sheet thickness or conduit cross sectional area.

1.3.2 Subglacial hydrology models of the 2000s

Over the years there have been many attempts to unify the ideas of inefficient subglacial drainage systems such as linked cavity systems with efficient subglacial drainage systems such as channelized drainage, under a single model. There have been many approaches to the problem, varying in their degree of sophistication. Flowers and Clarke (2002) produced a model of glacier hydrology with supraglacial, englacial, subglacial, and subsurface components. Each component had its own two dimensional layer, and the layers were coupled together through water exchange. The subglacial component of the model featured a porous water sheet, which obtained water through geothermal and frictional melting of ice, and exchange with the englacial and subsurface components of the model. The discharge was determined from Darcian flow (laminar) and the water pressure was parameterized as a function of the thickness of the water sheet, going to ice overburden pressure as $(h/h_c)^{7/2}$ where h is the thickness of the water sheet and h_c is some critical hydrology sheet thickness. This parameterization was derived empirically for Trapridge Glacier. The conductivity was allowed to vary as a function of the thickness of the hydrology sheet, with large variation of orders of magnitude around h_c denoting a switch from inefficient to efficient subglacial drainage. These concepts of parameterizing the effective pressure and variable hydraulic conductivity would be fundamental in subglacial hydrology models moving forward.

With the aim to model the impact of subglacial hydrology on the ice dynamics of the late Weichselian Scandinavian Ice Sheet, Arnold and Sharp (2002) developed an ice flow model and a subglacial hydrology model, coupled through an effective pressure dependent sliding law. Each grid cell could be classified as having either an inefficient drainage system or an efficient drainage system, which was dependent on whether a channelized drainage system was stable. The stability criterion was taken from Fowler (1987), who considered water exchange between a channelized and linked cavity system and found the conditions necessary for water to flow into and sustain channelized drainage. The stability condition depends on the effective pressure and the basal sliding speed. Once the cell is determined to be inefficient or efficient, the effective pressure is calculated from a parameterization also from Fowler (1987). Using their coupled model, Arnold and Sharp were able to produce ice speed and ice sheet thickness which match qualitatively with geological evidence. Isolated regions of fast flowing ice were only observed when non uniform melt water input was used, signifying the importance of spatially variable water input on subglacial hydrology and ice dynamics.

Kessler and Anderson (2004) looked to model spring speed up events and outburst floods of ice-marginal lakes using a coupled ice flow and subglacial hydrology model. They assumed a linked cavity system in the form of conduits opening due to basal sliding and

melting and closing due to ice creep. The linked cavity system is connected to an englacial reservoir and routes water to a centerline efficient channel through a tortuous path where water is assumed to travel three times the Euclidean distance from the its input to the centerline channel. The subglacial system is linked to an ice flow model via a sliding law which assumes no sliding for water pressure less than ice overburden and sliding as a function of the effective pressure for greater subglaical water pressures (Anderson et al., 2004). Kessler and Anderson were able to reproduce the behaviour of a spring event, with basal sliding due to increased subglacial water pressure initiating at the glacier terminus and propogating upglacier throughout the melt season. Enhanced ice speed ended abruptly when the subglacial hydrologic system had evolved to efficiently handle melt water supply.

In trying to model the processes involved in jökulhlaups, Flowers et al. (2004) made a one dimensional flowline model of the subglacial hydrologic system, which included a component of macro-porous sheet flow and a component of channelized flow, which were allowed to exchange water with each other. The exchange rate was proportional to the difference in water pressure between the sheet and channel systems. Water pressure in the sheet system was parameterized as a function of the sheet thickness as in Flowers and Clarke (2002), the water pressure in the channel was determined by solving the water mass balance equation in the channel at each time step. With an adjustment of model parameters, this model was able to reproduce the arrival time of floodwater at the glacier terminus, which proceeded the arrival time of channelized discharge, and it reproduced the time of peak floodwater discharge at the glacier terminus.

Schoof (2010) aimed to test the impact of mean water supply and water supply variability to the subglacial hydrologic system on ice motion in Greenland. He unified the ideas of inefficient and efficient drainage systems by considering the equation for the evolution of a conduit, which opens due to melt and sliding and closes due to ice creep (Fig. 1.4a,b). The system could be classified as inefficient if the relationship between water discharge and water pressure was direct, and classified as efficient if the relationship was inverse (Fig. 1.4d). Schoof found the critical discharge at which this switch occurred (Fig. 1.4d) and noted that if the conduit was classified as inefficient it was kept open mainly by sliding and if the conduit was efficient it was kept open mainly by melt. Using this model, Schoof showed how temporal melt water variability is responsible for fast ice flow events even when the subglacial hydrological system is efficient. He noted that this was because the time scale for the system to accommodate the extra water input was longer than the time scale of the input itself.

At this point, subglacial hydrology models which include both inefficient and efficient drainage had success emulating the processes they were built for. However, these models were often one dimensional with the exception of Schoof (2010) and Flowers and Clarke

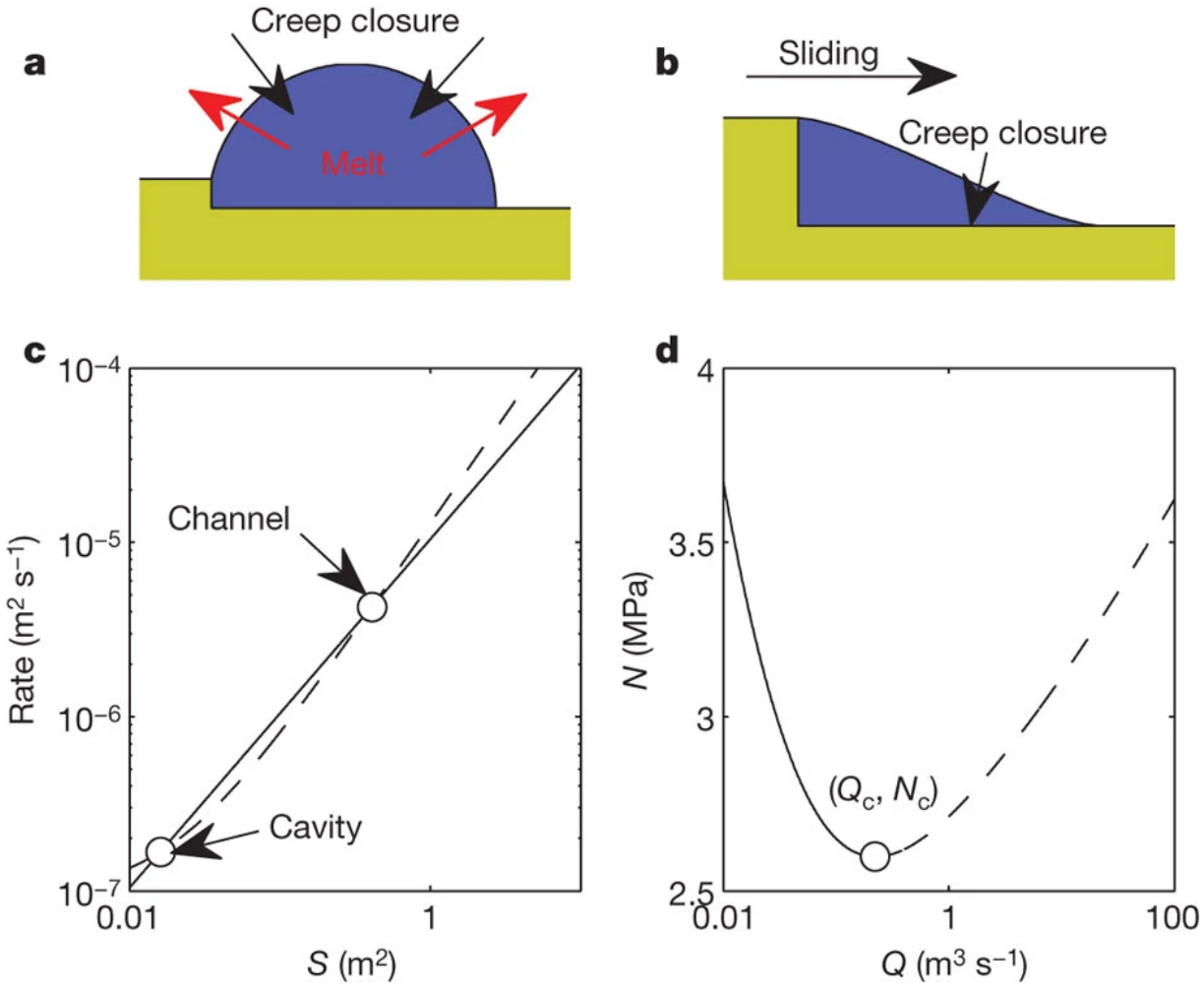

Figure 1.4: Conduit properties for Schoof's model (Schoof, 2010), which allows conduits to be efficient or inefficient. (a) underlying physics involved with channels; (b) underlying physics involved with cavities; (c) conduit opening (dashed line) and closing (solid line) rates as a function of conduit cross sectional area with depicted stable cavity and channel solutions; (d) effective pressure (N) as a function of discharge (Q) for a steady state conduit, above a critical point a cavity (solid line) becomes a channel (dashed line) and the relationship between water pressure and discharge goes from direct to inverse.

(2002), and built to model specific processes i.e. jökulhlaups (Kessler and Anderson, 2004; Flowers et al., 2004), and spring events (Flowers et al., 2004). In 2013, Werder et al. (2013) developed a two dimensional subglacial hydrology model with inefficient and effi-

cient drainage components, which could be solved on an unstructured mesh, which they called the Glacier Drainage System (GlaDS) model. GlaDS uses finite element methods, where each element was assumed to be in an inefficient linked cavity system, and each element edge is assumed to be an R-channel. In areas where inefficient drainage dominated, channel cross sectional area along element edges would be infinitesimal. In areas where the channelized drainage dominated the effective pressure of the surrounding elements would increase. The hydrology sheet on each element was allowed to grow due to basal sliding and close due to creep of ice. Channels open due to melt and close due to creep of ice. The model solves a mass balance equation for the hydraulic potential at each time step meaning that there is no prescription for the subglacial water pressure. Though GlaDS was originally applied to synthetic geometries representative of small alpine and Greenland glaciers, it has since seen widespread use in Greenland (Poinar et al., 2019; Ehrenfeucht et al., 2023; Verjans and Robel, 2024) and Antarctica (Dow et al., 2018, 2020, 2022; Dow, 2022) and served as the basis for the Subglacial Hydrology Model Intercomparison Project (de Fleurian et al., 2018, SHMIP).

Following from many of the GlaDS model equations, Sommers et al. (2018) developed the Subglacial Hydrology and Kinetic Transient Interactions (SHAKTI) model, which also uses finite element methods allowing for an unstructured computational mesh. SHAKTI did not include channels on element edges, opting to instead create a single set of equations describing a hydrology sheet with hydraulic transmissivity that is allowed to change as a function of the hydrology sheet thickness and the Reynold's number, which describes whether flow is laminar or turbulent. The varying transmissivity allows for a spectrum between inefficient and efficient drainage. Opening of the hydrology sheet is due to both sliding and melt, the dominant term being a consequence of if the system is efficient or inefficient. The model is able to create strings of high transmissivity elements equivalent to channelized drainage.

1.4 Friction laws and sliding laws

Alongside the development of subglacial hydrology models, came the theory of basal sliding, though the theory of basal sliding did not originally incorporate subglacial hydrological processes, instead assuming that sliding occurred due to regelation of basal ice and enhanced creep around bed obstacles (Weertman, 1957). The Weertman sliding law (Weertman, 1957) proposed that basal shear stress is a function of the basal sliding velocity and the bed geometry, excluding subglacial hydrological quantities from the expression altogether. However, even at the conception of the Weertman sliding law, it was understood that rege-

lation and enhanced creep were not capable of explaining observed sliding speeds, which were sometimes an order of magnitude greater than those proposed by the sliding law. In the 1970s the link between subglacial hydrology and basal sliding was made, and sliding laws with dependence of the basal shear stress on effective pressure were developed (Budd et al., 1979). The first sliding laws with the inclusion of effective pressure were simplistic power laws (Budd et al., 1979), but the theory of basal sliding developed in parallel with the theory of subglacial hydrology and in particular linked cavity systems. Iken (1981) found that there is a maximum ratio of basal shear stress to effective pressure, after which, longitudinal and lateral stresses must support the driving stress. This would mean that the search for a sliding law which can determine the sliding velocity given the basal shear stress was in vain, as the same shear stress could support different sliding speeds. A friction law, which relates basal shear stress to sliding speed and does not necessarily have a unique sliding speed for each value of the basal shear stress was then sought after. In the 2000s, friction laws were developed, which encompass the sliding described by Weertman (1957) and the sliding described by Iken (1981) and allow for a continuum between these two end cases (Schoof, 2005; Gagliardini et al., 2007).

1.4.1 Sliding laws

Basal sliding has been recognized as an important process in ice flow for a long time. Mathematical formulations of basal sliding date back to the 1950s, where Weertman (1957) considered sliding around cubic bedrock protrusions due to regelation and enhanced creep. He found that the sliding speed was proportional to the second power of the basal shear stress with the constant of proportionality being difficult to estimate as it had a strong dependence on the size of the bedrock protrusions relative to their spacing. Weertman determined that regelation and enhanced creep alone would not produce appreciable sliding rates, but if considered together then basal sliding of $1\,\mathrm{m\,a^{-1}}$ was achievable, but still outside the range of 4-79 $\mathrm{m\,a^{-1}}$ predicted by Nye (1952) for a number of glaciers. A sliding law relating the basal sliding speed as proportional to a power of the basal shear stress would come to be known as the Weertman sliding law, which is given by Eq. (1.18),

$$\tau_b = \alpha_w^2 \, |\overrightarrow{u_b}|^{s-1} \, \overrightarrow{u_b}, \tag{1.18}$$

where α_w is the Weertman sliding coefficient, s is the sliding law exponent, and $\overrightarrow{u_b}$ is the basal sliding velocity.

Budd et al. (1979) approached the problem from an experimental perspective, devising laboratory tests to try to find a relationship between the normal stress, the shear stress, and the sliding velocity. He devised experiments of limiting static shear, constant applied shear, and constant applied velocity over various rough surfaces. Budd's experiments did not all agree on a relationship between the normal stress, shear stress, and sliding velocity, with proportionality to various powers of the combination of variables arising for the different experiments. Regardless, the power law relation put forth by Budd is often used in modeling studies today (Åkesson et al., 2021; Khan et al., 2022), as it has explicit dependence on the normal stress or effective pressure, which is dependent on the subglacial hydrological system. The Budd sliding law is given by Eq. (1.19),

$$\tau_b = \alpha_b^2 N^r \, |\overrightarrow{u_b}|^{s-1} \, \overrightarrow{u_b}, \tag{1.19}$$

where α_b is the Budd sliding coefficient, N is the effective pressure, which is equal to the difference between the ice overburden pressure and the subglacial water pressure, and r and s are sliding law exponents.

1.4.2 Friction laws

Iken (1981) considered sliding over a tilted staircase of bedrock and determined that there was a maximum ratio of the basal shear stress to the effective pressure that was equal to the tangent of the largest angle of the stoss faces of bedrock protrusions. This bound on the ratio between the basal shear stress and the effective pressure would come to be known as Iken's bound. This would mean that with a low enough effective pressure, a given basal shear stress could support many different sliding velocities. A sliding law, which gives a unique value of sliding speed for each value of the basal shear stress is therefore insufficient to describe the full range of physical processes occuring at the glacier bed. A friction law, which acts as a relationship between the sliding velocity, basal shear stress, and effective pressure, which does not necessarily have a unique sliding velocity for a given basal shear stress is needed to capture the sliding which Iken proposed.

Though the derivation of Iken's bound was first proposed considering the specific bedrock geometry of a tilted staircase, it was extended to a general bedrock geometry by Schoof (2005). Schoof found, like Iken, that the ratio of the basal shear stress to the effective pressure was bounded by the supremum of the derivative of the bedrock geometry, or in other words: the maximum angle on the stoss side of bedrock protrusions. Schoof

went on to consider sliding over a cavitated bed assuming that ice obeyed a linear rheology ($n = 1$). Schoof found that for low ice speed the basal shear stress was proportional to the basal sliding speed. However the basal shear stress reached a maximum for some finite sliding speed where it would then level off and actually decrease. Schoof summarized the qualitative aspects of his findings in a friction law, which for low sliding speed and high effective pressure behaved like the Weertman sliding law but for high sliding speed and low effective pressure displayed the bounded nature of the basal shear stress. Schoof's law was not derived from a physical system, he rather searched for an analytical relation between sliding speed, effective pressure, and basal shear stress, which encompassed the nature of sliding over cavitation. These types of friction laws, which switch continuously over Weertman sliding regimes and the sliding proposed by Iken are known as regularized Coulomb friction laws. Though Schoof (2005) considered sliding over cavitation with a linear ice rheology, he proposed a nonlinear version of his friction law as well (Eq. 1.20),

$$\frac{\tau_b}{N} = C \left(\frac{\Lambda}{\Lambda + \Lambda_0} \right)^{1/n}, \quad \Lambda = \frac{u_b}{N^n}, \tag{1.20}$$

where C is a friction coefficient, n is the exponent in Glen's flow law, and Λ_0 is the value of u_b/N^n should tend to as τ_b/N reaches it's maximum.

Gagliardini et al. (2007) simulated sliding due to cavitation over sinusoidal and ellipsoidal bedrock protrusions using a nonlinear ice rheology, and considered (unlike Schoof) where bedrock protrusions had stoss faces with unbounded slopes. From their simulations, they were able to formulate a set of four conditions that a friction law should follow.

- $\tau_b/(CN^n) = f(\chi)$, where $\chi = u_b/(C^n N^n A_s)$, C is a parameter which is less than the maximum stoss face slope of bedrock protrusions and A_s is a sliding parameter when there is no cavitation.
- $\left|\frac{\partial f}{\partial \chi}\right|_{\chi=0} = 1$ which means that when there is no cavitation the friction law behaves like the Weertman sliding law.
- $\frac{\partial f}{\partial \chi} = 0 \implies f(\chi) = 1 \forall n$ which enforces Iken's bound so that there is a maximum ratio of the basal shear stress to the effective pressure regardless of the ice rheology assumed.
- $\tau_b/N \leq C_{\max} \forall \chi > \chi_m$ where $C_{\max}$ is the tangent of the maximum stoss face slope of bedrock protrusions, and χ_m is the value of χ for which f obtains a maximum. This enforces Iken's bound for larger values of χ.

They proposed a friction law based on these four conditions, which unlike Schoof's friction law accounted for the decrease in the ratio of the basal shear stress to the effective pressure once the maximum was reached. They noted that Schoof's generalization of his friction law to nonlinear rheologies agreed with the conditions they proposed. Their proposed friction law is given by Eq. (1.21),

$$\frac{\tau_b}{N} = C\left(\frac{\chi}{1+\alpha\chi^q}\right)^{1/n}, \quad \alpha = \frac{(q-1)^{(q-1)}}{q^q}, \tag{1.21}$$

where q is a parameter of the sliding law. When $q = 1$ this is equivalent to the friction law proposed by Schoof except that τ_b/N is now a function of $u_b/(C^n N^n)$ not u_b/N^n.

1.5 Siple Coast

The important interplay between subglacial hydrology and ice dynamics was originally observed on alpine glaciers, and glaciers on the Greenland Ice Sheet (GIS) (Joughin et al., 2008; van de Wal et al., 2008; Parizek and Alley, 2004). These locations have a melt season in the summer months, which supplies spatial and temporally variable inputs of meltwater to the subglacial hydrologic system. This variable water input allows for a reorganization of the subglacial hydrologic system and the consequent change in ice flow patterns.

While ice-hydrology feedbacks are readily observed in these regions, they still have a major role to play in Antarctica as well (Dow, 2022), which produces little to no surface melt in the Austral summer. In Antarctica the subglacial hydrologic system obtains water through geothermal heat flux and frictional heat, which melt basal ice. Though subglacial hydrology in Antarctica is often modeled to steady state (Dow et al., 2018, 2020, 2022; McArthur et al., 2023), over longer timescales than the annual changes on the GIS and alpine glaciers, Antarctic subglacial hydrological and ice flow patterns change significantly as in cases of ice and water piracy (McCormack et al., 2023). As Antarctica's contribution to sea level rise is almost entirely dependent on ice flow processes driving ice towards the ocean, the interactions between the subglacial hydrological system and the ice sheet are of utmost importance to study in Antarctica.

The Siple Coast, which is the study area for this project is located in West Antarctica, buttressed by the Ross Ice Shelf (RIS), the largest ice shelf in the world (Rignot et al., 2013). West Antarctica is currently losing mass, which is largely a result of the speed

up of the Pine Island and Thwaites glaciers in the Amundsen Sea Embayment (Rignot et al., 2022). However, the glaciers of the Siple Coast have been counteracting this process and have shown a net mass gain of $36 \pm 16\,\mathrm{Gt\,a^{-1}}$ (Pritchard et al., 2009). Though Siple Coast's mass balance and sea level contribution are no reason for concern at present, the Siple Coast attracts interest because of its ice dynamics and subglacial hydrology. The Siple Coast has at present, four active ice streams (Fig. 1.5), which tend to shut down and reactivate on century long timescales (Catania et al., 2012). The current trends of mass gain in the Siple Coast can be attributed to the shut down of the Kamb Ice Stream 170 years ago (Bougamont et al., 2015). Underneath these ice streams lie numerous active subglacial lakes, which fill and drain on the order of years, and are thought to have an impact on the dynamics of the overlying ice (Livingstone et al., 2022; Sergienko et al., 2007).

1.5.1 Ice stream reorganization

The ice streams of the Siple Coast have a long record of variability, with changes in the past millennium compiled and detailed by Catania et al. (2012). They found shut down and reactivation of the Whillans ice stream from around 1150 to 1557 and the MacAyeal ice stream from around 1207 to 1357. The Siple Ice Stream shut down around 1582 and another tributary of the Kamb Ice Stream shut down around 1750. Eventually the Kamb Ice Stream stagnated in 1837. They suggested that the Whillans Ice Stream is again in the process of stagnation; it is slowing and thickening and should continue for the next 60-70 years, which should result in the Kamb Ice Stream reactivation. Along with these changes in ice streams came the growth and decay of ice rises and grounding line retreat and advance. The ice stream, ice rise, and grounding line changes all have effects on each other meaning that the ice flow of the Siple Coast is in a constant state of change as a result of internal ice sheet instabilities.

Bougamont et al. (2015) modeled the Siple Coast 250 years into the future using a simple subglacial hydrology model, a subglacial processes model involving a till layer, and an ice sheet model. They found the continuation of the ice stream dynamics outlined by Catania et al. (2012). Whillans Ice Stream slowed down but did not completely stagnate, and the Bindschalder Ice Stream, the Kamb Ice Stream, and its tributary the Siple Ice Stream were reactivated. They noted that the subglacial hydrological system, although poorly constrained, had a large control on the modeled ice sheet dynamics, and an active subglacial hydrologic system led to larger ice discharge.

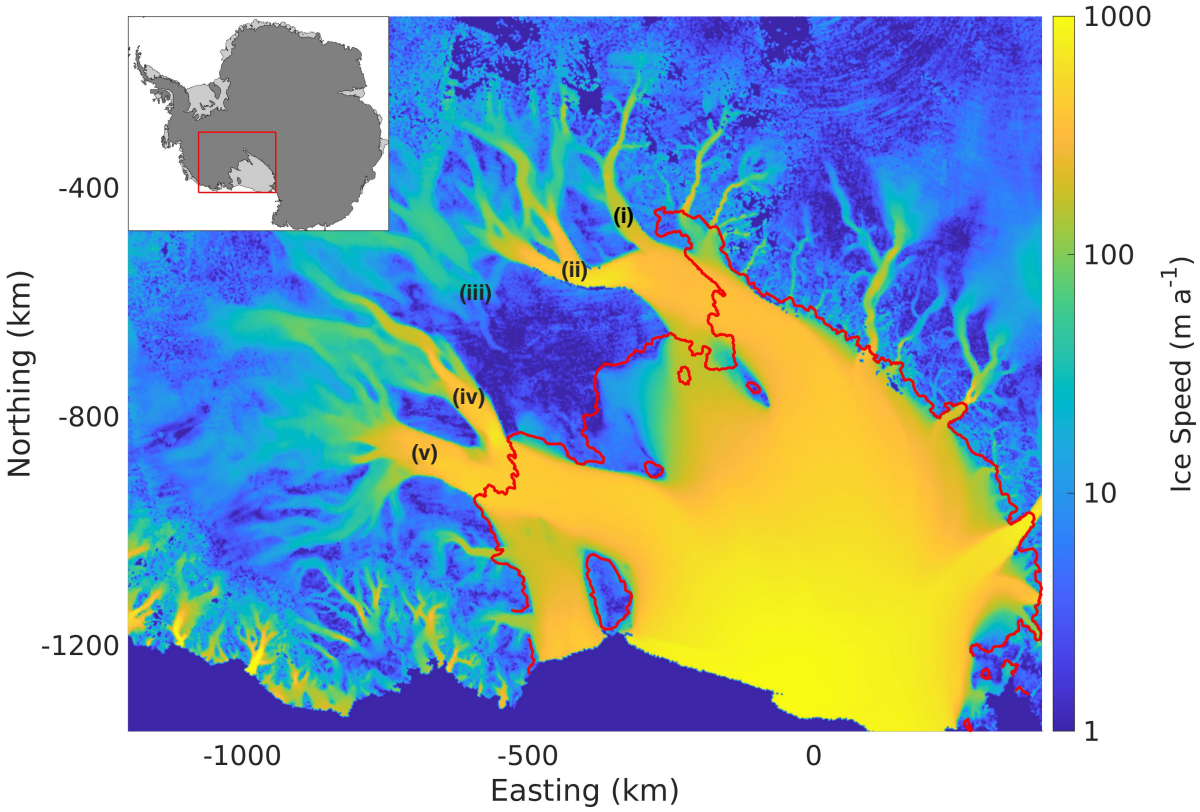

Figure 1.5: Observed ice velocity over the Siple coast and Ross Ice Shelf from Rignot et al. (2011, 2017); Mouginot et al. (2012, 2017). (i) Ice Stream A (Mercer); (ii) Ice Stream B (Whillans); (iii) Ice Stream C (Kamb); (iv) Ice Stream D (Bindschadler); (v) Ice Stream E (MacAyeal). The red line shows the Siple Coast grounding line. The region of Antarctica depicted is given in the upper left corner.

1.5.2 Subglacial lakes

During construction of a global subglacial lake inventory, Livingstone et al. (2022) compiled the location of many subglacial lakes in Antarctica (Fig. 1.6) including many subglacial lakes found underneath the Siple Coast ice streams. They postulated that active subglacial lakes have various drainage patterns with filling and drainage acting on sometimes different timescales. They observed that when lake discharge exceeded the capacity of the subglacial hydrological system, there would be an increase in subglacial water pressure resulting in increased ice flow. This altered ice flow demonstrates the influence that subglacial lakes

and the subglacial drainage system have on Antarctic ice dynamics. Localized studies have found a similar connection between subglacial lake drainage and ice speedup, such as at Byrd Glacier (Stearns et al., 2008), and Whillans and Mercer ice streams (Siegfried et al., 2016).

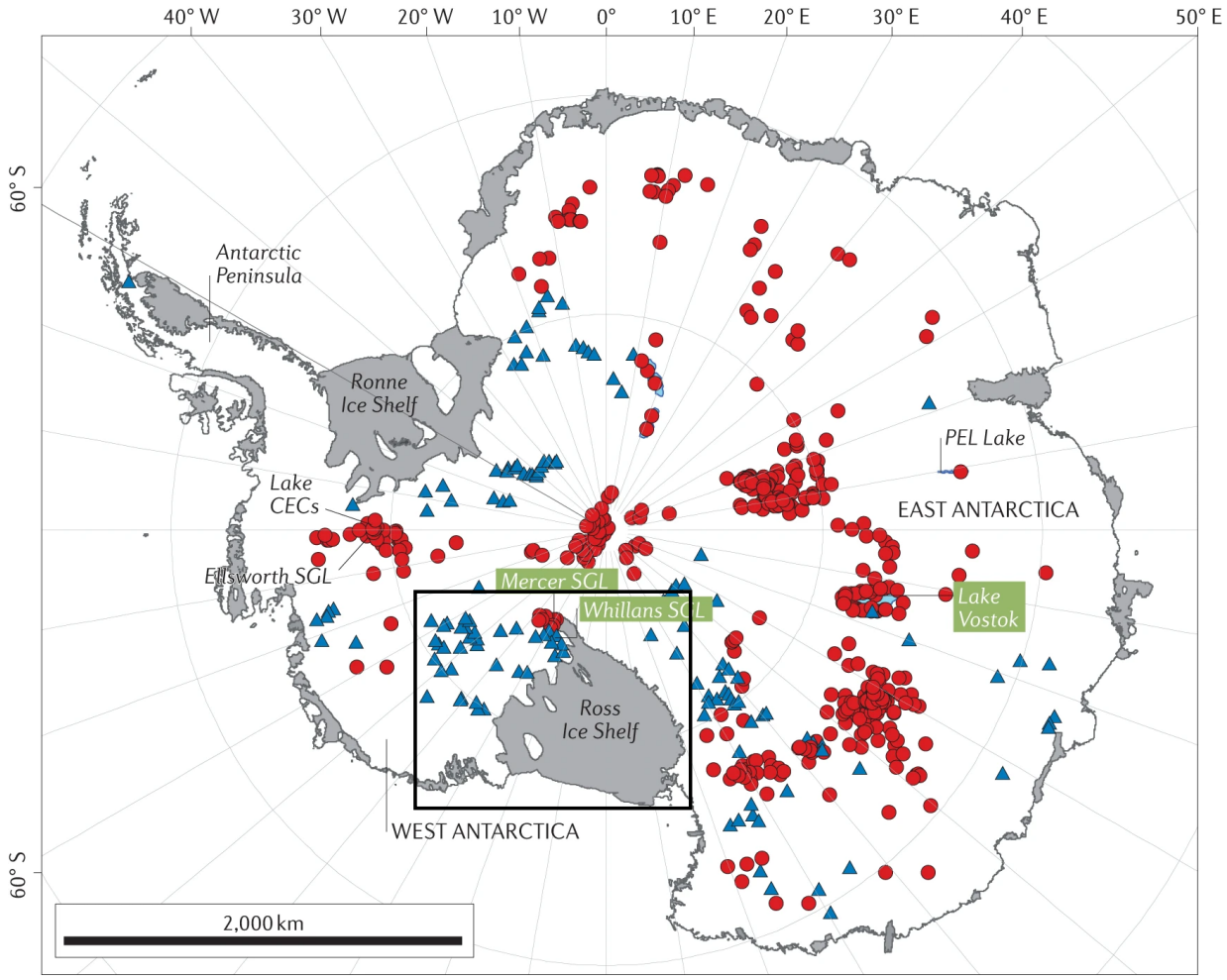

Figure 1.6: Observed Antarctic subglacial lakes adapted from Livingstone et al. (2022). The black box bounds the Ross Ice Shelf and Siple Coast region. Red circles represent stable subglacial lakes which have inflow equal to outflow, blue triangles represent active subglacial lakes, which fill and drain.

Siegfried et al. (2016) used Global Positioning System (GPS) data to study the affect of drainage events of hydraulically connected subglacial lakes under Whillans and Mercer ice streams on ice dynamics. They found that during a first drainage event ice speedup of up to 3.8 % followed close behind the lake drainage, and a deceleration of ice followed soon after. During this drainage event increasing drainage was correlated to increased ice speed. However, during a second drainage event they found that increased drainage was correlated to decreasing ice speed, which demonstrates the complexity of the ice sheet/subglacial hydrology feedback mechanisms. It is possible that the first drainage event initiated a shift to an efficient channelized drainage system where increased discharge in a second drainage event would produce larger channels persisting at higher effective pressures and consequently slow down the ice.

Carter et al. (2017) modeled subglacial lake dynamics with a drainage system that consisted of a distributed sheet with an R-channel or a canal incized into underlying sediment. They found that when the canals were used, the fill/drain timescales of the lakes matched closer to observations. Canals in such weak sediments would suggest the lakes also exist in weak sediments meaning this type of drainage would occur in shallow lakes. They suggested that areas with active subglacial lakes would show more variability in ice flow rates.

Conditions of the ice sheet play a role in the development of subglacial lakes as well. Motivated by subglacial lakes found underneath fast flowing ice streams like those of the Siple Coast, Sergienko and Hulbe (2011) modeled the affect of a "sticky spot" of high basal traction on subglacial lake formation. They found that a sticky spot would reduce ice speed, which would thicken ice near the sticky spot but thin it downstream of the sticky spot. This change in surface gradient would create a hydraulic potential low downstream of the sticky spot, where water would pool and a subglacial lake would form. They suggested that thicker ice over the sticky spot compared to thinner ice upstream could drive water to form a subglacial lake upstream of the sticky spot if the bed topography was favourable for such a formation.

The active subglacial lake and ice stream dynamics, combined with the observed ability for the subglacial hydrologic system and the ice sheet to affect each other, make this an interesting area to study coupled ice/hydrology interactions.

1.6 Layout of Thesis

The goal of this thesis is to determine the relevance of various feedback mechanisms between the subglacial hydrologic system and the ice sheet in the Siple Coast region of Antarctica.

This is accomplished using the Glacier Drainage System (GlaDS) model as a subglacial hydrology model and the Shallow Shelf Approximation (SSA) model as the basis of an ice flow model, with both models implemented in the Ice-sheet and Sea-level System Model (ISSM). Comparisons between model outputs 1) with and without coupling, 2) coupling with and without added components such as basal melt computed from frictional and geothermal heat, and the inclusion of hydrology sheet thickness gradients in driving stress computations allow for the assessment of the importance of various feedback mechanisms between the subglacial hydrological system and the ice sheet.

Chapter two will outline the methods to be used in this thesis. It will begin with a detailed description of the GlaDS model equations, boundary conditions, and initialization. It will continue to outline the SSA equations, the implementation of friction at the glacier base, and the mass transport equation, all to be used in the ice flow model. Boundary conditions and the initialization of the ice flow model including an overview of the inversion technique used to constrain the basal friction coefficient and the ice rigidity will also be given. Alterations to the GlaDS and SSA model equations will be included in this section as well. The coupling process including different coupling components and the coupling initialization will follow. Finally, the chapter will end with a comprehensive list of experiments which were run and a description of the computation of the model domain, and the computational mesh on which the model is solved.

Chapter three will showcase the results of this thesis. It will start by displaying the subglacial hydrological outputs, followed by the outputs of the ice flow-only models. It will follow by showcasing the results of the coupled model, and comparing it to the hydrology-only and ice flow-only models. Next will be a comparison between the coupled models using various friction laws and their corresponding ice flow-only models. This section will close by giving the results of the coupled models with additional coupling components, including 1) melt from geothermal heat flux and frictional heating of ice, 2) including subglacial lake geometry in the glacier driving stress, and 3) a fully coupled model with the melt and driving stress additions. These models with additional coupling components will be compared against each other, and the standard two-way coupled model.

Chapter four will discuss the implications of the results of Chapter three. It will start with a comparison between our understanding of the Ross Sea subglacial hydrologic catchment region from this study compared to the literature on the area. It will continue with a discussion of our present implementation of friction in ice flow models, some of its shortcomings, and potential future avenues to remedy these shortcomings. This will be followed with an analysis of the various feedback mechanisms identified in chapter three. This chapter will close with a discussion of potential future GlaDS improvements, some in the context of two-way coupled modeling.

Chapter five concludes this thesis with a summary of the objectives and its main findings. A path forward for a better representation of basal conditions in ice sheet modeling is presented.

Chapter 2

Methods

Both GlaDS and the ice flow model are implemented in the Ice-Sheet and Sea-Level System Model (Larour et al., 2012, ISSM), which will be used to run all models for this thesis. ISSM uses continuous Galerkin finite element methods, which solve the weak form solution of partial differential equations on unstructured meshes using triangular piecewise linear elements.

This chapter will describe the GlaDS equations in detail, and discuss how GlaDS is initialized, including initial conditions, boundary conditions, and input data. Next, a discussion of the ice flow equations will be given, including the stress balance equations, the mass transport equation, and the friction laws used. Initialization of the ice flow model will follow, including initial conditions, boundary conditions, inversion procedures for unknown parameters, input data, and the spinup procedure. Once GlaDS and the ice flow model have been introduced, the coupling between GlaDS and the ice flow model will be discussed as well as the initialization of the coupled model. Finally, an overview of the creation of the model mesh will be given along with a detailed list of the experiments to be run.

2.1 Glacier Drainage System model

As discussed in the Section 1.3.2, the Glacier Drainage System (GlaDS) model is a two dimensional subglacial hydrology model, which is solved using finite element methods on an unstructured mesh. Each element simulates a linked cavity distributed sheet system and each element edge simulates an R-channel, which is visualized in Fig. (2.1). Both the

distributed sheet and channel systems parameterize opening and closing rates of cavities and channels respectively, and solve a mass conservation equation for the hydraulic potential at each time step. Channels are assumed to be completely filled with water, and the basal environment is assumed to be at pressure melting point, allowing evolution of channels without taking ice temperature gradients into account.

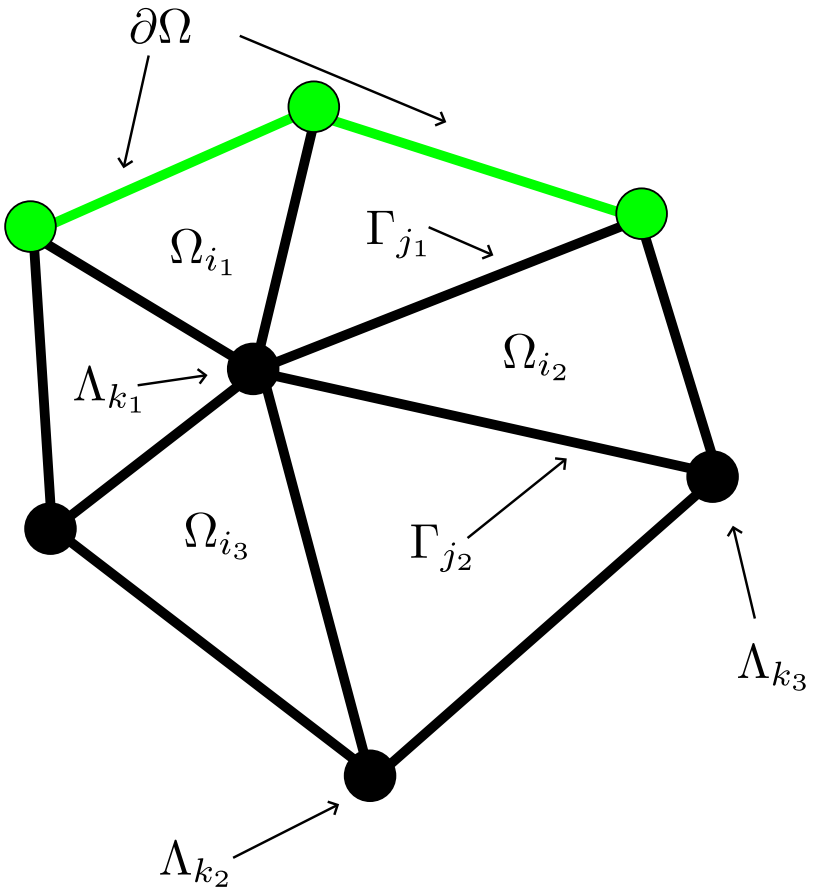

Figure 2.1: GlaDS conceptual model adapted from Werder et al. (2013). The elements which contain a linked cavity distributed sheet system are represented by Ω_i; the element edges which contain R-channels are represented by Γ_J; the nodes are represented by Λ_k. Green represents the domain boundary ($\partial\Omega$).

The choice of GlaDS as the subglacial hydrology model for this thesis is two fold. First,

GlaDS has both inefficient and efficient drainage components, which can form at any part of the domain allowing for a more complete analysis of the subglacial hydrological system. Second, GlaDS operates on an unstructured mesh, which can be refined in areas of fast ice flow, large gradients in bed topography, and close to the grounding line. A model such as the Subglacial Hydrology and Kinetic Transient Interactions (Sommers et al., 2018, SHAKTI) model, which describes a range of inefficient and efficient drainage and is solved on an unstructured mesh could have also been chosen. However, GlaDS has a history of being applied to Antarctic subglacial hydrology modeling (Dow et al., 2018, 2020, 2022; Dow, 2022), so it is therefore the choice for this thesis.

In this section I will cover in detail the GlaDS model equations, and the various alterations to the equations made for this project. The equations are solved by converting to the weak form and using finite element methods, but an analysis of the solution technique will be omitted. A summary of GlaDS variables can be found in Table 2.1 and a summary of parameter values and constants can be found in Table 2.2.

2.1.1 The distributed sheet system

The distributed sheet system is governed by mass conservation, which is given in Eq. (2.1).

$$\frac{\partial h_e}{\partial t} + \frac{\partial h}{\partial t} + \overrightarrow{\nabla} \cdot \overrightarrow{q} = m_s. \tag{2.1}$$

Here h_e is the englacial storage given by Eq. (2.2), e_ν is the englacial void ratio, and ρ_{fw} is the density of freshwater. The mass balance equation says that change in the hydrology sheet thickness and the englacial storage at any point is balanced by flux away from that point and production of water at that point.

$$h_e = e_\nu \frac{\phi - \rho_i g H}{\rho_{fw} g} = e_\nu \frac{p_w}{\rho_{fw} g}. \tag{2.2}$$

The sheet discharge is parameterized as a function of the gradient in the hydraulic potential by a Darcy-Weisbach law given by Eq. (2.3), described in Section 1.3. α_s and β_s are chosen to describe fully turbulent flow. It is important to note that Darcy's law originates from considering flow through a porous medium and turbulence in this context refers to movement through micro cavities favoured over flow through the medium's pores (Fountain

Variable Name	Symbol	Units
Basal shear stress	τ_b	Pa
Basal sliding speed	u_b	$\mathrm{m\,s^{-1}}$
Channel closing rate	ν_c	$\mathrm{W\,m^{-1}}$
Channel cross sectional area	S_c	$\mathrm{m^2}$
Channel coordinate	s_c	
Channel discharge	q_c	$\mathrm{m^3\,s^{-1}}$
Channel dissipation	Ξ	$\mathrm{W\,m^{-1}}$
Channel opening rate	ω_c	$\mathrm{W\,m^{-1}}$
Channel pressure melt	Π	$\mathrm{W\,m^{-1}}$
Channel source term	m_c	$\mathrm{m^2\,s^{-1}}$
Effective pressure	N	Pa
Englacial storage	h_e	m
Geothermal heat flux	G	$\mathrm{W\,m^{-2}}$
Hydraulic potential	ϕ	Pa
Hydrology sheet thickness	h	m
Ice thickness	H	m
Sheet closing rate	ν_s	$\mathrm{m\,s^{-1}}$
Sheet discharge	$\overrightarrow{q}$	$\mathrm{m^2\,s^{-1}}$
Sheet flow parallel to channel	$\tilde{q}_s$	$\mathrm{m^2\,s^{-1}}$
Sheet opening rate	ω_s	$\mathrm{m\,s^{-1}}$
Sheet source term	m_s	$\mathrm{m\,s^{-1}}$
Time	t	s
Water pressure	p_w	Pa

Table 2.1: GlaDS model variables.

and Walder, 1998), which aligns with the physics of a linked cavity system where water flows through cavities and orifices.

$$\overrightarrow{q} = -k_s h^{\alpha_s} \left|\overrightarrow{\nabla}\phi\right|^{\beta_s - 2} \overrightarrow{\nabla}\phi. \tag{2.3}$$

The time evolution of the hydrology sheet thickness is given by Eq. (2.4) parameterized by an opening (ω_s) and a closing (ν_s) rate given by Eq. (2.5) and Eq. (2.6) respectively.

Parameter	**Value**	**Units**
Bedrock bump height (h_r)	0.08	m
Cavity spacing (ℓ_r)	2	m
Channel conductivity (k_c)	$5 \cdot 10^{-2}$	$\mathrm{m}^{3/2}\,\mathrm{kg}^{-1/2}$
Channel opening cap ($S_{c,\max}$)	100	m^2
Englacial void ratio (e_ν)	10^{-5}	
First flow exponent (α_c, α_c)	5/4	
Fresh water density (ρ_{fw})	1000	$\mathrm{kg\,m}^{-3}$
Glen's flow constant (n)	3	
Gravitational acceleration (g)	9.81	$\mathrm{m\,s}^{-2}$
Heat capacity of water (c_w)	4.22	$\mathrm{J\,g}^{-1}\,\mathrm{K}^{-1}$
Ice density (ρ_i)	910	$\mathrm{kg\,m}^{-3}$
Ice flow constant ($\tilde{A}_c$, $\tilde{A}_s$)	$2.5 \cdot 10^{-25}$	$\mathrm{Pa}^3\,\mathrm{s}^{-1}$
Latent heat (L)	334	$\mathrm{J\,g}^{-1}$
Pressure melt coefficient (c_t)	$7.5 \cdot 10^{-8}$	$\mathrm{K\,Pa}^{-1}$
Second flow exponent (β_c, β_c)	3/2	
Sheet conductivity (k_s)	10^{-3}, $5 \cdot 10^{-3}$	$\mathrm{m}^{7/4}\,\mathrm{kg}^{-1/2}$
Sheet opening cap (h_c)	100	m
Sheet width below channel (l_c)	2	m

Table 2.2: GlaDS model parameters and constants.

$$\frac{\partial h}{\partial t} = \omega_s - \nu_s. \tag{2.4}$$

$$\omega_s = \begin{cases} u_b(h_r - h)/\ell_r & h < h_r \\ 0 & \text{otherwise} \end{cases}. \tag{2.5}$$

$$\nu_s = \begin{cases} \tilde{A}_s h_c \left|N\right|^{n-1} N & h \geq h_c \cap N < 0 \\ \tilde{A}_s h \left|N\right|^{n-1} N & \text{otherwise} \end{cases}. \tag{2.6}$$

Here, h_r is the typical bedrock bump height, ℓ_r is the typical cavity spacing, $\tilde{A}_s$ is the ice rheological constant ($\tilde{B}^{-n}$) multiplied by an order one factor related to the cavity

geometry, which is given by $2/n^n$, N is the effective pressure given by Eq. (2.7), h_c is a constant determining a maximum rate of sheet opening when $N < 0$, and B is the bed elevation.

$$N = \rho_i g H + \rho_{fw} g B - \phi + \rho_{fw} g h. \tag{2.7}$$

The hydrology sheet opens due to sliding when h is below the typical bedrock bump height. The hydrology sheet closes due to ice creep, but when the effective pressure becomes negative (water pressure exceeds ice overburden pressure) the closing rate functions as an opening rate term for subglacial lakes. To avoid numerical instabilities when the closing turned opening rate term is in effect, we compute the effective pressure at the ice/water interface as opposed to the bed, which means adding $\rho_{fw} g h$ to the effective pressure (Eq. 2.7). This will increase the effective pressure as the lake fills until it reaches equilibrium. We also cap ν_s when h exceeds a certain threshold (h_c) to further avoid runaway values of lake growth.

m_s is determined using either a prescribed melt rate, or melt due to geothermal heat flux (G) and frictional melting of ice, given by Eq. (2.8),

$$m_s = \frac{G + \tau_b u_b}{\rho_i L}, \tag{2.8}$$

where L is the latent heat of melting.

With the paramterization of the discharge, hydrology sheet opening, and the englacial storage as a function of the hydraulic potential, Eq. (2.1) becomes a second order parabolic partial differential equation for the hydraulic potential. The form of Eq. (2.1) differs from the mass conservation equation (Eq . 1.12) given in Section 1.3 as it has an added englacial storage component ($\frac{\partial h_e}{\partial t}$). This englacial storage, which increases with water pressure, is necessary to explain changes in water storage on timescales that are faster than opening due to sliding over a cavitated bed and closure due to ice creep.

2.1.2 The channel system

Like the distributed sheet system, channels are governed by conservation of mass, given by Eq. (2.9),

$$\frac{\partial S_c}{\partial t} + \frac{\partial q_c}{\partial s_c} = \frac{\Xi - \Pi}{\rho_{fw} L} + m_c, \tag{2.9}$$

where Ξ is the rate of dissipation of potential energy per unit length of the channel and per unit time, Π is the rate of change of sensible heat per unit length of the channel due to changes in the pressure melting point, and m_c is the rate of flow of water from the adjacent sheet into the channel. The mass balance equation says that change in channel cross sectional area at any point along the length of the channel is balanced by the flux of water to or from that point of the channel, water input to that point in the channel, and water gained through dissipation of potential energy as heat, taking into account changes in pressure melting point.

The channel discharge is given by a Darcy-Weisbach parameterization of the hydraulic potential (Eq. 2.10), where α_c and β_c are chosen so that the flow is fully turbulent.

$$q_c = -k_c S_c^{\alpha_c} \left| \frac{\partial \phi}{\partial s_c} \right|^{\beta_c - 2} \frac{\partial \phi}{\partial s_c}. \tag{2.10}$$

The time evolution of the channel cross sectional area (Eq. 2.11) is given by a parameterization of the channel opening rate (ω_c) from melt due to dissipation of potential energy in the form of heat, taking into account changes in pressure melting point and a parameterization of the channel closing rate (ν_c) due to viscous creep of ice. The opening rate is given by Eq. (2.12), and the closing rate is given by Eq. (2.13), which unlike the sheet closing rate does not allow for opening when $N < 0$.

$$\frac{\partial S_c}{\partial t} = \omega_c - \nu_c. \tag{2.11}$$

$$\omega_c = \frac{\Xi - \Pi}{\rho_i L}. \tag{2.12}$$

$$\nu_c = \begin{cases} 0 & N < 0 \\ \tilde{A}_c S \left| N \right|^{n-1} N & N \geq 0 \end{cases}. \tag{2.13}$$

Here, $\tilde{A}_c$ is the ice rheological constant ($\tilde{B}^{-n}$) multiplied by an order one factor depending on the cross sectional geometry of the channel, taken to be $2/n^n$, the same as in the distributed sheet system. The channel cross sectional area is capped at $100\,\mathrm{m}^2$ to prevent runaway channel growth. A cap of $500\,\mathrm{m}^2$ was also tested, but caused large sections of the hydrology sheet under Ice Stream B to have a thickness above the typical bedrock bump height, so the $100\,\mathrm{m}^2$ cap is used in all hydrology models. The dissipation of potential energy per unit length and time is given by Eq. (2.14),

$$\Xi = \left| q_c \frac{\partial \phi}{\partial s_c} \right| + \left| l_c \tilde{q}_s \frac{\partial \phi}{\partial s_c} \right|, \tag{2.14}$$

where l_c is the width of the sheet below the channel and $\tilde{q}_s$ is the approximate discharge of the sheet into the channel, given by Eq. (2.15). This takes into account the change in potential energy that a particle of water experiences moving down the channel, as well as the change in potential energy that a particle of water experiences moving into the channel from the sheet.

$$\tilde{q}_s = -k_s h^{\alpha_s} \left| \frac{\partial \phi}{\partial s_c} \right|^{\beta_s - 2} \frac{\partial \phi}{\partial s_c}. \tag{2.15}$$

The rate of change of sensible heat due to changes in pressure melting point is given by Eq. (2.16),

$$\Pi = -c_t c_w \rho_{fw} \left(q_c + f l_c \tilde{q}_s \right) \frac{\partial p_w}{\partial s_c}, \tag{2.16}$$

where c_t is the pressure melt coefficient (rate of change of melting point per unit of temperature), c_w is the specific heat capacity of water, and f is a constant acting as a switch, equal to 1 when the channel has a non zero cross sectional area or water from the surrounding sheet is flowing into the channel and 0 otherwise. Eq. (2.16) takes into account the change in temperature a particle of water experiences due to moving along the length of the channel, and the change in temperature a particle of water experiences from moving from the adjacent sheet into the channel.

Exchange of water with the adjacent hydrology sheet is used to determine m_c. If Ω_{i1} and Ω_{i2} are the two elements bordering a channel (Fig. 2.1), and $\overrightarrow{n}_{\Omega_{i1}}$ and $\overrightarrow{n}_{\Omega_{i2}}$ are the corresponding outward unit normal vectors to the channel, then m_c is given by Eq. (2.17).

$$m_c = \overrightarrow{q} \cdot \overrightarrow{n}_{\Omega_{i1}} + \overrightarrow{q} \cdot \overrightarrow{n}_{\Omega_{i2}}. \tag{2.17}$$

Conservation of mass requires that the inflow to the node must equal outflow from the node, where channels meet at nodes in the mesh (Fig. 2.1). For a given node Λ_k, conservation of mass at the node is given by Eq. (2.18),

$$\sum_j Q_j^k = 0, \tag{2.18}$$

where Q_j^k is the discharge from channel Γ_j into node Λ_k. At nodes where input from moulins is considered Eq. (2.18) must be modified, however, for this project surface melt, and therefore moulins, are not of concern.

2.1.3 Model initialization

GlaDS requires a set of initial conditions and boundary conditions in order to run. Initial conditions can be lenient if the intention of the run is to go to steady state, but if running with a coupled ice flow model or with transient changes in water input, ice speed, or ice geometry change, then initial conditions should represent a steady state hydrologic system for the given forcing at the start of the model run. Boundary conditions on the hydraulic potential are taken to be either Dirichlet or Neumann depending on the assumed physics at the glacier boundary discussed below (hydrostatic equilibrium at the ocean requires a Dirichlet boundary condition).

The model domain is the Ross Sea hydraulic catchment (Fig 2.2) assuming overburden hydraulic potential (ϕ_0), given by Eq. (2.19), where the water pressure is equal to the ice overburden pressure throughout the entire domain.

$$\phi_0 = \rho_i g H + \rho_w g B. \tag{2.19}$$

The Transantarctic Mountains on the Eastern side of the Ross Ice Shelf were carefully masked out of the domain by taking away areas where ice thickness was less than 100 m, and areas with model instability. At the grounding line (ice/ocean interface), a Dirichlet

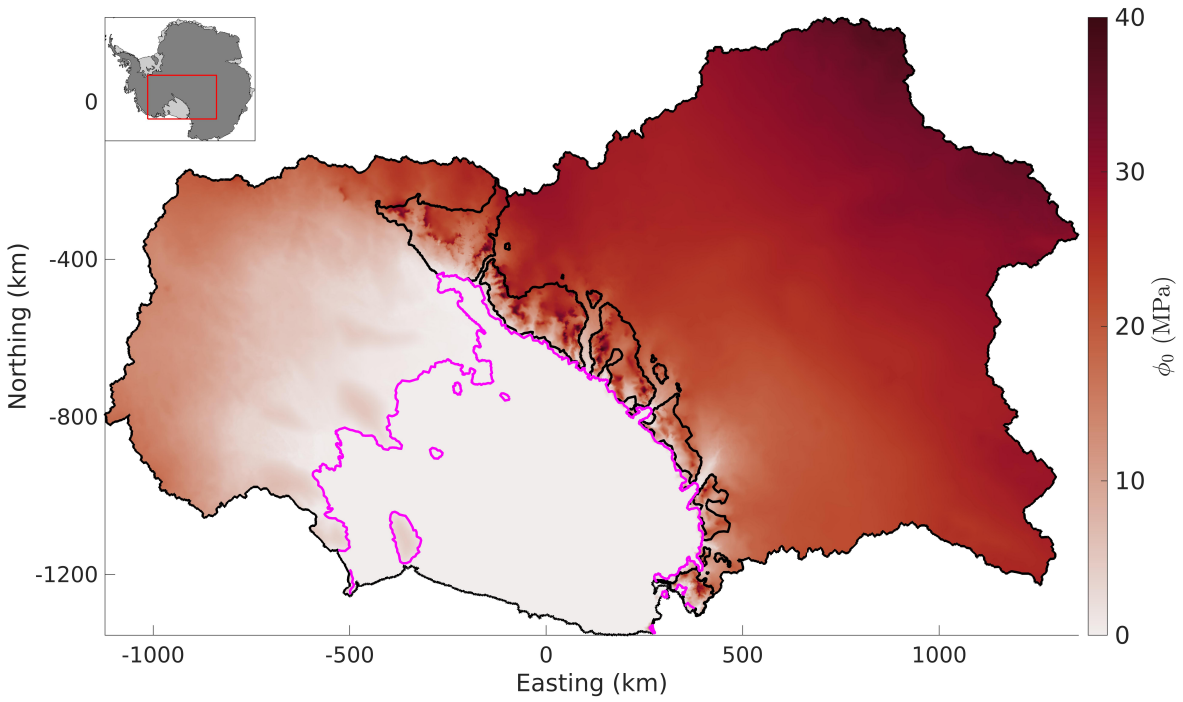

Figure 2.2: Overburden hydraulic potential for the Ross Sea subglacial hydrologic catchment (MPa). The black lines represents the domain boundary, and the pink lines represent grounding lines.

boundary condition of $\phi|_{\partial\Omega_\mathcal{O}} = 0$ is applied, where $\partial\Omega_\mathcal{O}$ is the grounding line. This ensures that the hydrologic system is in hydrostatic equilibrium with the ocean at the grounding line, and the transition of the water pressure in the subglacial hydrologic system to the water pressure in the ocean is continuous. In areas in the mountains where there is land termination of ice, a Dirichlet boundary condition of $\phi|_{\partial\Omega_\mathcal{T}} = \rho_w g B$ is applied where $\partial\Omega_\mathcal{T}$ is the part of the domain boundary with land terminating ice. This ensures water pressure is equal to atmospheric pressure. The rest of the domain $\partial\Omega_\mathcal{N}$ is the hydraulic catchment boundary, which means no water is flowing in or out of the domain at these points and zero Neumann flux is applied ($\frac{\partial\phi}{\partial\tilde{n}} = 0$, where $\tilde{n}$ is the unit direction normal to the domain boundary). However, once the ice sheet geometry begins to change this boundary is not necessarily the boundary of the hydraulic catchment. Therefore, in areas where water begins to pool, a Dirichlet boundary condition of the hydraulic potential which allowed for that pooling water is applied, which means water can exit the domain in these regions.

If no prior model runs have been made, then the hydrology sheet thickness is initialized to 3 cm, the channel area is initialized to $0\,m^2$, and the hydraulic potential is initialized to $\phi(t = 0) = \rho_i g H/2$. If prior models have been run then hydrology sheet thickness, hydraulic potential, and channel cross sectional area from the final time step of a prior model will be used to initialize the new model.

Bed topography is taken from BedMachine Antarctica v3 (Morlighem et al., 2020), while surface topography and ice thickness are taken from the ice flow model if running a coupled model and from Morlighem et al. (2020) otherwise. Ice velocity data is taken from the ice flow model if running a coupled model and from MEaSUREs v2 (Rignot et al., 2011, 2017; Mouginot et al., 2012, 2017) otherwise. If using Eq. (2.8) to compute m_s, the basal shear stress is estimated using a series of inversions described in Section 2.2.4. Otherwise melt is taken from the initMIP Antarctica JPL-ISSM control run final time step (Seroussi et al., 2019), which used a thermomechanical model to determine basal melt water production. If GlaDS is run coupled to the ice flow model then the glacier geometry, ice speed, and basal shear stress are temporally variable, but if GlaDS is run uncoupled then they are temporally constant.

2.2 Ice Flow Model

Following Section 1.1, the ice flow model assumes conservation of momentum using the SSA, with a friction law relating the basal shear stress to the effective pressure and ice speed, and conservation of mass using a mass transport equation. Like GlaDS, the ice flow model is two dimensional and is solved using finite element methods. The SSA is depth averaged, and assumes that vertical shear is negligible. Since the SSA only has two unknowns and is two dimensional, it is computationally inexpensive to solve compared to the Full Stokes equations. The trade off is that it will not capture the physics of when vertical shear is not negligible such as the onset of fast flowing ice streams, which are present in the Siple Coast.

This section will begin with a statement of the SSA equations and alterations to the equations to account for the variations in ice geometry from subglacial lakes. It will continue to give an overview of the friction laws used to determine the basal shear stress. Following will be a brief explanation of the mass transport equation, and this section will close with the model initialization procedure. Ice flow model variables are summarized in Table 2.3 and ice flow model parameters and constants are given in Table 2.4.

Variable Name	Symbol	Units
Basal mass balance	$\dot{M}_b$	$\mathrm{m\,s^{-1}}$
Basal shear stress	τ_b	Pa
Basal sliding velocity	$\overrightarrow{u}$, $\overrightarrow{u_b}$	$\mathrm{m\,s^{-1}}$
Budd friction coefficient	α_b	$\mathrm{s^{1/2}\,m^{-1/2}}$
Depth averaged effective viscosity	$\bar{\mu}$	$\mathrm{Pa\,s}$
Effective pressure	N	Pa
Effective viscosity	μ	$\mathrm{Pa\,s}$
Hydrology layer thickness	h_l	m
Hydrology-modified friction coefficient	C	$\mathrm{kg^{1/2}\,m^{-2/3}\,s^{-5/6}}$
Hydrology sheet thickness	h	m
Ice thickness	H	m
Ice surface elevation	S	m
x component of τ_b	$\tau_{b,x}$	Pa
Schoof friction coefficient	C_s	$\mathrm{kg^{1/2}\,m^{-2/3}\,s^{-5/6}}$
Sliding regime measure	ξ	
Surface mass balance	$\dot{M}_s$	$\mathrm{m\,s^{-1}}$
x component of $\overrightarrow{u}$	u	$\mathrm{m\,s^{-1}}$
y component of τ_b	$\tau_{b,y}$	Pa
y component of $\overrightarrow{u}$	v	$\mathrm{m\,s^{-1}}$

Table 2.3: Ice flow model variables.

2.2.1 The Shallow Shelf Approximation

The SSA, mentioned in Section 1.1, is stated again here in Eq. (2.20).

$$\begin{aligned}
\frac{\partial}{\partial x}\left(4H\bar{\mu}\frac{\partial u}{\partial x}+2H\bar{\mu}\frac{\partial v}{\partial y}\right)+\frac{\partial}{\partial y}\left(H\bar{\mu}\frac{\partial u}{\partial y}+H\bar{\mu}\frac{\partial v}{\partial x}\right)+\tau_{b,x}&=\rho_i g H\frac{\partial S}{\partial x},\\
\frac{\partial}{\partial y}\left(4H\bar{\mu}\frac{\partial v}{\partial y}+2H\bar{\mu}\frac{\partial u}{\partial x}\right)+\frac{\partial}{\partial x}\left(H\bar{\mu}\frac{\partial u}{\partial y}+H\bar{\mu}\frac{\partial v}{\partial x}\right)+\tau_{b,y}&=\rho_i g H\frac{\partial S}{\partial y}.
\end{aligned} \tag{2.20}$$

The right hand sides of the two equations represent the driving stress due to surface slope, τ_{bi} represent the components of the basal shear stress, the first terms on the left hand side of the equations represent compressive and extensional strain and the second terms on the left hand side represent shear strain. The equations therefore read that driving stress is balanced by basal shear stress, compressive, extensional, and shear strain.

Parameter	**Value**	**Units**
Bedrock bump height (h_r)	0.08	m
Cavity spacing (ℓ_r)	2	m
Coupling strength constant (ζ)	10^7, $2 \cdot 10^7$, $3 \cdot 10^7$	$\mathrm{m}^{-4}\,\mathrm{kg}\,\mathrm{s}$
First Budd friction exponent (r)	1	
Glen's flow constant (n)	3	
Gravitational acceleration (g)	9.81	$\mathrm{m}\,\mathrm{s}^{-2}$
Ice density (ρ_i)	910	$\mathrm{kg}\,\mathrm{m}^{-3}$
Ice flow constant ($\tilde{A}$)	$2.5 \cdot 10^{-25}$	$\mathrm{Pa}^3\,\mathrm{s}^{-1}$
Iken's bound ($C_{\max}$)	0.5	
Schoof/hydrology friction exponent (m)	1/3	
Second Budd friction exponent (s)	1/3	

Table 2.4: Ice flow model parameters and constants.

Subglacial lakes have the ability to raise and lower the ice surface as they fill and drain (Livingstone et al., 2022), which can alter the driving stress of the glacier. When the hydrology sheet thickness in GlaDS is less than the typical bedrock bump height then the ice is in contact with bedrock protrusions (Fig. 2.3). However, when the hydrology sheet thickness exceeds the typical bedrock bump height the ice base and consequently the ice surface is lifted up a distance $h - h_r$. Using the linearity of the differential operator, we can add these ice elevation changes to the SSA, which we can implement as Eq. (2.21),

$$\begin{aligned}
\frac{\partial}{\partial x}\left(4H\bar{\mu}\frac{\partial u}{\partial x} + 2H\bar{\mu}\frac{\partial v}{\partial y}\right) + \frac{\partial}{\partial y}\left(H\bar{\mu}\frac{\partial u}{\partial y} + H\bar{\mu}\frac{\partial v}{\partial x}\right) + \tau_{b,x} &= \rho_i g H \frac{\partial}{\partial x}(S + h_l), \\
\frac{\partial}{\partial y}\left(4H\bar{\mu}\frac{\partial v}{\partial y} + 2H\bar{\mu}\frac{\partial u}{\partial x}\right) + \frac{\partial}{\partial x}\left(H\bar{\mu}\frac{\partial u}{\partial y} + H\bar{\mu}\frac{\partial v}{\partial x}\right) + \tau_{b,y} &= \rho_i g H \frac{\partial}{\partial y}(S + h_l), \\
h_l &= \begin{cases} 0 & h \le h_r \\ h - h_r & h > h_r \end{cases},
\end{aligned} \tag{2.21}$$

where h_l is the hydrology layer thickness representing the distance that the ice raised up due to a subglacial lake.

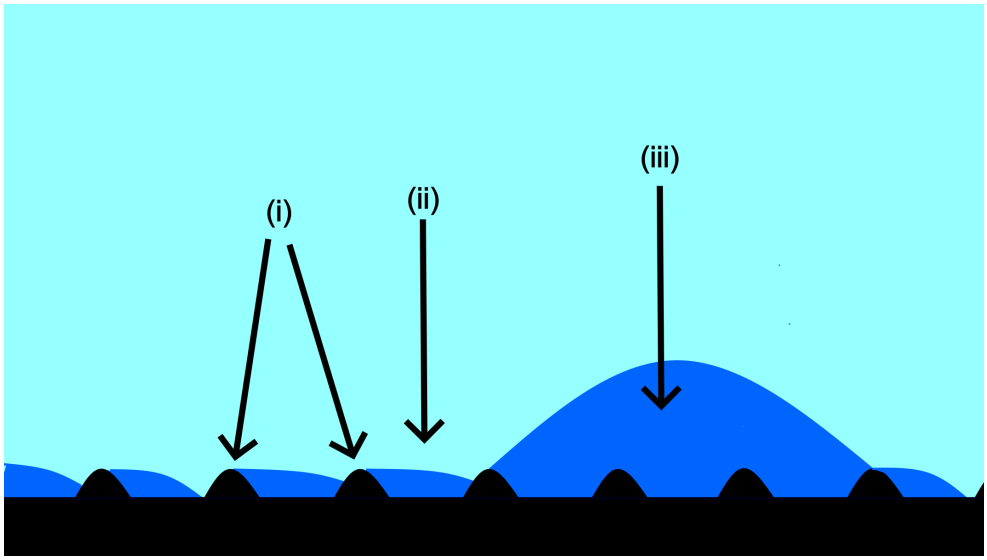

Figure 2.3: Conceptual model of a subglacial lake altering ice geometry. Black represents the glacier bed, dark blue represents subglacial water, and light blue represents glacier ice. (i) is bedrock protrusions of height h_r and spacing l_r; (ii) is a water filled cavity where the ice base lies on the bedrock protrusions; (iii) represents a subglacial lake where the ice is no longer in contact with the glacier bed, raised up a distance $h - h_r$.

2.2.2 A hydrology-modified regularized coulomb friction law

To determine the basal shear stress in the SSA a friction law must be used. In ISSM the "Schoof friction law" is implemented as Eq. (2.22).

$$\tau_b = \frac{C_s^2 \, |\overrightarrow{u_b}|^{m-1}}{(1 + (C_s^2/(C_{\max} N))^{1/m} \, |\overrightarrow{u_b}|)^m} \overrightarrow{u_b}, \tag{2.22}$$

where C_s is the basal friction coefficient, $C_{\max}$ is Iken's bound, and $m = 1/n$ is a friction law exponent. This friction law is actually a specific case of the friction law proposed by Gagliardini et al. (2007) described in Section 1.4. The Schoof friction law in ISSM assumes that $q = 1 \implies \alpha = 1$, C from Section 1.4 is now called $C_{\max}$, and A_s from Section 1.4 is now called $(C_s^2)^{-n}$. These Schoof and Gagliardini friction laws were designed considering sliding over a system of linked cavities. They encompass the continuum between a Weertman sliding regime where cavities have not yet opened up, and a regime where the ratio of basal shear stress to effective pressure has hit a maximum as proposed first by Iken (1981), which I will refer to hereafter as an Iken sliding regime.

Eq. 2.22 can be rewritten in scalar form as Eq. 2.23,

$$\tau_b = \frac{C_s^2 u_b^m}{(1+\xi)^m}, \tag{2.23}$$

where $\xi = (C_s^2/(C_{\max}N))^{1/m} u_b$ is a dimensionless variable describing the extent to which cavitation plays a role in basal sliding. In the limit where $\xi \to 0$ we get a Weertman sliding regime, where $\tau_b = C_s^2 u_b^m$. In the limit where $\xi \to +\infty$ we get an Iken sliding regime where $\tau_b = C_{\max}N$. The basal friction coefficient, C_s, is often solved for using inversion techniques, while $C_{\max}$ is held constant (McArthur et al., 2023; Brondex et al., 2017, 2019). However, it is immediately clear that an inversion for C_s alone is insufficient to determine the basal shear stress where $\xi \to +\infty$. Likewise, an inversion for $C_{\max}$ alone would be insufficient to determine the basal shear stress in regions where $\xi \to 0$. If using the Schoof friction law an inversion for both C_s and $C_{\max}$ should be performed to account for the full range of possible sliding regimes in the Schoof friction law.

Determination of C_s and $C_{\max}$ for a given τ_b is a system of one equation in two unknowns and therefore has an infinite number of solutions. However, the goal of a friction law is not only to determine the basal shear stress at a snapshot in time, but to describe subglacial conditions, and more specifically subglacial hydrological conditions in cases with explicit dependence on the effective pressure. Since we have two parameters we can vary, and one equation relating the basal shear stress to these parameters (Eq. 2.22), we have one more equation to describe these subglacial conditions as best as possible. To find this second equation, we propose that the sliding regime of the Schoof friction law given by ξ should be a function of the degree to which cavitation plays a role in basal sliding, which in GlaDS is given by the hydrology sheet thickness. We look to rewrite ξ as a function of h by using the GlaDS sheet equations to approximate u_b/N^n. Assuming the hydrology sheet is in steady state ($\frac{\partial h}{\partial t} = 0$), below the typical bedrock bump height ($h < h_r$) and there is positive effective pressure ($N > 0$) we arrive at Eq. 2.24.

$$0 = u_b(h_r - h)/\ell_r - \tilde{A}hN^n. \tag{2.24}$$

With some rearrangement we find

$$\frac{u_b}{N^n} = \frac{\tilde{A}\ell_r h}{h_r - h}, \tag{2.25}$$

plugging u_b/N^n from Eq. 2.25 into the definition of ξ, we get Eq. 2.26, now free of the dependence of u_b and N.

$$\xi = \left(\frac{C_s^2}{C_{\max}}\right)^n \frac{\tilde{A}\ell_r h}{h_r - h}. \tag{2.26}$$

$\tilde{A}$ and ℓ_r are taken to be constant in GlaDS, meaning that the sliding regime depends entirely on the hydrology sheet thickness and the ratio of C_s^2 to $C_{\max}$. To ensure that the same degree of cavitation produces the same sliding regime over the entire domain we require that $C_s^2/C_{\max} = \zeta$ where ζ is some constant, which controls the the degree of cavitation where a Weertman sliding regime will transition to an Iken sliding regime. We therefore propose a modified form of the Schoof friction law (Eq. 2.27), where the determination of the basal friction coefficient, C, will now give both the appropriate basal shear stress for the given sliding velocity and effective pressure, and the correct sliding regime for the given hydrology sheet thickness. This modified friction law can also be implemented using the hydrology sheet thickness instead of the effective pressure as in Eq. 2.28, where $\tilde{\zeta} = \zeta^n \tilde{A}\ell_r$.

$$\tau_b = \frac{C^2 \, |\overrightarrow{u_b}|^{m-1}}{(1 + (\zeta/N)^{1/m} \, |\overrightarrow{u_b}|)^m} \overrightarrow{u_b}. \tag{2.27}$$

$$\tau_b = \frac{C^2 \, |\overrightarrow{u_b}|^{m-1}}{h_r + h(\tilde{\zeta} - 1)} \overrightarrow{u_b}. \tag{2.28}$$

The same analysis can be applied for the general Gagliardini friction law (Eq. 1.21), where $C^n A_s$ is required to be held constant; such an analysis is omitted here as such a friction law will not be applied to this project.

To test the impact of having a sliding regime that is dependent on the degree of cavitation at the glacier bed on coupling, the Budd friction law, the Schoof friction law, and the modified Schoof friction law (that we refer to hereafter as the hydrology-modified Schoof friction law) are applied and their model outputs are compared. The effective pressure used in these friction laws is capped at 3 % of ice overburden pressure (when $N < 0.03 p_i$ an effective pressure of $0.03 p_i$ is used in the friction law) to avoid low values of the basal shear

stress, which arise as a result of low effective pressure, causing unphysically large speedups of ice. This cap limits the physics which is captured by these friction laws and displays a need to further investigate the implementation of basal friction in ice flow models moving forwards.

2.2.3 Mass transport equation

While the SSA equations describe the velocity at which the ice moves, a mass transport equation is needed to update the geometry of the glacier due to this ice velocity. The mass transport equation is given by Eq. (2.29).

$$\frac{\partial H}{\partial t} + \vec{\nabla} \cdot (H \vec{u}) = \dot{M}_s + \dot{M}_b. \tag{2.29}$$

Here, $\dot{M}_s$ is the local change in surface mass balance due to accumulation and ablation and $\dot{M}_b$ is the basal mass balance due to melting and freezing of ice at the glacier base. The mass transport equation says that change in thickness at any given point is balanced by movement of ice away from that point and the ice which has been locally added to that point.

2.2.4 Model initialization

The ice flow model uses the same domain as GlaDS, with the addition of the Ross Ice Shelf. The SSA stressbalance equations use Dirichlet type boundary condition of $\vec{u} = \vec{u}^{\text{obs}}$ over the entire boundary of the two dimensional domain (including the mountainous regions which have been masked out of the domain), where $\vec{u}^{\text{obs}}$ is the observed ice velocity from MEaSUREs v2 (Rignot et al., 2011, 2017; Mouginot et al., 2012, 2017). The mass transport model uses a Dirichlet boundary condition of $H = H^{\text{obs}}$ where H^{obs} is the observed ice thickness from BedMachine Antarctica v3 (Morlighem et al., 2020), applied at the same location as the boundary conditions for the stressbalance model. The ice velocity is initialized to that from MEaSUREs v2 (Rignot et al., 2011, 2017; Mouginot et al., 2012, 2017) and the ice thickness is initialized to that from BedMachine Antarctica v3 (Morlighem et al., 2020).

The bed topography is taken from Morlighem et al. (2020), the effective pressure and hydrology layer thickness (h_l) are taken as an output from GlaDS or a coupled model

run. The surface mass balance in the mass transport model is taken from CESM2 (Kittel et al., 2021) and basal mass balance is either taken as a prescribed melting rate from the initMIP-Antarctica control run final time step (Seroussi et al., 2019) or given by Eq. (2.8) on grounded ice. This is consistent with the melt added into the distributed sheet system of GlaDS. On floating ice, basal mass balance is taken from Adusumilli et al. (2020).

To match the initial ice velocity to that observed from Rignot et al. (2011, 2017); Mouginot et al. (2012, 2017) the basal shear stress and the ice rigidity must be determined. This is accomplished by performing inversions for the basal friction coefficient in the hydrology-modified Schoof friction law over the grounded part of the domain and inversions for the ice rigidity over the floating ice shelf. The inversion involves choosing parameters $\overrightarrow{z}$ (which are either the basal friction coefficient or the ice rigidity) that minimize a cost function $\mathcal{J}$. This is achieved using a variational process described in detail by Nardi et al. (2009). With an initial estimate of $\overrightarrow{z}$ at time t_0, the model is run one time step to t_1 to achieve the model output ice velocity $\overrightarrow{u}$. The gradient of the cost function with respect to the input variables $\frac{\partial \mathcal{J}}{\partial \overrightarrow{z}}$ is computed and then multiplied by the adjoint $\frac{\partial \overrightarrow{u}(t_0)}{\partial \overrightarrow{u}(t_1)}$ to estimate the gradient of $\mathcal{J}$ at the initial time. An M1QN3 minimization algorithm (Gilbert and Lemarechal, 1989) is then used to compute the next guess of $\overrightarrow{z}$ and the process repeats until a convergence criteria is met. This process is illustrated in Fig. (2.4) adapted from Nardi et al. (2009).

The cost function $\mathcal{J}$ is composed of three component cost functions $\mathcal{J}_a$, $\mathcal{J}_l$, $\mathcal{J}_t$. $\mathcal{J}_a$ is given by Eq. (2.30),

$$\mathcal{J}_{\mathrm{a}}(\overrightarrow{u}) = \iint_{\Sigma} \frac{1}{2} \left(\left(u - u^{\mathrm{obs}}\right)^2 + \left(v - v^{\mathrm{obs}}\right)^2 \right) d\Sigma, \tag{2.30}$$

where u^{obs} and v^{obs} are the x and y components of the observed ice speed from Rignot et al. (2011, 2017); Mouginot et al. (2012, 2017) respectively, and Σ is the two dimensional domain. $\mathcal{J}_l$ is given by Eq. (2.31),

$$\mathcal{J}_{\mathrm{l}}(\overrightarrow{u}) = \iint_{\Sigma} \left(\log \left(\frac{||\overrightarrow{u}|| + \varepsilon}{||\overrightarrow{u}^{\mathrm{obs}}|| + \varepsilon} \right) \right)^2 d\Sigma, \tag{2.31}$$

where ε is a small constant close to machine precision to avoid division by 0 when the observed ice speed is 0. $\mathcal{J}_t$ is given by Eq. (2.32),

$$\mathcal{J}_{\mathrm{t}}(\overrightarrow{u}) = \iint_{\Sigma} \frac{1}{2} \left| \overrightarrow{\nabla} \kappa \right|^2 d\Sigma, \tag{2.32}$$

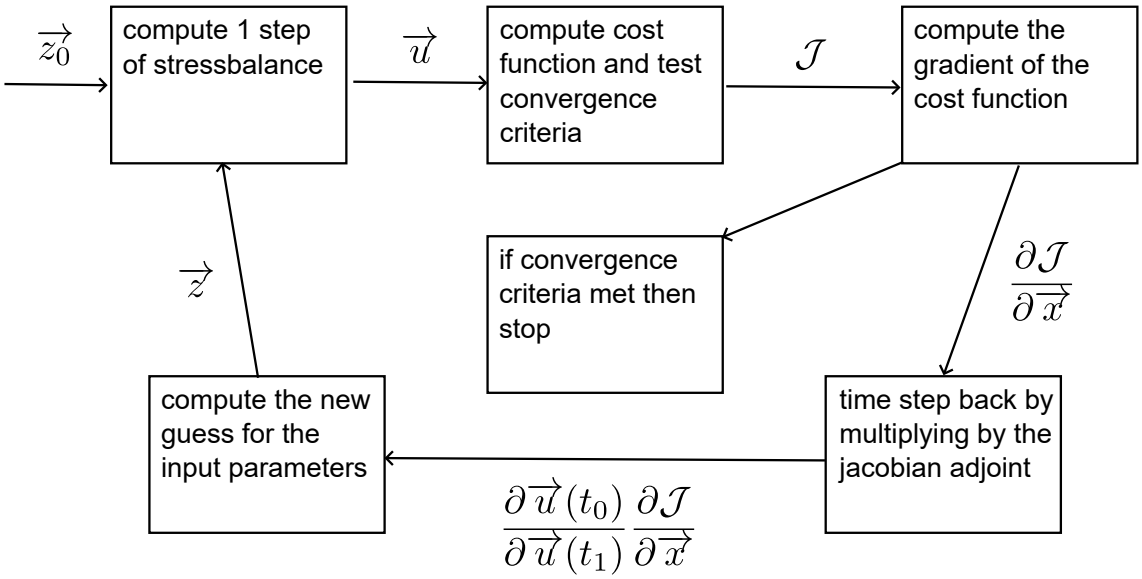

Figure 2.4: Inversion procedure adapted from (Nardi et al., 2009)

where κ is the variable being inverted for, which is the ice rigidity or the basal friction coefficient. The total cost function is given by Eq. (2.33),

$$\mathcal{J} = c_{\mathrm{a}}\mathcal{J}_{\mathrm{a}} + c_{\mathrm{l}}\mathcal{J}_{\mathrm{l}} + c_{\mathrm{t}}\mathcal{J}_{\mathrm{t}}, \tag{2.33}$$

where c_a, c_l, and c_t affect how much the total cost function depends on each component cost function.

$\mathcal{J}_a$ penalizes absolute differences between the observed and modeled ice surface speeds and ensures that the velocities match in fast flowing regions of the domain. $\mathcal{J}_l$ penalizes proportional differences between observed and modeled ice surface speeds and ensures that velocities match in the slow flowing regions of the domain. $\mathcal{J}_t$ penalizes gradients in the field being inverted for, which ensures that there is no overfitting. c_a and c_l are taken so that $c_a\mathcal{J}_a$ and $c_l\mathcal{J}_l$ are the same order of magnitude, which is the same order of magnitude as the ice speed in the fastest flowing regions of the domain. c_t is taken so that $c_t\mathcal{J}_t$ is an order of magnitude smaller than $c_a\mathcal{J}_a$ and $c_l\mathcal{J}_l$. c_t could be computed using an L-curve

analysis (Hansen, 2001), which ensures that the greatest amount of regularization of the field being inverted for is achieved with minimal loss of velocity match. However, with the variety of friction laws used and the method of choosing the final basal friction coefficient not accounting for regularization, an L-curve analysis is not performed here.

A series of five inversions are performed to determine the ice rigidity and basal shear stress. Starting with the Budd friction law (Eq. 1.19).

1. The ice rigidity over the floating ice shelf.
2. The Budd basal friction coefficient (α_b) over the grounded domain.
3. The ice rigidity over the floating ice shelf.
4. With the estimate of the basal shear stress from the inversion for the Budd basal friction coefficient, a switch to the hydrology-modified Schoof friction law is made and the basal friction coefficient is inverted for over the grounded part of the domain.
5. The ice rigidity over the entire domain.

The basal friction coefficient only needs to be determined over the grounded part of the domain as there is no friction underneath the floating ice shelf at the ice/ocean interface. The initial guess of the ice rigidity over the grounded part of the domain is determined using a temperature dependent relation from Cuffey and Paterson (2010) with ice temperature taken to be surface atmospheric temperature from RACMO2.3p2 (van Wessem et al., 2023).

Once the basal shear stress is determined and simulated ice speeds match closely (12.2 % error for this project) to those observed from MEaSUREs v2 (Rignot et al., 2011, 2017; Mouginot et al., 2012, 2017) a series of model relaxations are performed in order to have a steady state ice sheet geometry and subglacial hydrological system. The ice flow model is run for 20 years, forced with average surface mass balance from the years 1980 to 2010 of the CESM2 reanalysis model (Kittel et al., 2021). At the end of the ice flow relaxation the ice geometry and velocity is updated and a GlaDS relaxation is run for 40 years. At the end of the GlaDS relaxation the effective pressure is updated. The basal shear stress at the end of the ice flow relaxation and the effective pressure at the end of the GlaDS relaxation are then used to convert to the Schoof friction law, the Budd friction law, and the hydrology-modified Schoof friction law with different values of ζ. This ensures that the different friction laws being tested start with the same basal shear stress. For the Budd friction law the basal friction coefficient is given by Eq. (2.34),

$$\alpha_b = \sqrt{\frac{\tau_b}{N^r u_b^s}}, \tag{2.34}$$

s is taken to equal 1/3 and r is taken to equal 1. For the Schoof friction law the basal friction coefficient is given by Eq. (2.35) and for the hydrology-modified Schoof friction law the basal friction coefficient is given by Eq. (2.36).

$$C_s = \frac{\sqrt{\tau_b / u_b^m}}{\left(1 - \left(\tau_b / (C_{\max} N)\right)^{1/m}\right)^{m/2}}. \tag{2.35}$$

$$C = \sqrt{\frac{\tau_b}{u_b^m}} \left(1 + \left(\frac{\zeta}{N}\right)^{1/m} u_b\right)^{m/2}. \tag{2.36}$$

In areas where $\tau_b > C_{\max} N$ in the Schoof friction law, the value of $C_{\max}$ is raised so that $\tau_b = 0.999 C_{\max} N$.

After the model relaxations, the model is run for one year for both the ice flow-only and two-way coupled models to allow for a final relaxation. The model is then run forced with surface mass balance from the CESM2 SSP585 forcing scenario (Kittel et al., 2021) from 2010 to 2100 in all but two control runs, which keep the surface mass balance constant at the mean 1980-2010 value. A detailed description of all the simulations is given in Section 2.4.1.

The initialization procedure used in this study considers a comparison between multiple friction laws and having a relaxed state with simulated ice surface velocities, which match observed ice surface velocities. Though the initialization procedure is not the primary interest of this study, it is not unique and must be handled with care. An in depth investigation into coupled model initialization should be a focus of future work.

2.3 The coupled model

2.3.1 Coupling

Along with glacier geometry, GlaDS takes in ice flow information in the hydrology sheet opening rate in the form of the ice speed (Eq. 2.5). GlaDS also has the option to take in ice

flow information in the melt rate, which is either prescribed from the initMIP-Antarctica control run final time step (Seroussi et al., 2019) or given by Eq. (2.8), which is dependent on the basal shear stress and the ice speed. The hydrology sheet opening rate and the melt are therefore areas where GlaDS can be coupled to the ice flow model.

The ice flow model depends on subglacial hydrological information in the effective pressure dependent friction law and can take in subglacial hydrologic information when computing the driving stress as in Eq. (2.21), which depends on the hydrology sheet thickness. Therefore, the friction law and driving stress calculation are areas where the ice flow model can be coupled to GlaDS.

There are four two-way coupling methods which are tested.

1. The base coupling scheme involves taking the ice speed from the ice flow model and inputting it to the hydrology sheet opening rate in GlaDS, and taking the effective pressure from GlaDS and inputting it to the friction law in the ice flow model.

2. The second coupling scheme has all the components of the base coupling scheme but also uses the ice velocity and the basal shear stress from the ice flow model to compute the melt rate in GlaDS using Eq. (2.8).

3. The third coupling scheme has all the components of the base coupling scheme but also takes the hydrology sheet thickness from GlaDS to compute the driving stress in the SSA using Eq. (2.21).

4. The final coupling scheme uses all coupling components. The ice speed from the ice flow model is put into the hydrology sheet opening rate and the melt calculation (along with the basal shear stress) in GlaDS. The effective pressure from GlaDS is put into the the friction law, and the hydrology sheet thickness is put into the calculation of the driving stress in the ice flow model.

The coupling is envisioned in Fig. (2.5), where the base coupling scheme is represented by the green lines and the optional coupling components, which make up the other four schemes, are represented by the pink lines.

2.3.2 Model initialization

The coupled model initialization is very similar to the initialization of the ice flow model. With GlaDS run to steady state, the effective pressure is used to run the series of inversions

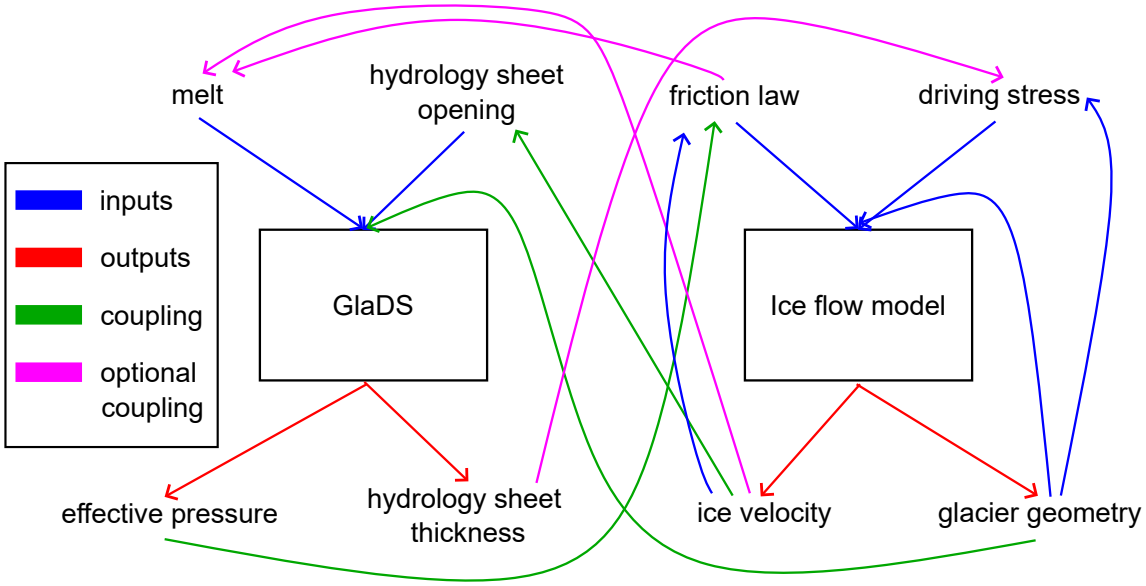

Figure 2.5: Schematic of the coupling between GlaDS and the ice flow model. Model inputs are represented by blue lines; model outputs are represented by red lines; green lines represent model outputs which are always fed as model inputs during coupling; pink lines represent model outputs which can be fed as model inputs during coupling.

described in Section 2.2.4. An ice flow and GlaDS relaxation is then performed (20 years ice flow, 40 years GlaDS) with effective pressure, ice sheet geometry, and ice speed being passed between the two models as described in Section 2.2.4. The basal shear stress from the ice flow relaxation is then used convert to the Schoof, Budd, or hydrology-modified Schoof friction laws if necessary as described in Section 2.2.4, and a final coupled relaxation is run for one year giving the initial conditions for the transient run. If melt is computed using Eq. (2.8) then after the series of inversions described in Section 2.2.4 and the ice flow relaxation, the GlaDS relaxation has the new form of melt input. If Eq. (2.21) is used to compute the driving stress in the coupled model, then the the one year coupled relaxation will use Eq. (2.21), with h_l determined from the second GlaDS relaxation.

2.4 Experiments

To test the relevance of various subglacial hydrology/ice flow feedback mechanisms, 16 model runs are performed with various setups so that results can be compared. The model runs which are performed are outlined in Section 2.4.1. The model domain and computational mesh that the models are run on is described in Section 2.4.2.

2.4.1 List of models run

To test the impact of coupling, runs of hydrology-only and ice flow-only models must be performed for comparison with coupled runs. GlaDS is run to steady state with melt input from the initMIP-Antarctica control run final time step (Seroussi et al., 2019), and a sheet conductivity of $10^{-3}\,\mathrm{m}^{7/4}\,\mathrm{kg}^{-1/2}$ and $5\cdot10^{-3}\,\mathrm{m}^{7/4}\,\mathrm{kg}^{-1/2}$. These runs will be denoted HM1K1, and HM1K2, "H" for hydrology-only, "M1" specifying that melt is implemented in GlaDS from the initMIP-Antarctica control run final time step (Seroussi et al., 2019), "K1" specifying a sheet conductivity of $10^{-3}\,\mathrm{m}^{7/4}\,\mathrm{kg}^{-1/2}$, and "K2" specifying a sheet conductivity of $5\cdot10^{-3}\,\mathrm{m}^{7/4}\,\mathrm{kg}^{-1/2}$. A summary of all the models run is given in Table 2.5. The output effective pressure from HM1K1 and HM1K2 are used to run the series of inversions described in Section 2.2.4 to determine the basal shear stress using the hydrology-modified Schoof friction law with $\zeta = 2\cdot10^{7}\,\mathrm{m}^{-4}\,\mathrm{kg\,s}$, and the ice speed. With initialization from HM1K1 and ice speed and basal shear stress from the corresponding inversions, GlaDS is run to steady state again using melt from Eq. (2.8). This run will be denoted HM2K1,"M2" specifying that melt is computed using Eq. (2.8). HM2K1 is used only as hydrology runs, as large water pooling under the Siple Coast ice streams with the relaxed ice sheet geometry means the lower sheet conductivity is not suitable for coupled modeling in this region of Antarctica.

The output effective pressure from the HM1K2 run is used to run the initialization procedure described in Sections 2.2.4 and 2.3.2. Ice flow-only runs for the Budd friction law, Schoof friction law, and hydrology-modified Schoof friction law with $\zeta = 2\cdot10^{7}\,\mathrm{m}^{-4}\,\mathrm{kg\,s}$ are then completed. These runs are denoted "IB", "IS1", and "IS2" respectively. "I" stands for ice flow-only, "B" specifies the Budd friction law, "S1" specifies the Schoof friction law, and "S2" specifies the hydrology-modified Schoof friction law. It is assumed that the sheet conductivity is taken to be $5\cdot10^{-3}\,\mathrm{m}^{7/4}\,\mathrm{kg}^{-1/2}$.

To test the impact of coupling compared to ice flow or hydrology models running alone, a base coupling run is performed. The same setup as in IS2 is used, except the model is

Model	Hydrology	Ice Flow	Friction Law	ζ	Melt	Driving Stress
HM1K1	yes	no	–	–	no	–
HM2K1	yes	no	–	–	yes	–
HM1K2	yes	no	–	–	no	–
IB	no	yes	Budd	–	–	no
IS1	no	yes	Schoof	–	–	no
IS2	no	yes	hydrology	2	–	no
IS2-control	no	yes	hydrology	2	–	no
C	yes	yes	hydrology	2	no	no
C-control	yes	yes	hydrology	2	no	no
CB	yes	yes	Budd	–	no	no
CS1	yes	yes	Schoof	–	no	no
CS2Z1	yes	yes	hydrology	1	no	no
CS2Z3	yes	yes	hydrology	3	no	no
CM	yes	yes	hydrology	2	yes	no
CD	yes	yes	hydrology	2	no	yes
FC	yes	yes	hydrology	2	yes	yes

Table 2.5: List of models run. The *Model* column gives the name of the model; the *Hydrology* column says if GlaDS is run; the *Ice Flow* column says if the ice flow model is run; the *Friction Law* column tells the friction law, which is *Schoof* for the Schoof friction law, *hydrology* for the hydrology-modified Schoof friction law, and *Budd* for the Budd friction law; The ζ column tells the value of ζ, which is in units of $10^7\,\mathrm{m}^{-4}\,\mathrm{kg\,s}$ if the hydrology-modified Schoof friction law is used; The *Melt* column says if melt is computed using Eq. (2.8); The *Driving Stress* column says if the the driving stress is computed using Eq. (2.21); In models where a field is not applicable – is used.

run with the coupling components of coupling scheme 1 described in Section 2.3.1. This model is denoted C, which stands for "coupled".

To test the impact of the friction law and the value of ζ on coupling, coupling is performed with the Budd, the Schoof, and hydrology-modified Schoof friction laws, with two extra values of ζ. For the Budd friction law the same setup as in "IB" is used, for the Schoof friction law, the same setup as in IS1 is used, except both models are run with the coupling components of coupling scheme 1 described in Section 2.3.1. These models are denoted CB, and CS1 respectively. The models CS2Z1 and CS2Z3 are run using the same setup as in C except switching to $\zeta = 10^7\,\mathrm{m}^{-4}\,\mathrm{kg\,s}$ and $\zeta = 3\cdot10^7\,\mathrm{m}^{-4}\,\mathrm{kg\,s}$ respectively after

the GlaDS relaxation. "Z1" and "Z3" denote the value of ζ used in the hydrology-modified Schoof friction law.

To test the impact of variable melt in the subglacial hydrologic system, coupling using melt from Eq. (2.8) is performed. The same setup as in C is used, except a switch to melt from Eq. (2.8) is made at the GlaDS relaxation. The model is denoted CM, where "M" specifies the use of melt from Eq. (2.8), and is the second coupling scheme described in Section 2.3.1.

To test the impact of subglacial lakes altering the glacier driving stress, coupling with Eq. (2.21) is performed. The same setup as in C is used, except a switch to using Eq. (2.21) for the SSA is made after the GlaDS relaxation. This run is denoted CD, where "D" specifies the use of Eq. (2.21) for the SSA, and is the third coupling scheme described in Section 2.3.1.

Finally, a coupled model with all coupling components is run. The same setup as C is used, except a switch to melt from Eq. (2.8) is made at the GlaDS relaxation and a switch to using Eq. (2.21) for the SSA is made after the GlaDS relaxation. This model with all the coupling components is denoted FC for "fully coupled", and is the fourth coupling scheme described in Section 2.3.1.

All the runs described above are run from 2010 to 2100 using surface mass balance forcing from the CESM2 SSP585 climate forcing scenario (Kittel et al., 2021). Additionally two control runs where surface mass balance is kept at the average 1980-2010 level are run, one using the same setup as C and the other using the same setup as IS2, these runs are denoted C-control and IS2-control respectively.

A summary for the motivation for running each model given in Table 2.6. Each simulation takes approximately four hours to run using 32 CPUs on the parallelized Graham cluster.

2.4.2 Model domain and computational mesh

The model domain is comprised of the Ross Sea subglacial hydrologic catchment and the Ross Ice Shelf. Areas where ice thickness from Morlighem et al. (2020) is less than 100 m and areas near this thin ice that create numerical instabilities in GlaDS have been carefully masked out of the domain (it is assumed that there is no ice). GlaDS runs over the grounded portion of the domain, which is defined by flotation criterion $\rho_i g H + \rho_w g B > 0$, where ρ_w is the density of sea water; the ice flow model runs over the entire domain.

Model	**Reasoning**
HM1K1	hydrology base run
HM2K1	affect of melt water calculation on hydrology
HM1K2	affect of sheet conductivity on hydrology
IB	affect of friction law on ice flow
IS1	affect of friction law on ice flow
IS2	ice flow base run
IS2-control	affect of surface mass balance forcing on ice flow
C	coupled base run
C-control	affect of surface mass balance forcing on coupled runs
CB	affect of friction law on coupling
CS1	affect of friction law on coupling
CS2Z1	affect of ζ on coupling
CS2Z3	affect of ζ on coupling
CM	affect of variable melt on coupling
CD	affect of driving stress calculation on coupling
FC	affect of full coupling

Table 2.6: List of models run with the motivation behind each run. The *Model* column gives the name of the model and the *Reasoning* column gives the motivation for running the model.

The computational mesh is refined in areas where there are deep troughs, mountains, and fast flowing ice. The average element edge length is 20 km on the eastern half of the domain, 7.5 km on the western half of the domain where the Siple Coast is, 10 km in the floating ice shelf, 5 km around Lake Vostok, and 2 km near mountains, deep troughs, and grounded regions where ice flow exceeds $100\,\mathrm{m\,a^{-1}}$. Element edge lengths get as small as 225 m, which occurs near the domain boundary in the Lake Vostok region.

The model domain, including the areas where no ice is assumed, and the grounding line are shown in Fig. 2.6 along with bed topography, ice thickness, and mesh resolution.

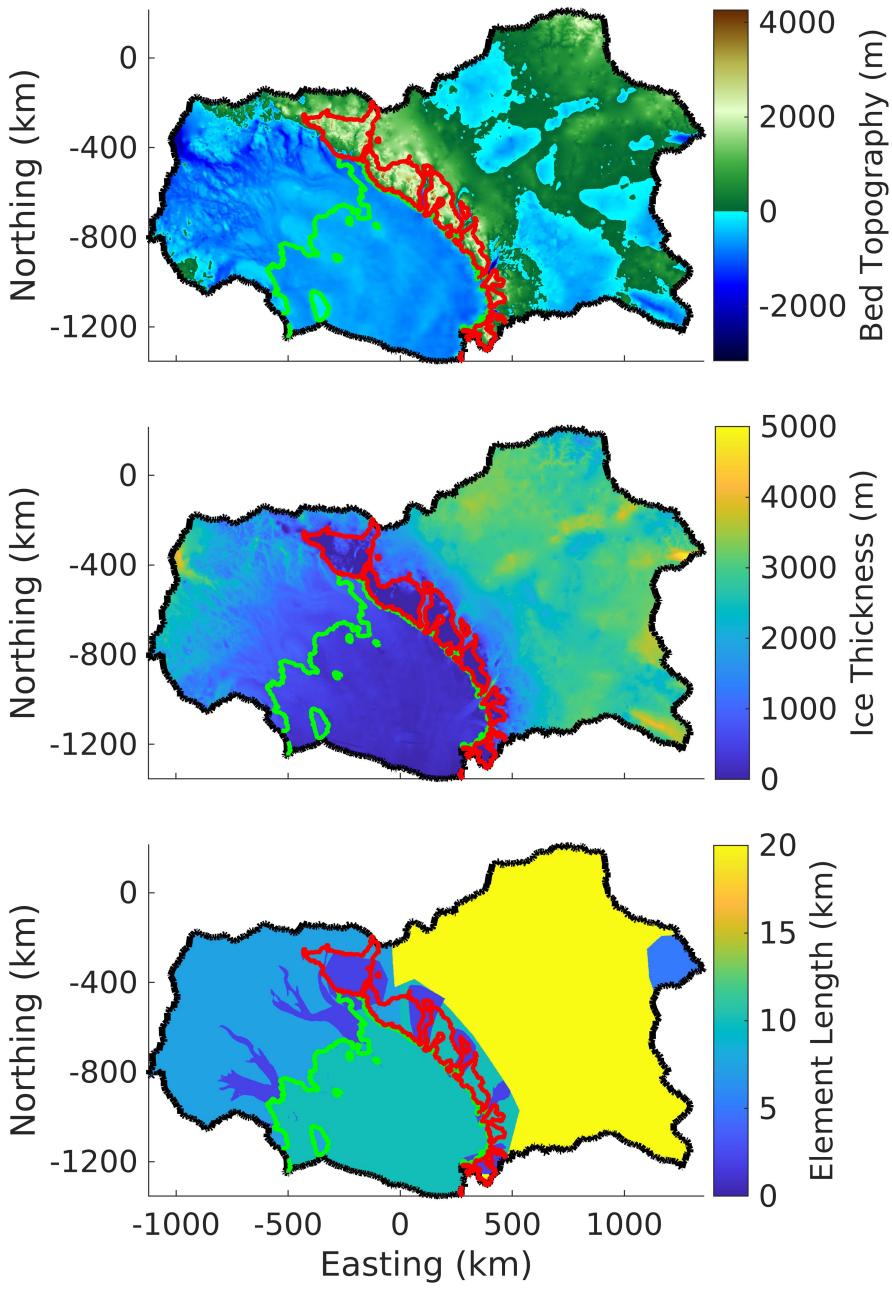

Figure 2.6: Bed topography, ice thickness, and mesh resolution, with model domain boundary and grounding line. (a) bed topography (m); (b) ice thickness (m); (c) typical element edge length (km). The black lines represents the domain boundary, red lines represent areas which have been masked out of the domain due to thin ice and model instabilities, green lines represent grounding lines.

Chapter 3

Results

Here we present the results of the model runs described in Section 2.4.1. Section 3.1 contains the hydrology-only model runs (HM1K1, HM1K2, and HM2K1), discussing spatial trends in flotation fraction, hydrology sheet thickness, and channelization, as well as temporal trends in subglacial lake evolution. Section 3.2 contains the results of the ice flow-only model runs (IS2, IS1, IB, and IS2-control), and will discuss general trends in ice speed and ice sheet geometry over the transient simulation, as well as the impact of friction law and surface mass balance forcing on these trends. Section 3.3 contains the results of the coupled models (C, C-control, CS1, CB, CS2Z1, CS2Z3, CD, CM, and FC). It begins with a comparison between the results of C and the results of IS2 and C-control, moves to the results of the coupling schemes with different friction laws/friction law parameters (CS1, CB, CS2Z1, and CS2Z3), and ends with the results from the optional coupling component runs (CD, CM, and FC).

3.1 Hydrology

When GlaDS has been previously run in the Antarctic a sheet conductivity of $10^{-4}\,\mathrm{m}^{7/4}\,\mathrm{kg}^{-1/2}$ has typically been used (Dow et al., 2018, 2020, 2022; McArthur et al., 2023). However, due to the unrealistically large areas where subglacial lakes form with a sheet conductivity of $10^{-4}\,\mathrm{m}^{7/4}\,\mathrm{kg}^{-1/2}$ in the Siple Coast, we elect to raise the sheet conductivity to $10^{-3}\,\mathrm{m}^{7/4}\,\mathrm{kg}^{-1/2}$ for a hydrology-only run and to $5\cdot10^{-3}\,\mathrm{m}^{7/4}\,\mathrm{kg}^{-1/2}$ for coupled runs, which tend to have unrealistically large areas where subglacial lakes form with a sheet conductivity of $10^{-3}\,\mathrm{m}^{7/4}\,\mathrm{kg}^{-1/2}$. The hydrology-only run with a sheet conductivity of $10^{-3}\,\mathrm{m}^{7/4}\,\mathrm{kg}^{-1/2}$

best follows our understanding of Antaractic subglacial hydrology in the context of subglacial water pressure, and is the closest to the typical value of $10^{-4}\,\mathrm{m}^{7/4}\,\mathrm{kg}^{-1/2}$ (Dow et al., 2020, 2022), it is therefore presented here as HM1K1. It is worth noting that past studies that used a sheet conductivity of $10^{-4}\,\mathrm{m}^{7/4}\,\mathrm{kg}^{-1/2}$ were conducted in a version of GlaDS implemented in MATLAB (Dow et al., 2020, 2022), while this study uses GlaDS implemented in ISSM, which may explain why a higher sheet conductivity works better in our models.

With HM1K1, much of the Ross Sea subglacial hydrologic catchment (92.1 %) has a fraction of flotation ($p_w/p_i = 1 - N/p_i$) greater than 0.8 (Fig. 3.1a). These values are elevated within the Siple Coast ice streams and the Byrd trough where the fraction of flotation is often above 0.95 (31.0 % of the total grounded domain), and sometimes reaches flotation in regions where there are subglacial lakes (0.755 % of the total grounded domain). Between the Siple Coast ice streams lie isolated patches of high effective pressure (low fraction of flotation), which correspond to ice rises where the glacier bed and the ice surface lie hundreds of meters above the surrounding topography, creating hydraulic potential highs. The fraction of flotation surrounding the Transantarctic Mountains (TM) is generally low except in the troughs which feed water into the ocean. East of the TM the fraction of flotation is generally high as water is pressurized underneath thick ice in the interior of East Antarctica.

Notable subglacial hydrological features occur in the fast flowing regions of the domain. Channels form underneath the ice streams of the Siple Coast, including under the stagnated Kamb ice stream, and the outlet glaciers running through the TM (Fig. 3.1b). Though the channels running through the TM have a directed discharge path, such a path is less evident in the Siple Coast ice streams where channels form on many element edges as a result of low effective pressure and channel closing rates, and because the relatively flat ice surface creates small gradients in hydraulic potential. Subglacial lakes form underneath the Siple Coast ice streams, not including the Kamb ice stream, and in the Byrd trough (Fig. 3.1c). The hydrology sheet thickness reaches close to the typical bedrock bump height (8 cm) underneath the ice streams of the Siple Coast and in the Byrd trough (Fig. 3.1d). A smaller hydrology sheet exists outside of these fast flowing regions, quickly falling to zero near the TM and the Siple Coast ice rises where the subglacial hydrological system appears to be inactive.

The subglacial lakes of the Siple Coast first form higher up in the ice streams away from the grounding line, and drain through a system of linked subglacial lakes where they eventually reach steady state at the end of the model run (Fig. 3.2). Though these lakes reach thicknesses of up to 50 m earlier in the model run (Fig. 3.3), this could be a consequence of a still developing hydrological system, and the lake thickness near the end

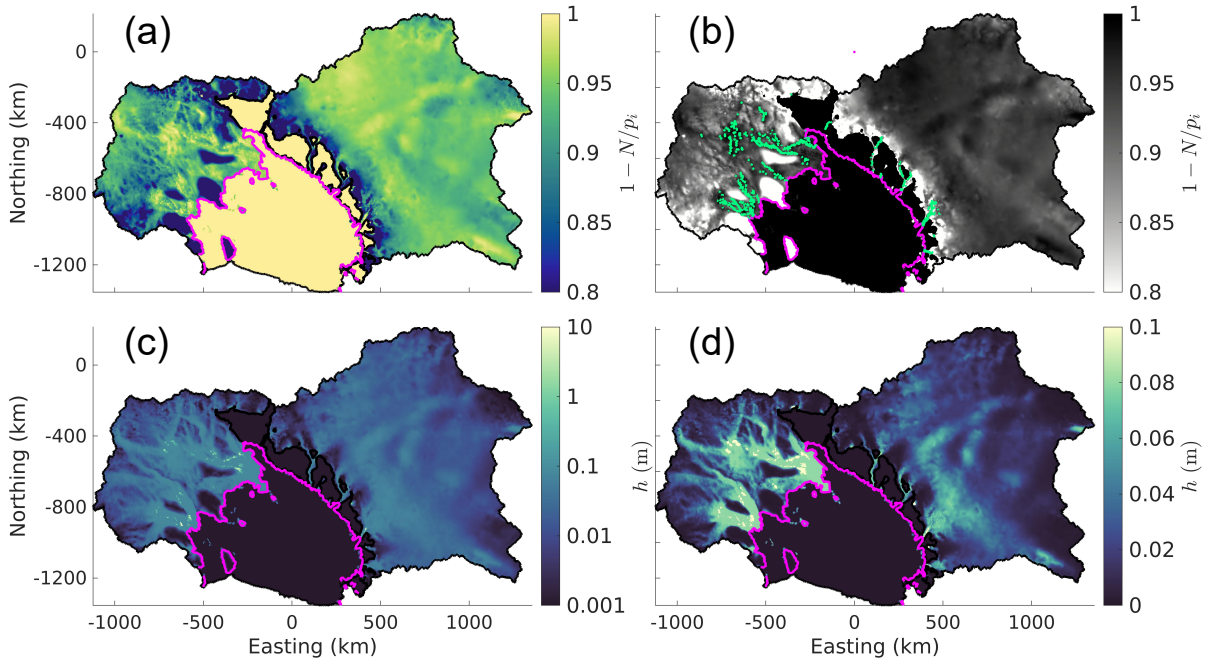

Figure 3.1: Results from HM1K1. (a) shows the fraction of flotation $1 - N/p_i$; (b) shows the fraction of flotation overlayed with channels which discharge $1\,\mathrm{m}^3\,\mathrm{s}^{-1}$ or more; (c) and (d) show the hydrology sheet thickness at different scales. Black lines represent the model boundary, and pink lines represent the grounding line.

of the model run, which is substantially smaller (less than 15 m) should be taken as typical modeled lake depth in these areas. Though some of the modeled lakes agree with locations of subglacial lakes inventoried by Livingstone et al. (2022), there are many subglacial lakes in Livingstone et al. (2022) that do not appear in HM1K1 and many modeled lakes that are not recorded by Livingstone et al. (2022).

Fig. (3.3) shows the hydrology sheet thickness for the four lakes seen in the southern end of the main trunk of Ice Stream B in Fig. (3.2i,ii,iii,iv). The first three lakes follow a similar pattern of a fast fill period followed by a plateau in hydrology sheet thickness and a gradual drainage towards a steady state value much lower than the plateau. The fourth lake fills and drains slower than the other three, with peak sheet thickness approximately 20 m below that of the next shallowest lake (Fig. 3.3, lake 2). The lakes fill in the order of their position in the ice stream (upglacier lakes filling first) and the plateau and drainage period last longer in the lakes further down the ice stream. Despite the spatial organization

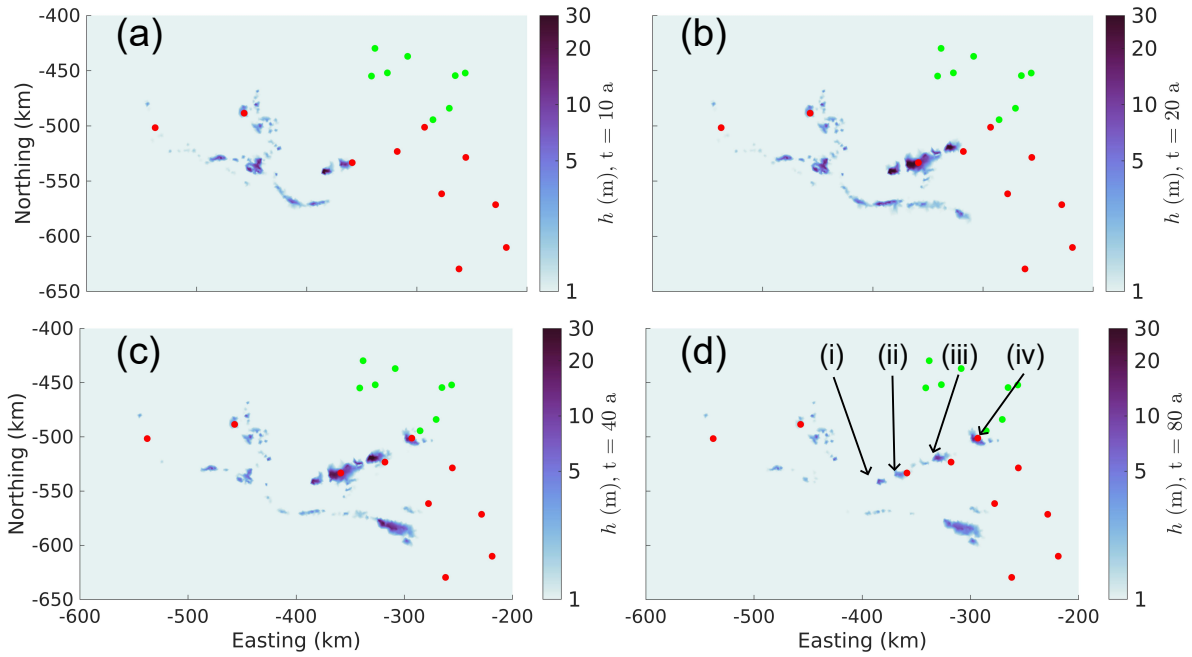

Figure 3.2: Hydrology sheet thickness (m) from HM1K1 for various points in time underneath ice stream A. (a) shows h at $t = 10$ a; (b) shows h at $t = 20$ a; (c) shows h at $t = 40$ a; (d) shows h at $t = 80$ a. (i) is lake 1 in Fig. (3.3); (ii) is lake 2 in Fig. (3.3); (iii) is lake 3 in Fig. (3.3); (iv) is lake 4 in Fig. (3.3). Red dots are active subglacial lakes from Livingstone et al. (2022) and green dots are stable subglacial lakes from Livingstone et al. (2022)

of the lakes, the filling of lakes further downstream does not seem to be dependent on the drainage of the lakes upstream. Lakes 2 and 3 both fill while lake 1 is at its plateau. Lake 4 fills just as lake 1 begins to drain, without a delay time for water to make its way through the system from lake 1 to lake 4.

3.1.1 Sheet conductivity

The raised sheet conductivity in HM1K2 ($5{\cdot}10^{-3}\,\mathrm{m}^{7/4}\,\mathrm{kg}^{-1/2}$) allows water to drain through the distributed sheet system much faster than in HM1K1, raising the effective pressure (Fig. 3.4a) and lowering the hydrology sheet thickness (Fig. 3.4c) and lake depth (Fig. 3.4d). Indeed, the average flotation fraction in HM1K2 is 0.858, compared to 0.912 in HM1K1. Likewise, 82.0 % of the domain has a fraction of flotation above 0.8 in HM1K2 compared

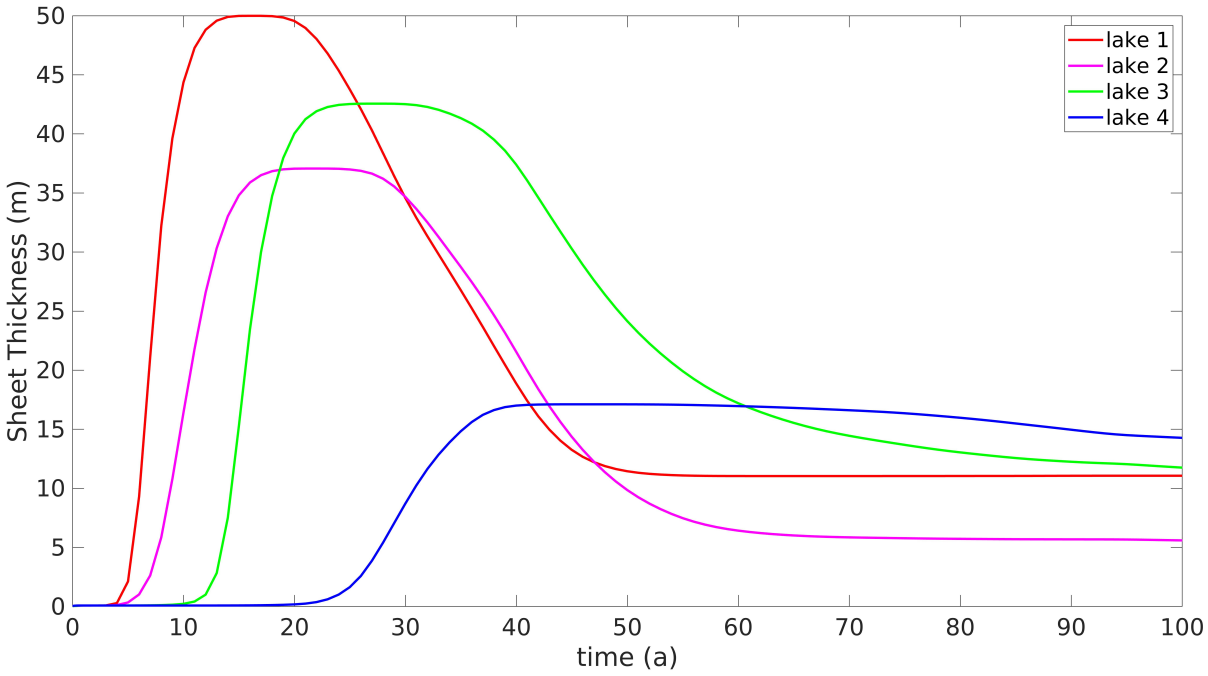

Figure 3.3: Hydrology sheet thickness (m) as a function of time for the four lakes in the southern end of the main trunk of Ice Stream B.

to 92.1 % in HM1K1. Similarly, but to a more extreme extent, 3.9 % of the domain has a fraction of flotation above 0.95 in HM1K2 compared to 31.2 % in HM1K1. The effective pressure discrepancy between HM1K1 and HM1K2 is more pronounced in the northern end of the Siple Coast where ice streams D and E lie, and surrounding the TM. Though the flotation fraction is still reduced in the eastern half of the domain, the reduction is generally smaller with an average difference in flotation fraction of -0.071 in the West compared to -0.048 in the East.

The increased effective pressure in HM1K2 means that the channel closing rate is generally larger and channels have a more difficult time forming in HM1K2 than in HM1K1 (Fig. 3.4b). Channels still form underneath Ice Stream B, the parts of Ice Stream E closer to the grounding line, and in the Byrd trough. However, channels no longer form in Ice Stream D, the Kamb Ice Stream, and other outlet glaciers running through the TM as in HM1K1.

The hydrology sheet thickness is close to the typical bedrock bump height in the Siple Coast ice streams in both HM1K1 and HM1K2 (Fig. 3.4c,d). However, the hydrology sheet

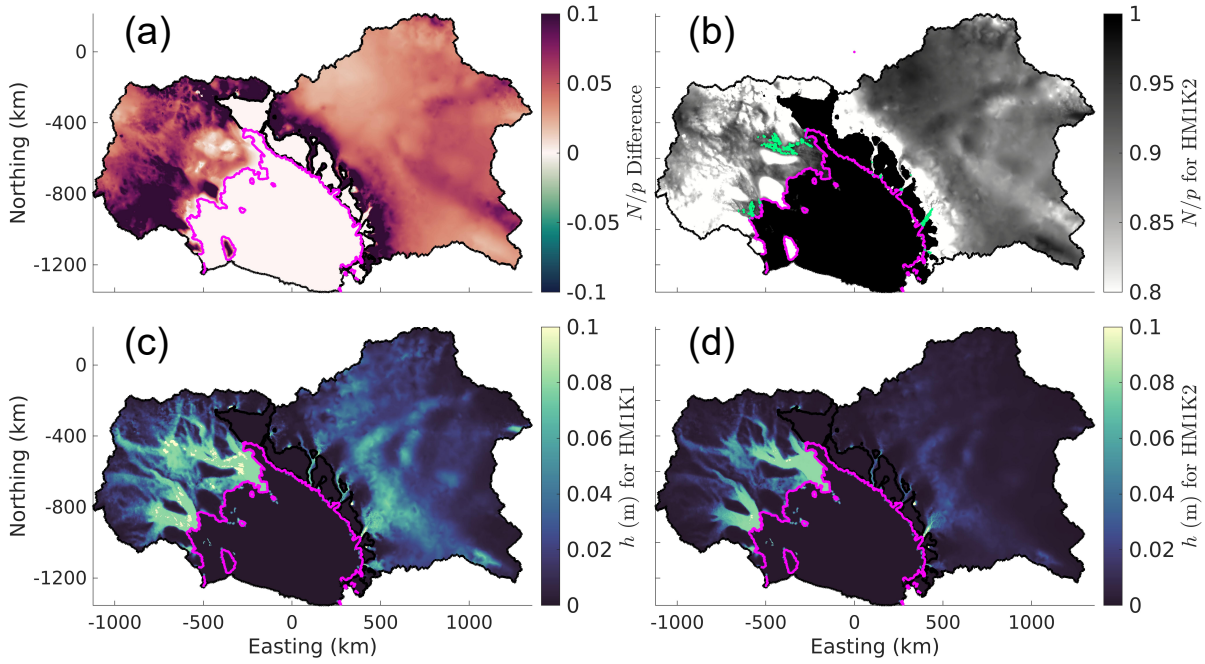

Figure 3.4: Sheet conductivity comparison. (a) shows the difference between N/p_i for HM1K2 and HM1K1; (b) shows the fraction of flotation for HM1K2 overlayed with channels which discharge $1\,\mathrm{m}^3\,\mathrm{s}^{-1}$ or more; (c) shows the hydrology sheet thickness for HM1K1 (m); (d) shows the hydrology sheet thickness for HM1K2 (m). Black lines represent the model boundary, and pink lines represent the grounding line.

thickness quickly falls off in the interior of the West Antarctic Ice Sheet outside the ice streams. Similarly, in the eastern half of the domain the hydrology sheet thickness quickly falls off outside of the Byrd trough in HM1K2. Subglacial lakes still form in a few locations in the Siple Coast ice streams in HM1K2, but not as many form as in HM1K1 and the ones that do form are not as deep as in HM1K1. No subglacial lakes form upglacier of the Siple Coast ice streams in HM1K2, whereas a few lakes formed upglacier of Ice Stream B in HM1K1. The lakes of HM1K2 also do not have a fill drain pattern as in HM1K1, rather they fill to a steady state depth by the end of the model run.

3.1.2 Melt input

In comparison to HM1K1, HM2K1 has generally lower effective pressure (Fig. 3.5a,b), generally higher hydrology sheet thickness, and more subglacial lakes (Fig. 3.5c,d). Though these trends are observed over the entire domain, they are more prominent in the eastern half of the domain, with a higher fraction of flotation of on average 0.025 in the East and 0.016 in the West. Subglacial lakes form in the interior of the East Antarctic Ice Sheet in HM2K1, which does not happen in HM1K1. These discrepancies in model outputs can be understood through the melt input to the two models. Both models identify the same areas of high melt, however, the contribution of geothermal heat flux to the melt of HM2K1 adds water to the subglacial system in areas where there is very little water in HM1K1 (Fig. 3.5e,f). The Siple Coast is characterised by high melt areas allowing for more similar subglacial hydrological outputs between the two models. However, the eastern portion of the domain is characterized by limited melt except surrounding the Byrd trough, meaning that much of the interior of the East Antarctic Ice Sheet has a more pressurized subglacial hydrological system with more water in HM2K1.

3.2 Ice flow

We present here the results of the ice flow-only models (IS2, IS1, IB, and IS2-control), including the trends of ice speed in the major ice streams of the Siple Coast, and the Byrd Glacier.

All ice flow models follow the same general patterns over the 90 year simulation (Fig. 3.6). Ice streams A, B, D, E, and the upper eastern branch of ice stream B slow down, while the upper western branch of ice stream B tends to maintain speed or speed up. The ice of ice streams A, B, D, and E thinned over the simulation, while the ice in the Kamb ice stream thickened. The ice upglacier of the TM and in the troughs running through the TM thickened in excess of 40 m. Notably in this area, the ice upglacier of the Byrd trough thickened in excess of 50 m and ice sped up by more than $100\,\mathrm{m\,a^{-1}}$ downstream of the grounding line (Fig. 3.7).

Ice stream A behaves similarly in all four ice flow models (Fig 3.8a). Starting with an ice speed of approximately $125\,\mathrm{m\,a^{-1}}$ ($126.0\,\mathrm{m\,a^{-1}}$ for IS2 and IS2-control, $122.9\,\mathrm{m\,a^{-1}}$ for IS1, and $125.5\,\mathrm{m\,a^{-1}}$ for IB) the ice stream slows down by approximately $30\,\mathrm{m\,a^{-1}}$ over the 90 year run ($31.3\,\mathrm{m\,a^{-1}}$ for IS2, $32.9\,\mathrm{m\,a^{-1}}$ for IS1, $31.4\,\mathrm{m\,a^{-1}}$ for IB, and $27.9\,\mathrm{m\,a^{-1}}$ for IS2-control). The models agree on the slowdown within $1\,\mathrm{m\,a^{-1}}$ for the first 49 years of the

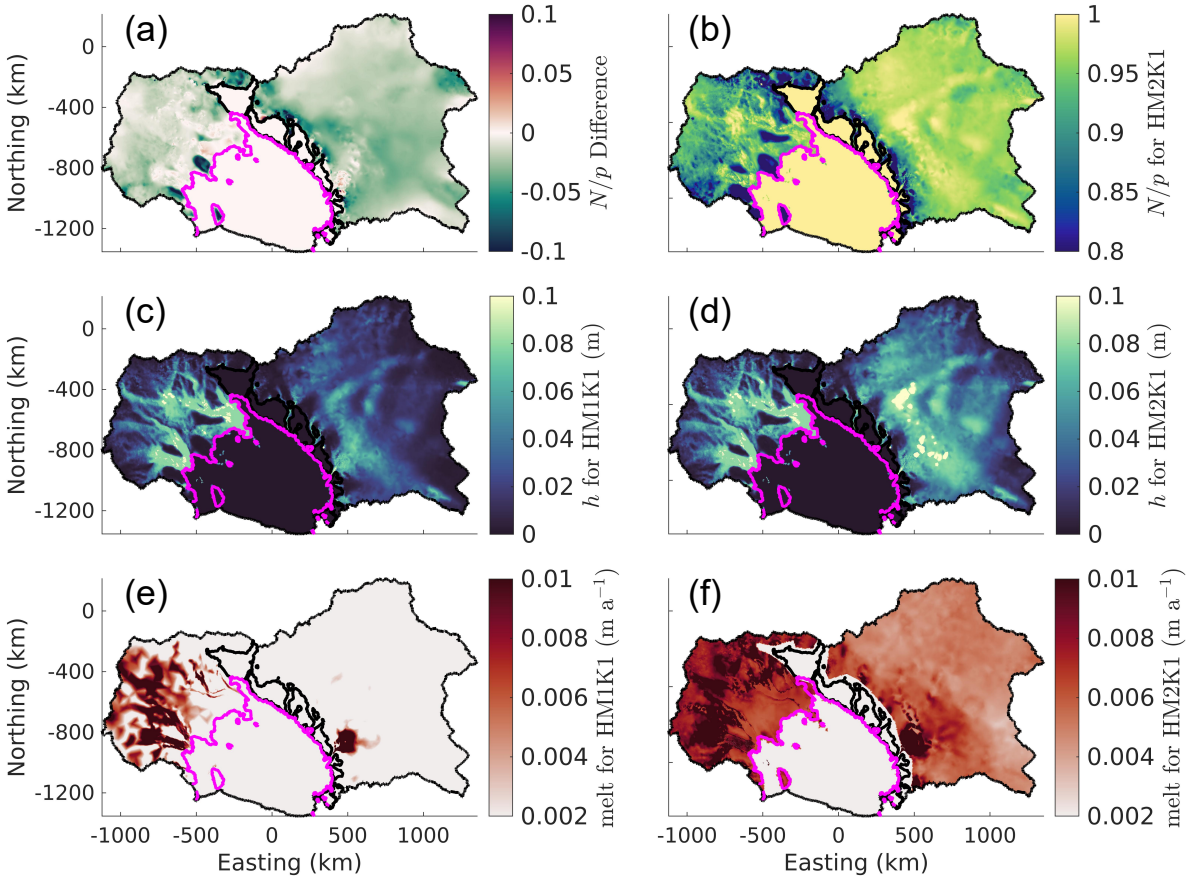

Figure 3.5: Melt input comparison. (a) shows the difference between N/p_i for HM2K1 and HM1K1; (b) shows the fraction of flotation for HM2K1; (c) shows the hydrology sheet thickness for HM1K1 (m); (d) shows the hydrology sheet thickness for HM2K1 (m); (e) shows the melt input for HM1K1; and (f) shows the melt input for HM2K1. Black lines represent the model boundary, and pink lines represent the grounding line.

simulation, after which IS2-control decreases in its rate of slowdown and diverges from the other models.

The main trunk of ice stream B slowed over the model runs (Fig 3.8b), though not to the same extent as Ice Stream A. The Eastern tributary feeding the main trunk of Ice Stream B follows this pattern in ice speed change, however, the Western tributary maintains ice speed to within $6\,\mathrm{m\,a^{-1}}$ for the first 30 years of the model run where it then plateaus and speeds up, surpassing its starting speed in IS2 and IB. Starting at approximately

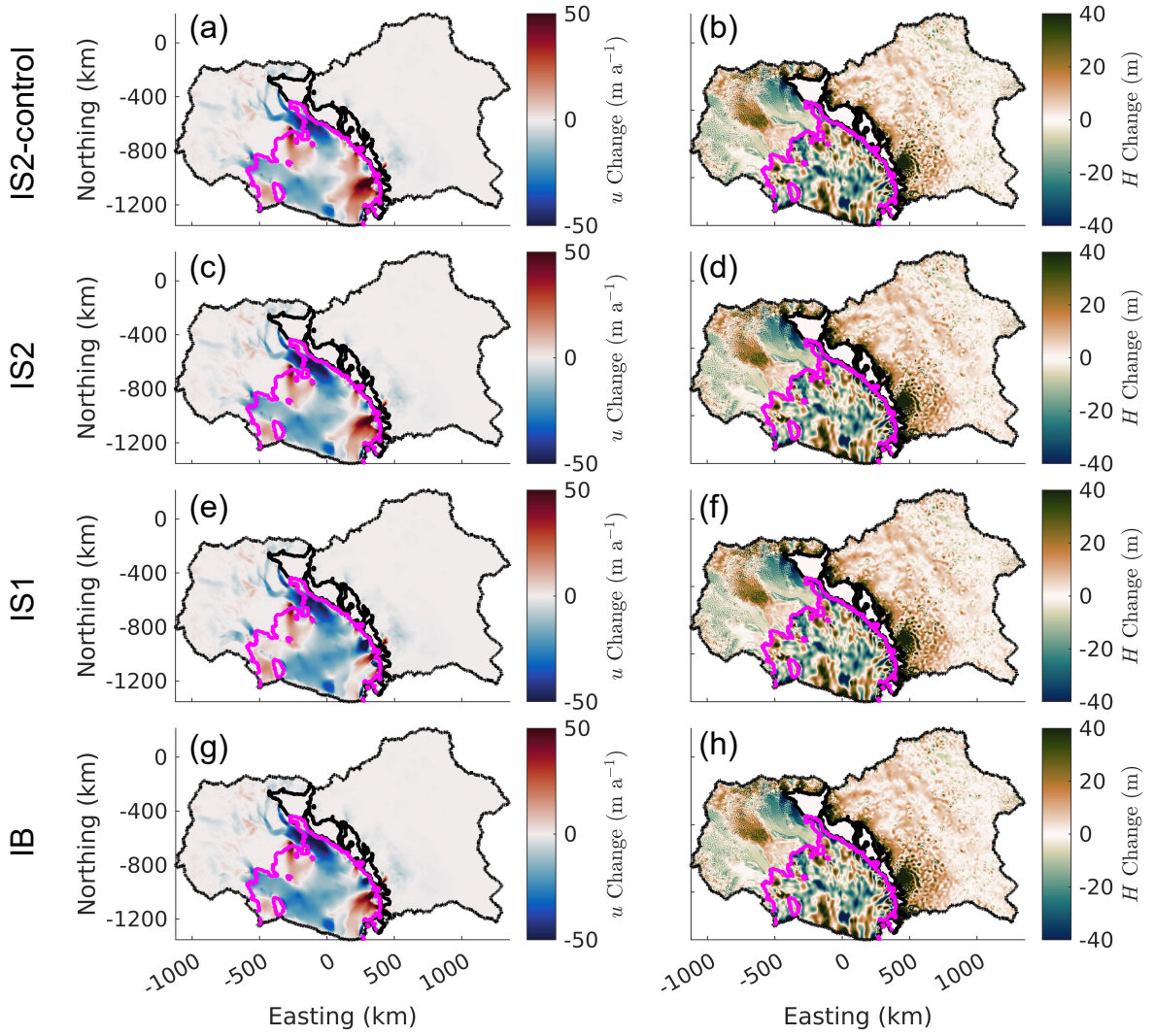

Figure 3.6: Change in ice speed (u) and ice thickness (H) from 2010 to 2100 (2100 values minus 2010 values) for IS2-control, IS2, IS1, and IB. (a) change in ice speed for IS2-control (m a^{-1}); (b) change in ice thickness for IS2-control (m); (c) change in ice speed for IS2 (m a^{-1}); (d) change in ice thickness for IS2 (m); (e) change in ice speed for IS1 (m a^{-1}); (f) change in ice thickness for IS1 (m); (g) change in ice speed for IB (m a^{-1}); (h) change in ice thickness for IB (m). Black lines are the domain boundary and pink lines are the grounding lines.

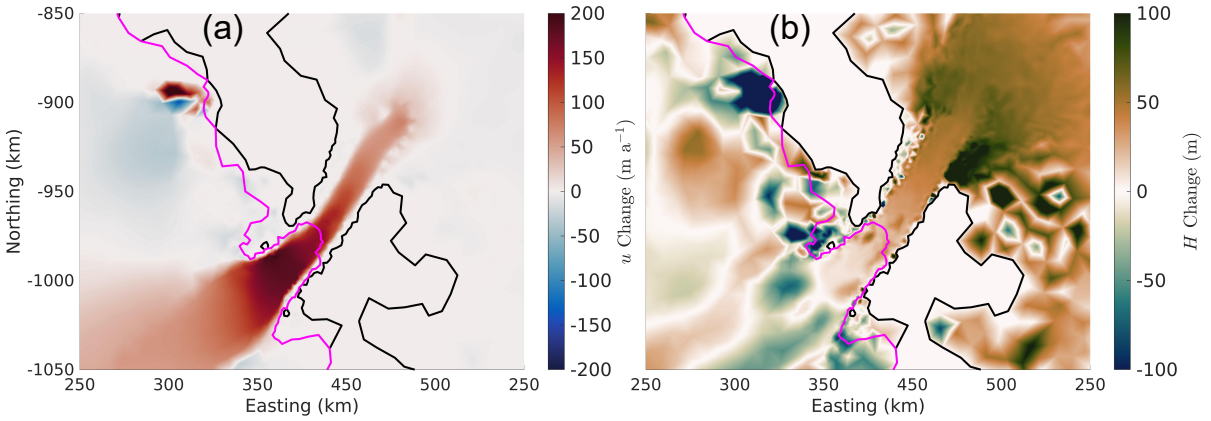

Figure 3.7: Change in ice speed (u) and ice thickness (H) between 2100 and 2010 for IS2, zoomed in on Byrd Glacier. (a) change in ice speed (m a^{-1}); (b) change in ice thickness (m). Black lines are the domain boundary and pink lines are the initial grounding line.

410 m a^{-1} (413.7 m a^{-1} for IS2 and IS2-control, 409.8 m a^{-1} for IS1, and 412.8 m a^{-1} for IB) the main trunk of Ice Stream B slows by at least 15.3 m a^{-1} up until 2082 (15.3 m a^{-1} for IS2, 18.1 m a^{-1} for IS1, 16.0 m a^{-1} for IB, and 16.6 m a^{-1} for IS2-control) in all ice flow runs. In the remaining 18 years of the simulation the ice stream speeds up by 3.8 m a^{-1} in IS2 and IB, and by 3.3 m a^{-1} in IS1. The ice in IS2-control continues to slow after 2082, finishing the simulation 20.2 m a^{-1} below its starting value.

Ice stream D shows similar trends of ice speed in IS2, IB, and IS2-control throughout the model run (Fig 3.8c). Ice Stream D decreased in ice speed by 5.9 m a^{-1}, 5.6 m a^{-1}, and 6.4 m a^{-1} starting from 294.9 m a^{-1}, 294.4 m a^{-1}, and 294.9 m a^{-1} in IS2, IB, and IS2-control respectively. In IS1 the ice stream gradually slows as with IS2, IB, and IS2-control but the rate of slow down is faster, so the ice stream ends up slowing down by 9.0 m a^{-1} from 293.6 m a^{-1} over the course of the 90 year simulation, with the most significant slow-down occurring at the start of the simulation before relaxing and slowing down at a rate comparable to the other ice flow models after 2030.

Unlike the other Siple Coast ice streams, Ice Stream E shows no discernible pattern between the different ice flow simulations (Fig 3.8d). In the IS2, IS2-control, and IS1 simulations the ice stream slows by 3.4 m a^{-1}, 4.9 m a^{-1}, and 8.3 m a^{-1} respectively from its initial value of 273.9 m a^{-1} for IS2 and IS2-control, and 276.0 m a^{-1} for IS1. In the IB run the ice stream increased in speed by 1.6 m a^{-1} up to 2045 and then slowed down by 2.0 m a^{-1} up to year 2090 where it reversed trend again ending up 0.1 m a^{-1} slower than

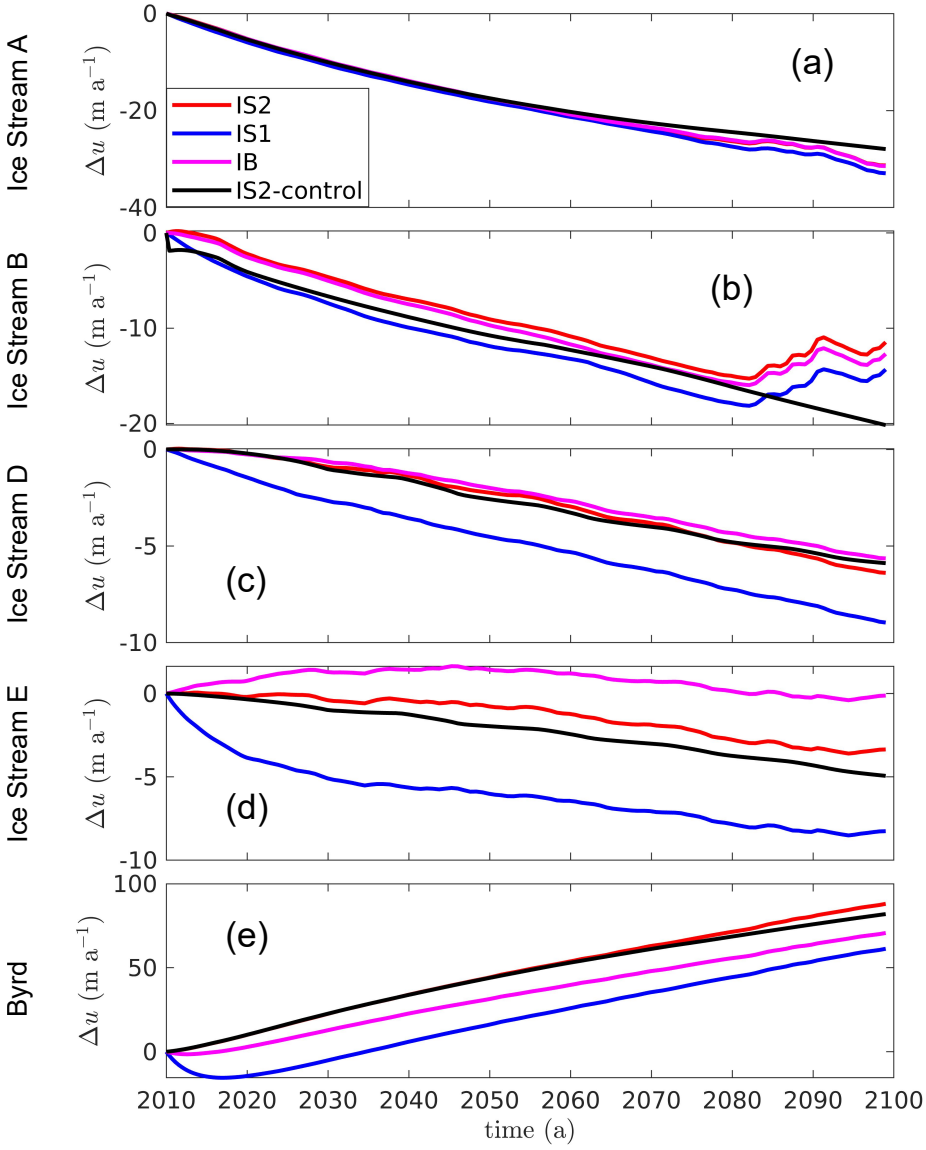

Figure 3.8: Change in areally-averaged ice speed (u) for the Siple Coast ice streams and Byrd Glacier. (a) Change in ice speed in ice stream A (m a^{-1}); (b) Change in ice speed in ice stream B (m a^{-1}); (c) Change in ice speed in ice stream D (m a^{-1}); (d) Change in ice speed in ice stream E (m a^{-1}); (e) Change in ice speed in Byrd Glacier (m a^{-1}).

its initial speed of $268.0\,\mathrm{m\,a^{-1}}$.

The Byrd Glacier sped up by $88.1\,\mathrm{m\,a^{-1}}$ and $82.0\,\mathrm{m\,a^{-1}}$ from it's starting value of $433.5\,\mathrm{m\,a^{-1}}$ in IS2 and IS2-control respectively over the course of the 90 year simulation (Fig 3.8e). In IS1 (IB), Byrd Glacier slowed down to $15.5\,\mathrm{m\,a^{-1}}$ ($1.5\,\mathrm{m\,a^{-1}}$) below its starting value of $475.1\,\mathrm{m\,a^{-1}}$ ($438.6\,\mathrm{m\,a^{-1}}$) over the first 7 (2.5) years of the simulation, after which it sped up by $76.8\,\mathrm{m\,a^{-1}}$ ($72.2\,\mathrm{m\,a^{-1}}$) over the remainder of the simulation.

Looking at the patterns in ice flow from Fig. (3.8), a few trends between the various ice flow models can be identified. IS1 tends to have ice streams which slow down initially before reaching a trend similar to the other ice flow models, this is true in ice streams B, D, E, and in the Byrd Glacier. Variation from the long term trend in ice streams A and B manifests around 2080 in all ice flow models except IS2-control. This suggests that the ice dynamics of ice streams A and B is governed by internal mechanisms up until 2080 where the surface mass balance forcing becomes relevant.

The one year ice flow relaxation after the switch to the various friction laws described in Section 2.2.4 allows for varying initial conditions between IS2, IS1, and IB (IS2 and IS2-control have the same initialization). The ice sheet geometry is very similar across all ice flow models (within 0.15 m throughout the entire domain), but the ice velocity changes by more than $100\,\mathrm{m\,a^{-1}}$ in a few areas near the model boundary. The IS1 model has slower ice speed than IS2 in the Siple Coast ice streams close to the grounding line and faster ice speed in ice streams B and E further upglacier (Fig. 3.9a). Byrd glacier is faster in IS1 than in IS2. Given the initially faster ice streams of IS1, which have an initial slowdown compared to the other ice flow models in the first 10 years of the simulation, it is likely that the one year relaxation was insufficient to allow IS1 to relax. The IB model starts with slower ice speed than IS2 in all the ice streams of the Siple Coast and the Byrd Glacier (Fig. 3.9b). The slower ice speed propagates upglacier in the Siple Coast ice streams into the interior of the West Antarctic Ice Sheet.

3.3 Coupling

Here we present the results of the coupled models, including the coupled models with different friction law parameters and different friction laws in Section 3.3.1, coupling with melt from Eq. (2.8) in Section 3.3.2, coupling with the inclusion of h_l in the glacier driving stress in Section 3.3.3, and the model with all the coupling components in Section 3.3.4.

At the end of run C, ice streams D and E sped up from their 2010 values (Fig 3.10a). The main trunk of Ice Stream B and its western tributary also sped up over this time, but

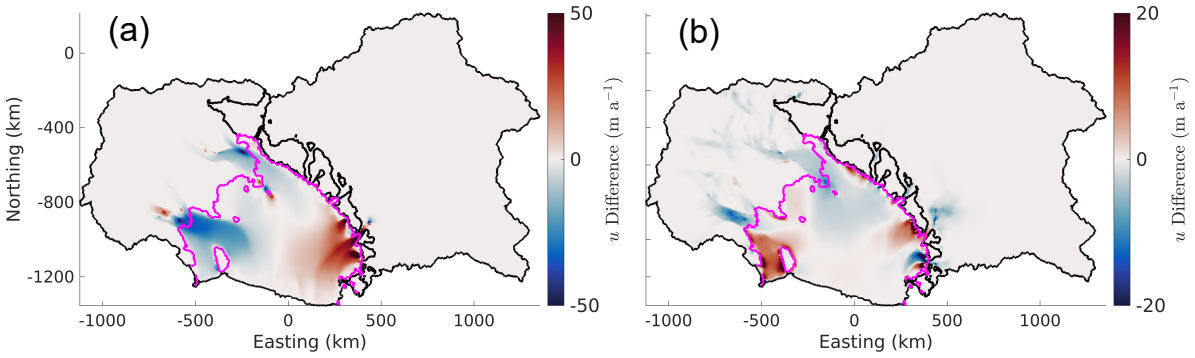

Figure 3.9: Comparison between initial ice speeds (u) for the ice flow models with different friction laws. (a) difference in initial ice speed between IS1 and IS2 (m a^{-1}); (b) difference in initial ice speed between IB and IS2 (m a^{-1}). Black lines are the domain boundary and pink lines are the initial grounding line. Note the subplots have different colour bar scales.

Ice Stream A and the eastern tributary of ice stream B slowed (Fig 3.10a). In comparison to IS2, the ice streams of the Siple Coast are all faster in C, with the exception of Ice Stream A (Fig 3.10b). Byrd Glacier has a similar speed in both C and IS2. The generally faster ice in C can be attributed to the changes in the hydrologic system, which occurred over the 90 year model run. The effective pressure decreased during this time from a mean fraction of flotation of 0.890 in 2010 to 0.936 in 2100, the percent of the domain above a fraction of flotation of 0.8 increased from 85.7 % to 89.8 % and the percent of the domain above a fraction of flotation of 0.95 increased from 6.3 % to 12.3 %. Most of this change happened in the western part of the domain (the Siple Coast) where the mean fraction of flotation elevated from 0.873 to 0.960 compared to a change from 0.899 to 0.924 in the Eastern part of the domain. As a result, ice flow patterns are very similar in both IS2 and C in the eastern part of the domain (Fig 3.10b). Near the end of the C run, the hydrology sheet blew up underneath Ice Stream B and its tributaries stretching into the interior of the West Antarctic Ice Sheet. The area where the hydrology sheet was above the typical bedrock bump height increased from 0.02 % to 1.11 %. This large pooling of water may be attributed to thinning of ice in this region discussed in Section 3.2.

The behaviour of C-control is very similar to that of C in the ice streams of the Siple Coast and the Byrd Glacier. This suggests that in the coupled models, surface mass balance forcing is a less important factor than it is in the ice flow-only models. A comparison between the behaviour of the Siple Coast ice streams and Byrd Glacier in C and IS2 is presented below.

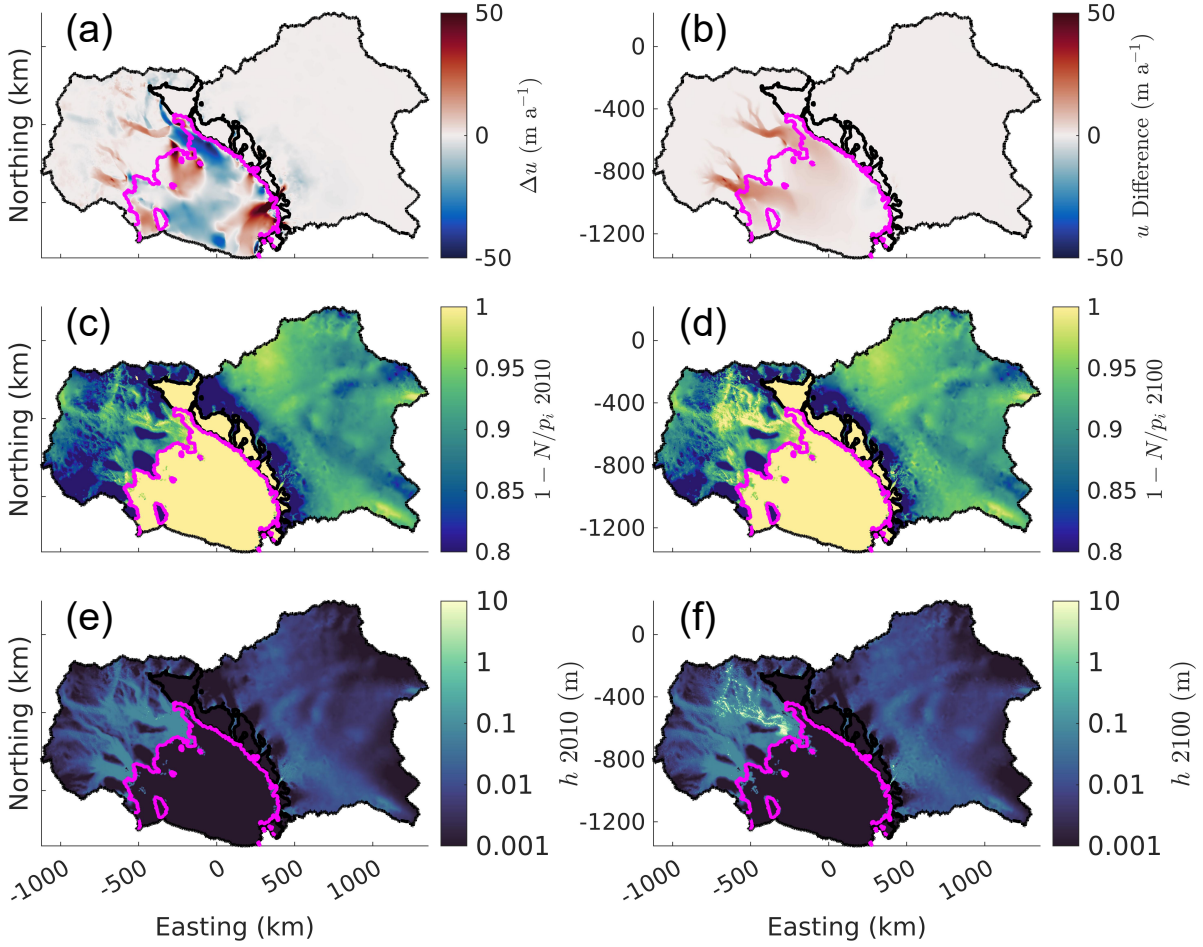

Figure 3.10: Spatial changes in effective pressure, hydrology sheet thickness and ice speed for C, and ice speed comparison with IS2. (a) Change in ice speed from 2010-2100 in C (m a^{-1}); (b) Difference in ice speed at 2100 between C and IS2 (m a^{-1}); (c) fraction of flotation at 2010 in C; (d) fraction of flotation at 2100 in C; (e) hydrology sheet thickness at 2010 in C (m); (f) hydrology sheet thickness at 2100 in C (m). Black lines are the domain boundary and pink lines are the initial grounding line.

Ice Stream A and Byrd Glacier behave very similarly in both IS2 and C, with a difference in ice speed of 2.3 m a^{-1} and 0.5 m a^{-1} respectively at 2100. However, the dynamics of ice streams B, D, and E are impacted significantly by the coupling. In C, Ice Stream B slows down initially, followed by a speedup, just as in IS2. However, in C, Ice Stream B slows

by only $6.6\,\mathrm{m\,a^{-1}}$ as compared to $15.3\,\mathrm{m\,a^{-1}}$ for IS2, and C reverses this trend by 2070, as compared to 2082 in IS2. The increase in ice speed in C over the remaining 31 years of the simulation is more pronounced than the increase in ice speed in IS2 ($12.2\,\mathrm{m\,a^{-1}}$ for C compared to $3.8\,\mathrm{m\,a^{-1}}$ for IS2). In C, the effective pressure used to compute the basal shear stress decreased from $0.0534p_i$ to $0.0332p_i$ over the course of the simulation resulting in an increase of ξ from 1.08 to 4.12 as the ice stream gradually transitioned more into an Iken sliding regime.

Compared to Ice Stream B, Ice Stream D has a much more variable ice speed trend, with fluctuations of more than $10\,\mathrm{m\,a^{-1}}$ over a couple years, which is larger than the change over the entire run in IS2 ($6.4\,\mathrm{m\,a^{-1}}$). This trend in ice speed follows closely to the inverse trend in effective pressure, which fluctuates between $0.09p_i$ and $0.03p_i$ (the effective pressure cap). Given that the mean ξ is often lower in Ice Stream D than in Ice Stream B (0.591 compared to 2.06), the close match between the negative of the effective pressure trend and the ice speed trend suggests that the part of Ice Stream D which is in a strong Iken sliding regime controls the ice dynamics of much of the ice stream. The high variability in effective pressure, which drives the ice speed profile of Ice Stream D is not captured in IS2. Ice Stream E behaves in a similar manner as Ice Stream D (variable ice speed, effective pressure, and ξ) and a discussion of its dynamics is not included.

For both ice streams B and D the effective pressure has a high negative correlation to the sliding regime (-0.996 for Ice Stream B and -0.995 for Ice Stream D). This is to be expected as ξ has a cubic dependence on the effective pressure compared to a linear dependence on the ice speed, and typical changes in effective pressure are comparatively larger than changes in ice speed for fast moving ice such as that in an ice stream, that is to say that $\Delta N/N > \Delta u/u$. Because of this, IS2 produced little variability in ξ compared to C, where changes in ξ were dominated by the effective pressure trend.

The lakes of C display varying behaviour depending on which ice stream they are under. Like the lakes in the hydrology-only model runs, the lakes under Ice Stream B have one occurrence of a fill drain cycle. As in HM1K1, the fill period is faster than the drain period, though both the filling and draining of the lake take place on timescales much faster than in HM1K1. This is likely due to the higher sheet conductivity in C, which allows water to make its way through the subglacial hydrological system faster than in HM1K1. Unlike in HM1K1, in C the lakes under Ice Stream B fill and drain simultaneously as a result of trends in the hydraulic potential taking place on spatial scales that span many typical lake widths. In C, the lakes in ice stream D display much more variable behaviour than the lakes in Ice Stream B, with variability in lake depth of approximately 1 m a year (Fig. 3.12). This variability in lake depth is a consequence of a variable hydraulic potential field under Ice Stream D. The variability of the lake under Ice Stream D and the simultaneous fill/drain

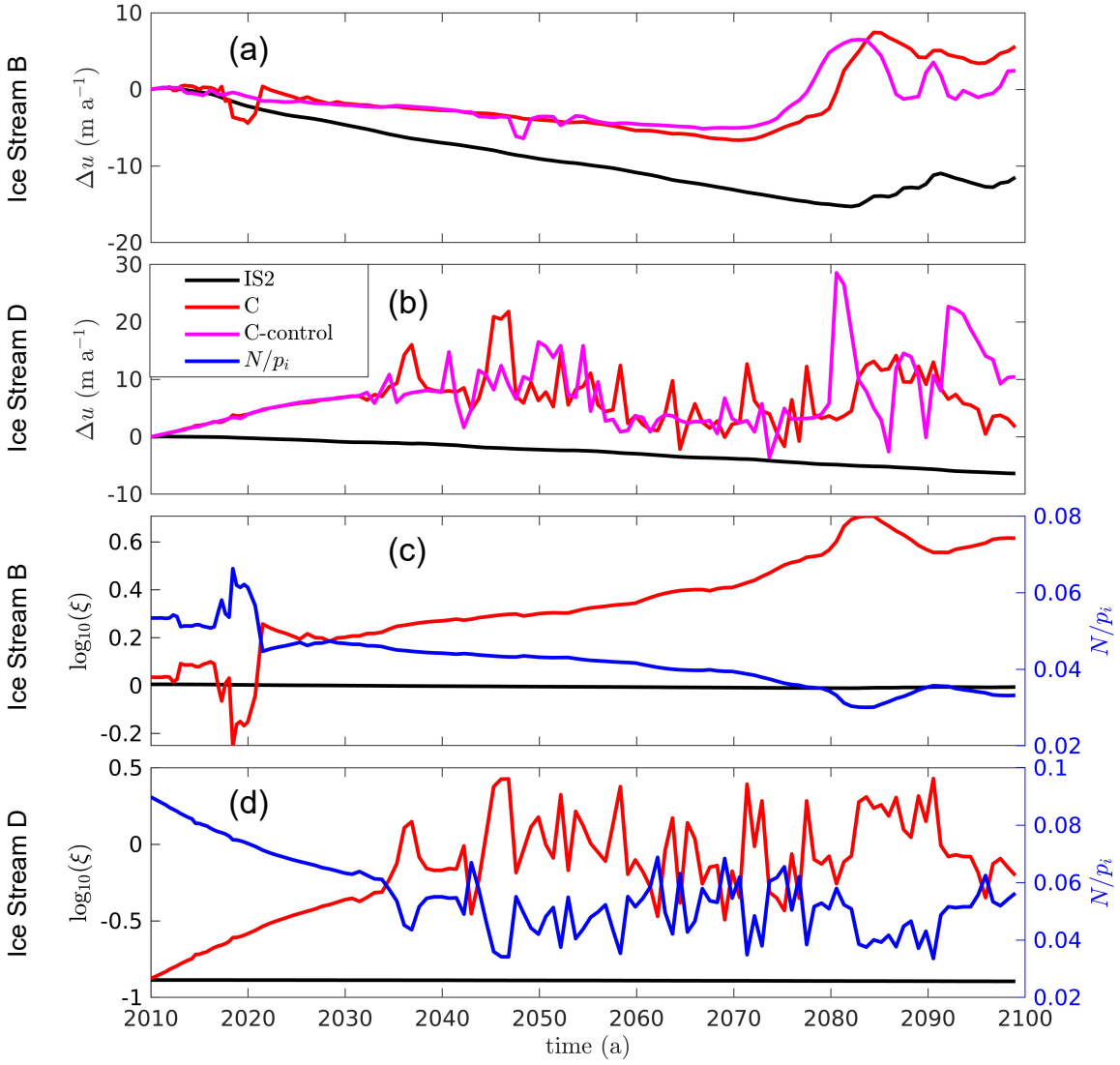

Figure 3.11: Comparison between the dynamics of ice streams B and D in the IS2 and C simulations. (a) change in ice speed in the main trunk of Ice Stream B (m a^{-1}); (b) change in ice speed in Ice Stream D (m a^{-1}); sliding regime (ξ) as a function of time and change in N/p_i for C in Ice Stream B; sliding regime (ξ) as a function of time and change in N/p_i for C in Ice Stream D.

patterns of the lakes in Ice Stream B highlights the importance of the hydraulic potential field in GlaDS lake dynamics.

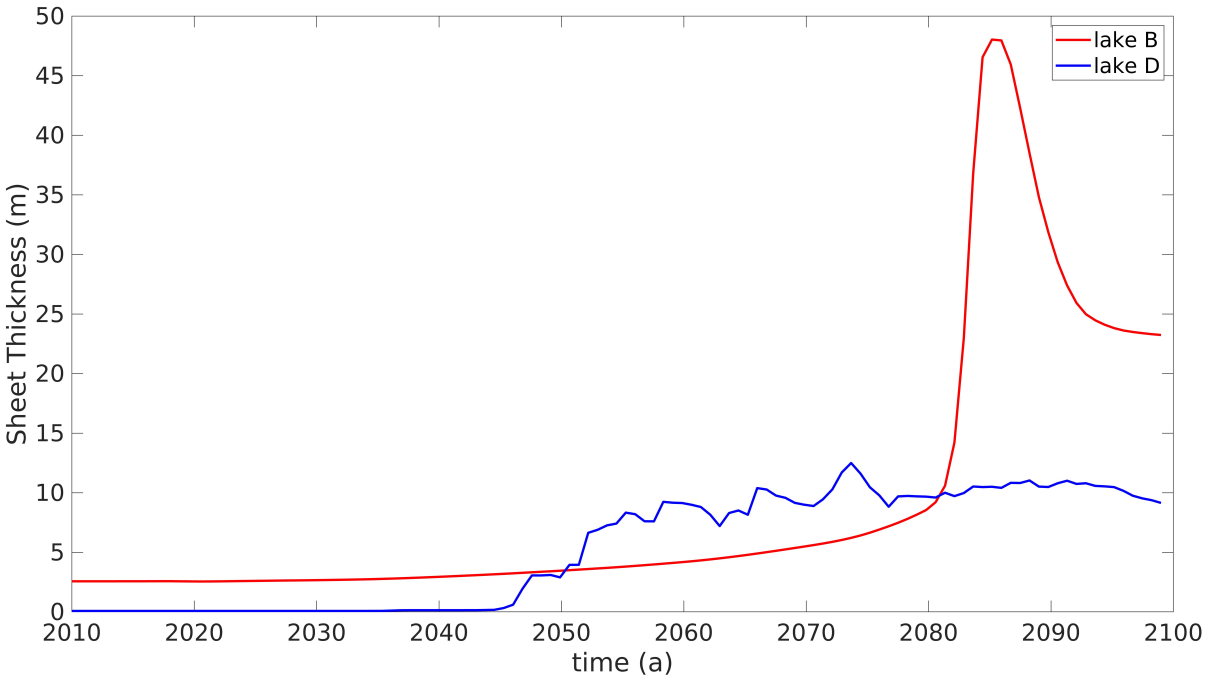

Figure 3.12: Lake depth in C (m) for a lake underneath Ice Stream B and a lake underneath Ice Stream D.

3.3.1 Friction law

All of the Siple Coast ice streams have a similar relationship between the ice speed in C and the ice speed in CS1. The Siple Coast ice streams in C are consistently faster than the ice streams in CS1 with more exaggerated long term trends, which mirror the long term trends of CS1. As in C, the effective pressure is the dominant factor controlling ice stream speed in CS1. However, the ice streams in CS1 have a consistently smaller ξ than those in C. In CS1, ξ starts off as $3.31 \cdot 10^{-10}$, $6.55 \cdot 10^{-10}$, $7.62 \cdot 10^{-10}$, and $3.12 \cdot 10^{-9}$ in ice streams A, B, D, and E respectively. Not only is this many orders of magnitude smaller than the values in C (0.0269, 1.08, 0.133, 0.0447 in ice streams A, B, D, and E respectively), but it is smaller than the sliding regime in the ice surrounding the ice streams as well. Given that the basal shear stress has negligible dependence on effective pressure in a strong Weertman

sliding regime such as those of the Siple Coast ice streams of CS1, it is unexpected that the ice stream dynamics of the Siple Coast ice streams of CS1 correlate so strongly with the effective pressure trend (-0.358 correlation coefficient). However, this can be explained by ice/hydrology interactions at the onset of the ice streams. At the onset of the ice streams, the sliding regime in CS1 is much closer to Iken even at the start of the model run ($\xi > 10^{-4}$, Fig. 3.14e). As the effective pressure decreases and ξ increases throughout the model run (Fig. 3.14g), the effective pressure plays a larger role in lowering the basal shear stress and speeding up ice. The ice speedup propagates down the ice stream, producing the trends in Fig. (3.13). C has a higher ξ to begin with in this region meaning that changes in effective pressure have a more pronounced impact on ice motion, which explains the larger variability in ice speed associated with the Siple Coast ice streams of C.

Unlike the Siple Coast ice streams, the Byrd Glacier has larger ice speed variability in CS1 than in C, and has higher ice speed in most of the last 30 years of the simulation with a spike in ice speed at 2072 of $671.5\,\mathrm{m\,a^{-1}}$ ($159.9\,\mathrm{m\,a^{-1}}$ above the 2070 value). This can be explained by the discrepancy in sliding regime of Byrd Glacier. In C, the side walls of the Byrd trough are in a Weertman sliding regime as high basal friction is required in the model to make up for lateral friction, which the model does not take into account (Fig. 3.14b,d). The interior of Byrd Glacier is in more of an Iken sliding regime than the side walls, as the trough is a hydraulic potential low. In CS1, the change to the Schoof friction law resulted in the Byrd Glacier interior being in a Weertman sliding regime with the sidewalls being in more of an Iken sliding regime (Fig. 3.14f,h). It was even necessary in these regions to raise the value of $C_{\max}$ to match the initial basal shear stress of C. Because of the high friction and the still underestimated value of $C_{\max}$, changes in effective pressure at the Byrd Glacier side walls, which increase the sliding regime over the course of the simulation have the ability to greatly influence the Byrd Glacier ice speed in CS1 while having little impact in C, which is what we see in Fig. (3.13e).

In the CB simulation, all the ice streams of the Siple Coast, and Byrd Glacier showed a significant speedup of up to $500\,\mathrm{m\,a^{-1}}$ in some regions by the end of the model run (Fig. 3.15a). In the case of the Siple Coast, the speedup propagated far inland, draining ice from the interior of the West Antarctic Ice Sheet. Because the ice upglacier of the Siple Coast ice streams moved initially much slower than the ice streams themselves, the speedup of the ice sheet interior was large comparatively to the speedup of the ice streams. That is to say that $\Delta u/u$ was larger in the ice sheet interior. Because of this, the ice streams of the Siple Coast thickened by in some cases 50 m over the course of the simulation, despite increasing in ice speed by hundreds of meters per year (Fig. 3.15b).

The inland propagation of ice speedup in the Siple Coast can be attributed to the linear dependence of the basal shear stress on the effective pressure. As effective pressure lowers

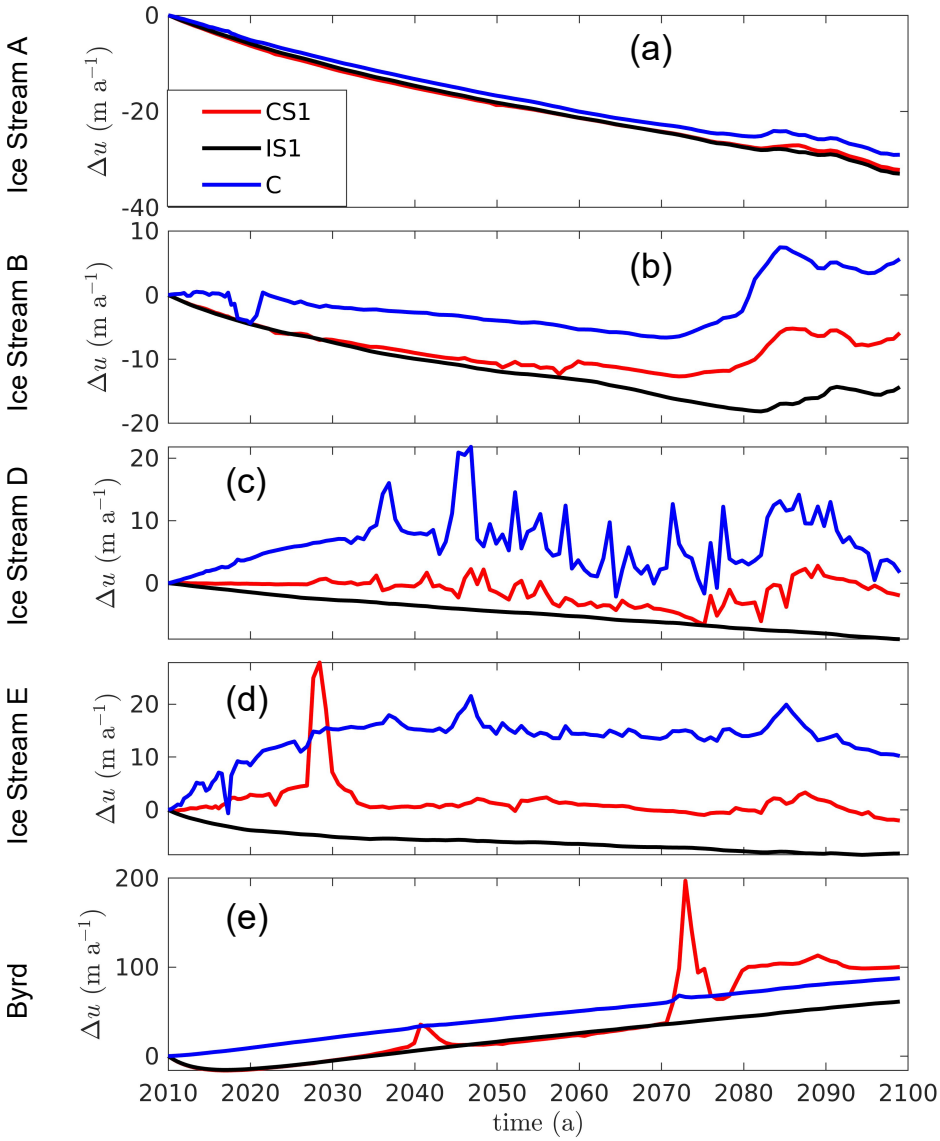

Figure 3.13: Comparison between the dynamics of the Siple Coast ice streams and Byrd Glacier for CS1, IS1, and C. (a) change in Ice Stream A ice speed (m a^{-1}); (b) change in Ice Stream B ice speed (m a^{-1}); (c) change in Ice Stream D ice speed (m a^{-1}); (d) change in Ice Stream E ice speed (m a^{-1}); (e) change in Byrd Glacier ice speed (m a^{-1}).

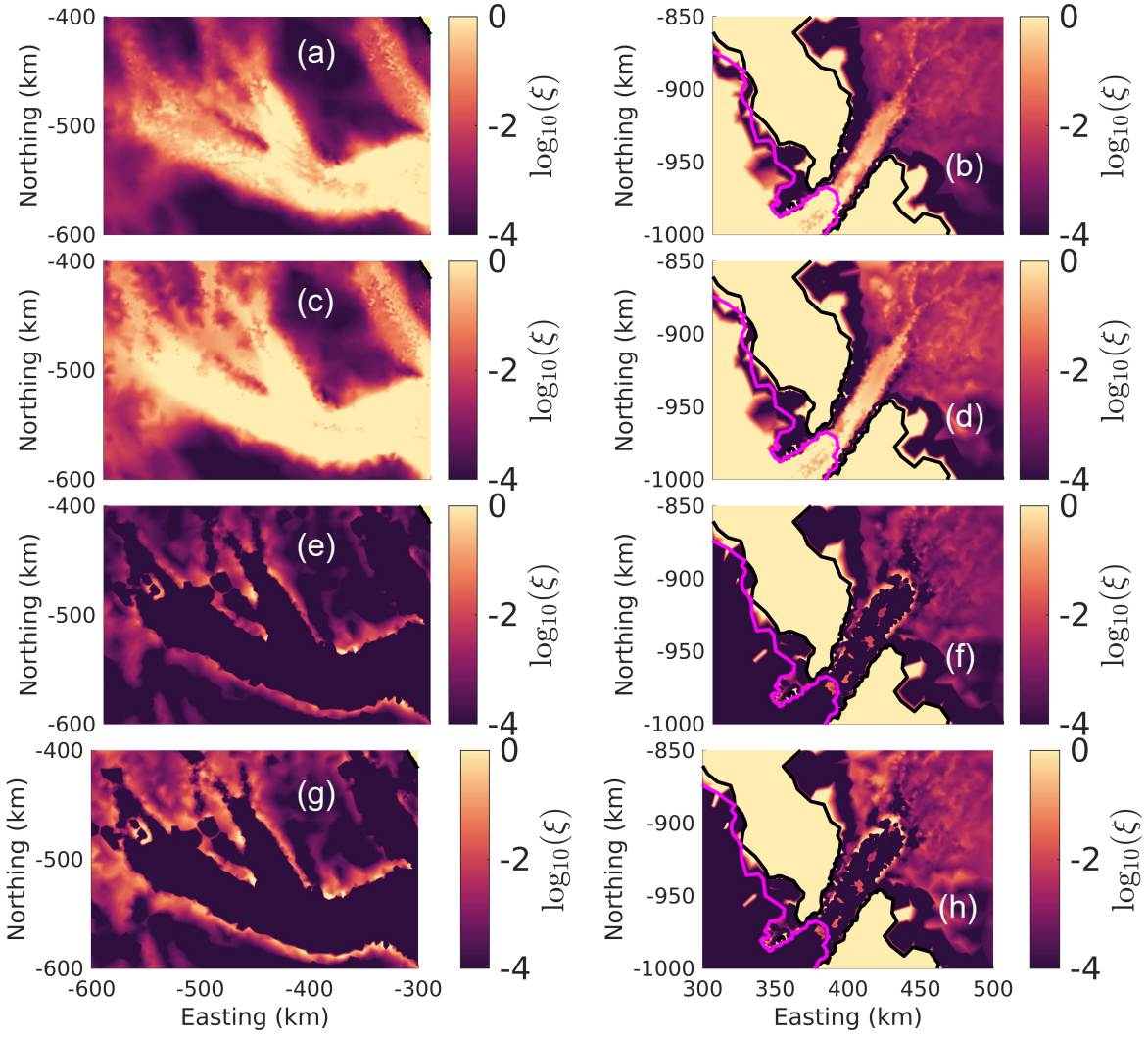

Figure 3.14: Sliding regime (ξ) in 2010 and 2100 for the Byrd Glacier and Ice Stream B. (a) $\log_{10}(\xi)$ for C at 2010 in Ice Stream B; (b) $\log_{10}(\xi)$ for C at 2010 in Byrd Glacier; (c) $\log_{10}(\xi)$ for C at 2100 in Ice Stream B; (d) $\log_{10}(\xi)$ for C at 2100 in Byrd Glacier; (e) $\log_{10}(\xi)$ for CS1 at 2010 in Ice Stream B; (f) $\log_{10}(\xi)$ for CS1 at 2010 in Byrd Glacier; (g) $\log_{10}(\xi)$ for CS1 at 2100 in Ice Stream B; (h) $\log_{10}(\xi)$ for CS1 at 2100 in Byrd Glacier. Black lines are the domain boundary and pink lines are the initial grounding line.

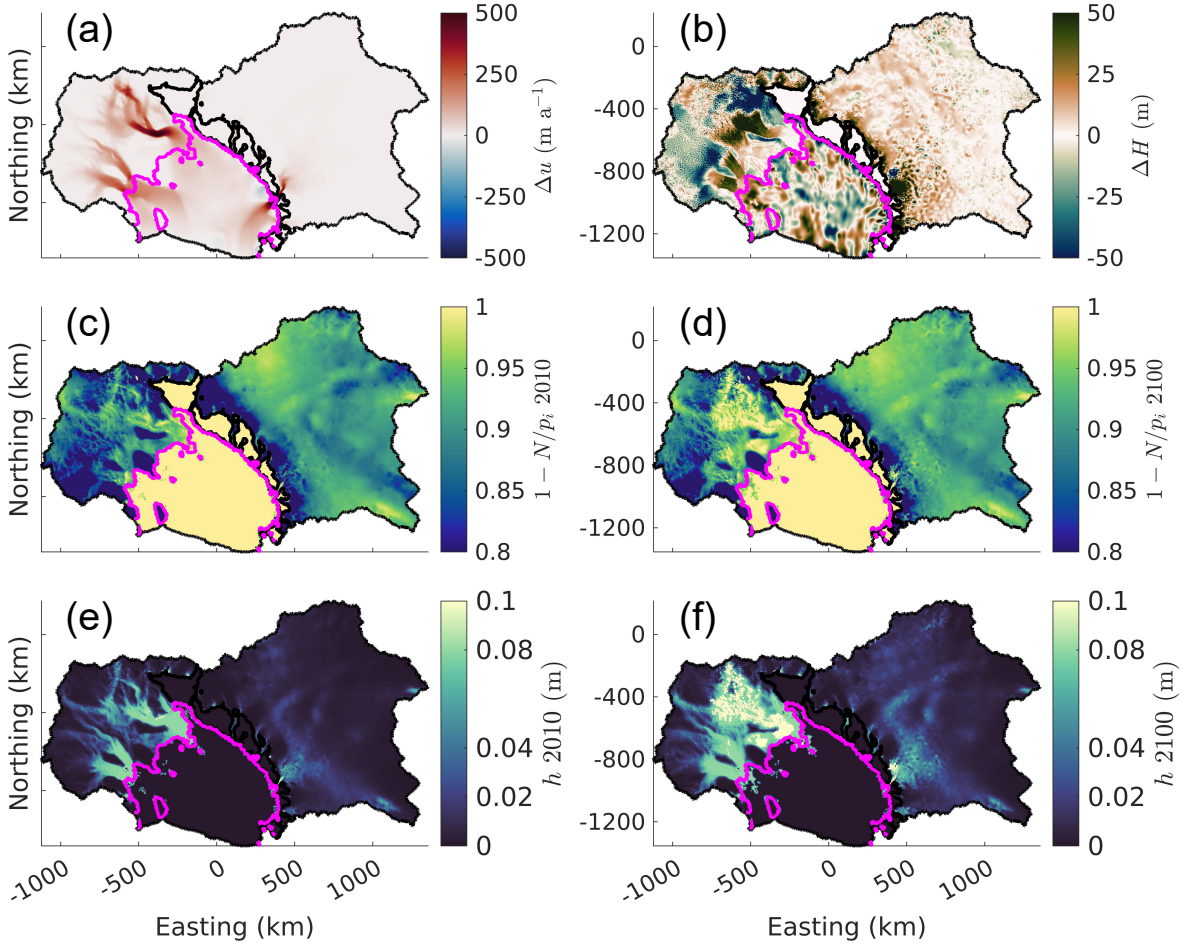

Figure 3.15: Spatial changes in flotation fraction, hydrology sheet thickness, and ice speed and thickness for CB. (a) Change in ice speed from 2010-2100 in CB (m a^{-1}); (b) Change in ice thickness from 2010-2100 in CB (m); (c) fraction of flotation at 2010 in CB; (d) fraction of flotation at 2100 in CB; (e) hydrology sheet thickness at 2010 in CB (m); (f) hydrology sheet thickness at 2100 in CB (m). Black lines are the domain boundary and pink lines are the grounding line.

over the course of the model run (Fig. 3.15c,d) the basal shear stress will lower as well, causing inland ice to speed up. In C and CS1 this doesn't happen because low values of ξ mean that the effective pressure has negligible influence on the basal shear stress, so it will remain more constant throughout the simulation.

The increased hydrology sheet opening rate from the faster ice motion caused a much larger portion of the domain upstream of Ice Stream B to have a hydrology sheet thickness closer to the typical bedrock bump height (Fig. 3.15e,f).

Despite the increased flotation fraction under the Kamb Ice Stream (Ice Stream C) in CB (Fig. 3.15f), which even reaches flotation in some areas, the Kamb Ice Stream does not reactivate. Though the Budd friction law has a linear dependence on the effective pressure, there are three things preventing the reactivation of the Kamb Ice Stream in CB. The first is the effective pressure cap, the choice to cap the effective pressure at $0.03p_i$ means that the basal shear stress can only reduce by a factor of 2 to 3 as the effective pressure falls from $0.06p_i$-$0.08p_i$ to $0.03p_i$ over the course of the simulation. The second reason that Kamb Ice Stream doesn't reactivate is that the Budd friction law has a $u^{1/3}$ dependence. An ice speed of $100\,\mathrm{m\,a^{-1}}$, which is approximately 33-50 times larger than its initial value of 2-3 $\mathrm{m\,a^{-1}}$, would mean that the basal shear stress would increase by a factor of 3.2 to 3.7, negating the affect of the effective pressure's influence on the basal shear stress. As it is, the Kamb Ice Stream speeds up to not quite $20\,\mathrm{m\,a^{-1}}$ over the course of CB. Finally, high simulated friction at the onset of the Kamb Ice Stream furthers the difficulty of reactivation.

Varying the value of ζ in the hydrology-modified Schoof friction law does not appear to alter the long term trends in ice speed in the Siple Coast ice streams and Byrd Glacier. However, it does seem to change the degree to which these trends are exaggerated, with a larger value of ζ increasing the degree to which ice speed changes. In the straightforward ice speed trends of Ice Stream A and Byrd Glacier this is easily observed (Fig. 3.16a,e). In ice streams D and E, the characteristic ice speed variability is exaggerated when $\zeta = 3 \cdot 10^7\,\mathrm{m^{-4}\,kg\,s}$ so that ice speed in Ice Stream E in CS2Z3 is sometimes below C and sometimes CS2Z1 values, which doesn't happen in the other ice streams (Fig. 3.16c,d). Unlike the other Siple Coast ice streams, Ice Stream B slows down before speeding up in all simulations. From Fig. (Fig. 3.16b) we see that not only does the value of ζ impact the degree to which the ice stream slows down and speeds up, but also at what time the speedup is initiated. In CS2Z1 the speedup is initiated in 2078, in C the speedup is initiated in 2069, and in CS2Z3 the speedup is initiated in 2025. The ice speed discrepancy between the three models can be easily explained by the cubic dependence of ξ on ζ. A larger ζ and correspondingly more Iken sliding regime will mean that the effective pressure will have a larger influence on the basal shear stress throughout the domain. Because of this, having a larger value of ζ produces more exaggerated trends in ice motion and ice motion variability in the case of ice streams D and E. In the case of Ice Stream B, the basal shear stress at the onset of the ice stream drops much faster in CS2Z3 compared to C and CS2Z1, which manifests as ice stream speed up much earlier in the model run.

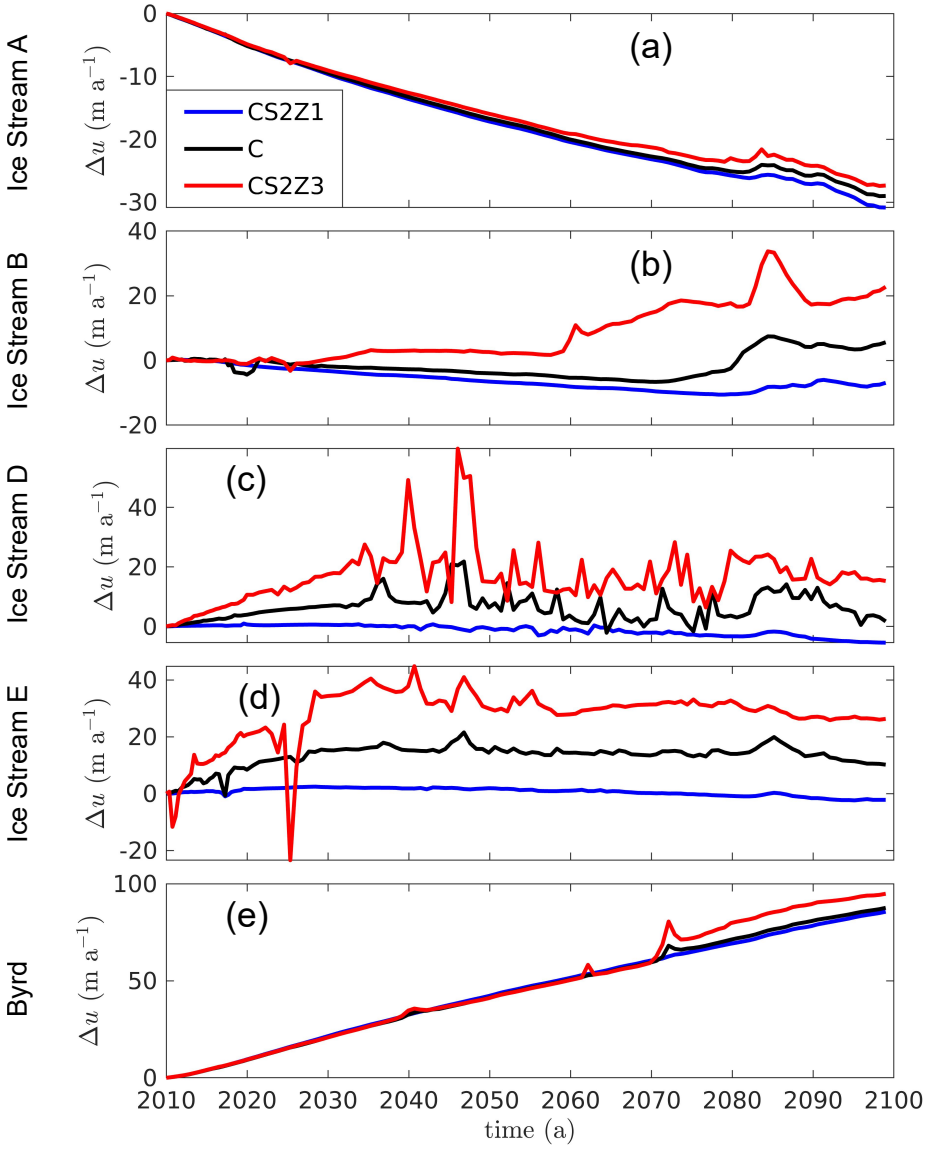

Figure 3.16: Comparison between the dynamics of the Siple Coast ice streams and Byrd Glacier for CS2Z1, C, and CS2Z3. (a) change in Ice Stream A ice speed (m a^{-1}); (b) change in Ice Stream B ice speed (m a^{-1}); (c) change in Ice Stream D ice speed (m a^{-1}); (d) change in Ice Stream E ice speed (m a^{-1}); (e) change in Byrd Glacier ice speed (m a^{-1}).

All values of ζ produce similar patterns in effective pressure and hydrology sheet thickness (Fig. 3.17). While it is clear that the effective pressure lowers over the course of each coupled simulation, the relationship between the effective pressure fields of the different coupled models is more complicated. CS1 and C have very similar effective pressure fields (Fig. 3.18a) with the largest difference coming at the boundary in the interior of the East Antarctic Ice Sheet where C is more pressurized. CB has a generally lower flotation fraction than C except surrounding the fast flowing regions where it has a generally higher flotation fraction than C (Fig. 3.18b). From CS2Z1 and CS2Z3 we see that the average flotation fraction appears to decrease when ζ is increased. These phenomenon can be explained by a negative feedback mechanism, where faster ice creates a larger cavity opening rate and depressurizes the system. In the models where the effective pressure has a larger influence on the basal shear stress the distributed sheet system is less pressurized.

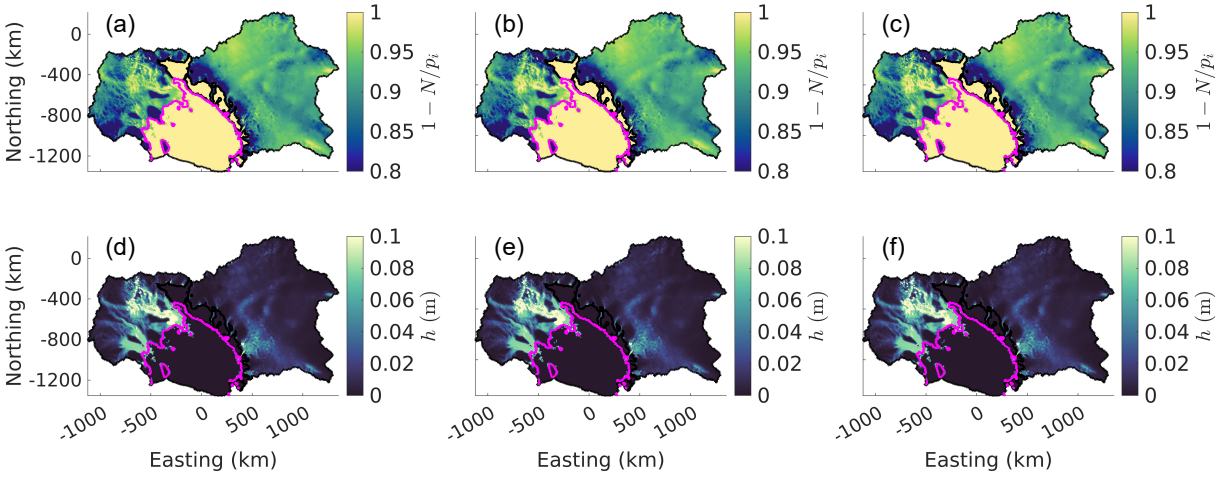

Figure 3.17: Flotation fraction and hydrology sheet thickness at 2100 for CS2Z1, C, and CS2Z3. (a) flotation fraction for CS2Z1; (b) flotation fraction for C; (c) flotation fraction for CS2Z3; (d) hydrology sheet thickness for CS2Z1 (m); (e) hydrology sheet thickness for C (m); (f) hydrology sheet thickness for CS2Z3 (m), Black lines are the domain boundary and pink lines are the initial grounding line.

However, by the end of the model runs these trends break down and are in some regards reversed. In CB, 13.2 % of the domain was above a fraction of flotation of 0.95 in 2100, as opposed to 13.0 %, 12.3 %, 12.1 % and 11.0 % for CS2Z3, C, CS2Z1, and CS1 respectively. The models with fewer low effective pressure areas have higher ice speed in the fast flowing regions of the domain. This may be a result of dynamic thinning of ice increasing the area

of hydraulic potential dips, which leads to larger pressurized regions of the domain. From this, a second feedback mechanism is identified between effective pressure and ice speed, where lower effective pressure corresponds to faster ice. In regions where there are slow changes in effective pressure and ice speed, the negative feedback mechanism discussed above will dominate, but in regions where there are faster changes in effective pressure and ice speed resulting in dynamic thinning of ice the positive feedback mechanism will dominate.

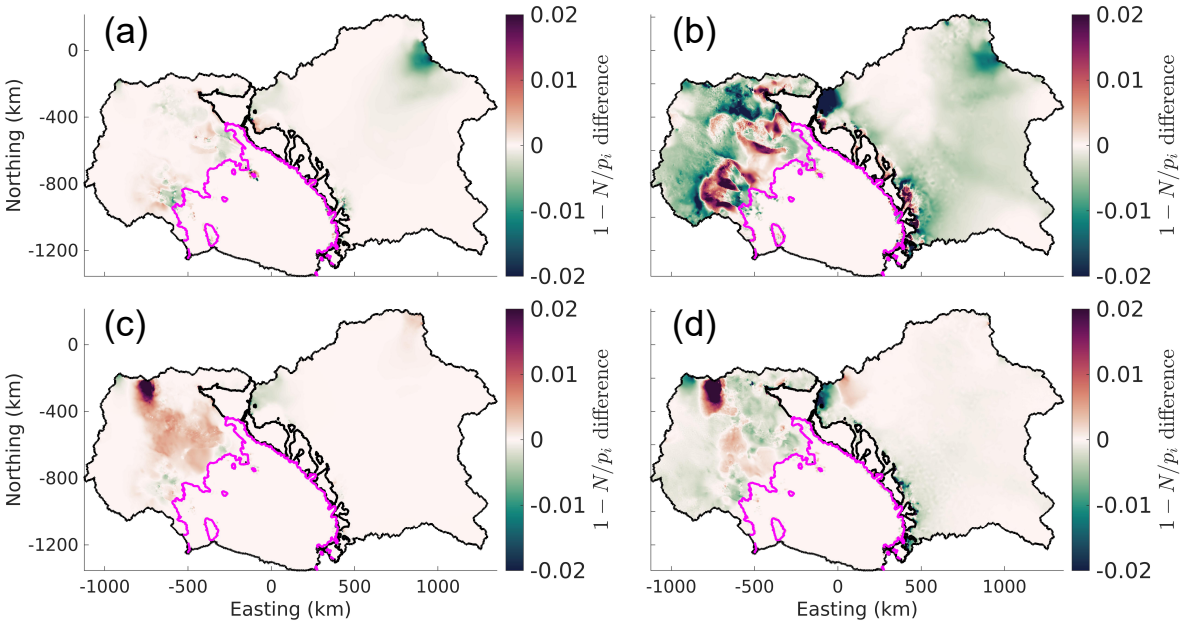

Figure 3.18: Difference in temporally averaged flotation fraction between coupled models. (a) difference between CS1 and C; (b) difference between CB and C; (c) difference between CS2Z1 and C; (d) difference between CS2Z3 and C. Black lines are the domain boundary and pink lines are the grounding line.

3.3.2 Melt input

The ice streams of the Siple Coast and the Byrd Glacier behave similarly in both C and CM with the exception of Ice Stream A which sped up by 21.8 m a^{-1} between 2086 and 2087 in CM (Fig. 3.19a). Ice streams D and E were slower in CM compared to C (Fig. 3.19c,d), with a slight trend of slow-down in Ice Stream E starting around 2043. The ice speed

variability in ice streams D and E was reduced in CM compared to C, especially in the second half of the simulations, as a result of a more stable subglacial hydrological system. Given that such stability is not observed when a constant melt rate is applied and the effective pressure and water input are overall lower in the variable melt simulations, the stability in ice streams D and E in CM can be attributed to negative feedback loops between melt input to the subglacial hydrological system and the basal shear stress, which act to keep them in equilibrium. In constant melt simulations, perturbations in the basal shear stress are capable of growing larger as there is no change in melt rate to compensate them as in the variable melt simulations.

The speedup of Ice Stream A can be attributed to hydrologic activation of the ice stream onset (Fig. 3.20), which manifests as an initial pulse of ice speedup followed by deceleration (Fig. 3.19a), despite still maintaining a pressurized hydrological system. Such hydrological features are unique to CM, not occurring in FC, the other variable melt simulation. In fact, not only does this hydrologic activation at the onset of Ice Stream A not occur in FC, but FC experiences significantly reduced flooding under Ice Stream B during the last couple of decades of the simulation as well. The flooding of Ice Stream A in CM can be attributed to the build up and release of water further upstream, which occurred only in CM. The water was generated from ice flow over nearby high friction areas, which had minimal melt in the coupled simulations with constant melt. The small change in ice speed despite the drastic change in the hydrological system suggests that Iken's bound is overestimated in this area of the domain. Similar overestimations of Iken's bound in the Kamb Ice Stream close to the grounding line lead to minimal ice speedup despite a flooded subglacial hydrologic system.

3.3.3 Driving stress

Trends in ice speed for CD match closely with those from C for most of the ice streams in the Siple Coast and for Byrd Glacier (Fig. 3.19). Ice streams D and E experience comparable variability in ice speed, though the trend in variability in ice stream D does not match up between C and CD. Unlike the other ice streams of the Siple Coast, Ice Stream B has a large deviation in ice speed between C and CD. In CD, Ice Stream B speeds up during the characteristic flooding of the 2080s, which occurs in all coupled models except FC. By 2084 Ice Stream B reaches $69.1\,\mathrm{m\,a^{-1}}$ above its starting speed, before falling back to $6.0\,\mathrm{m\,a^{-1}}$ above its starting speed in 2086.

Taking h_l into account when computing the driving stress leads to general decreases in driving stress, except in areas where there are deep subglacial lakes, which correspond to sharp increases in driving stress (Fig. 3.21c). Despite the generally lower driving stress

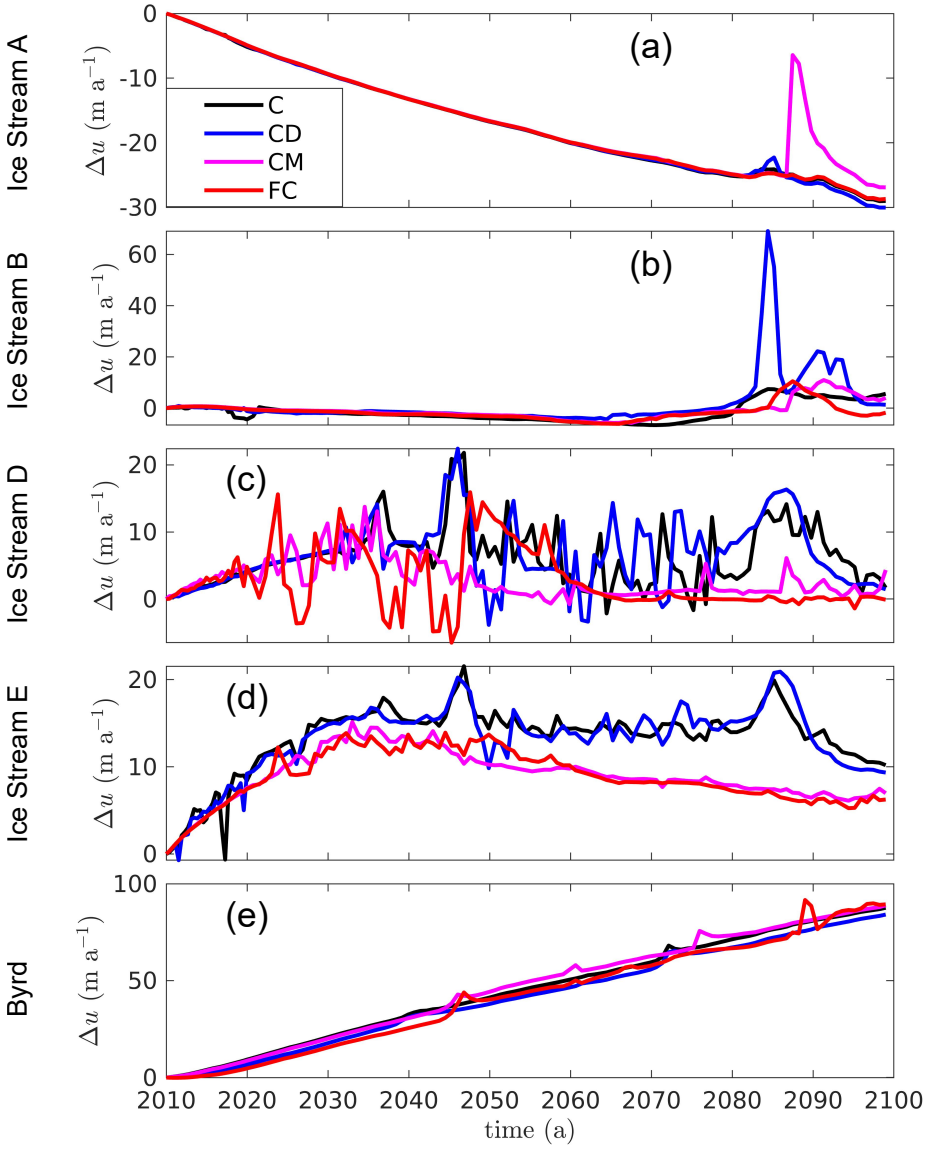

Figure 3.19: Comparison between the dynamics of the Siple Coast ice streams and Byrd Glacier for C, CD, CM, and FC. (a) change in Ice Stream A ice speed (m a^{-1}); (b) change in Ice Stream B ice speed (m a^{-1}); (c) change in Ice Stream D ice speed (m a^{-1}); (d) change in Ice Stream E ice speed (m a^{-1}); (e) change in Byrd Glacier ice speed (m a^{-1}).

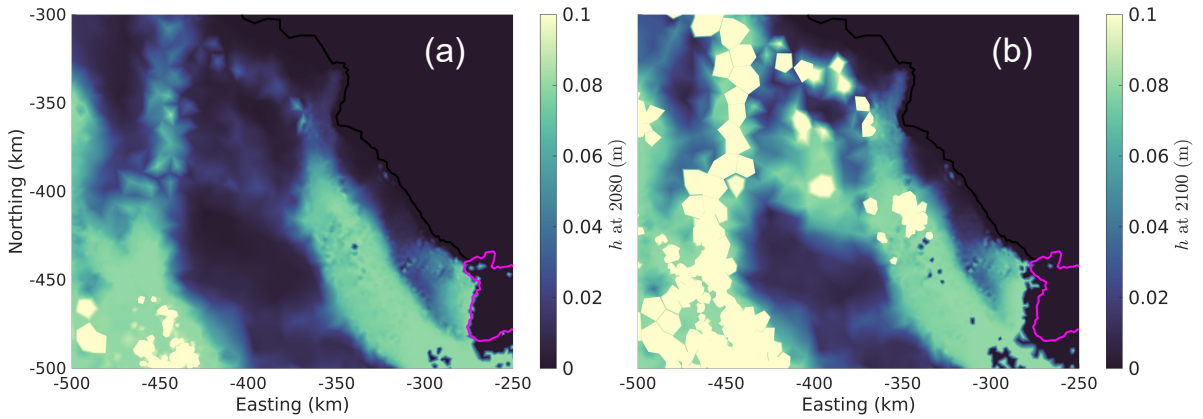

Figure 3.20: Hydrology sheet thickness for CM for various times. (a) hydrology sheet thickness at 2080 (m); (b) hydrology sheet thickness at 2100. Black lines are the domain boundary and pink lines are the grounding line.

computed with h_l, a higher driving stress at the onset of the eastern tributary of Ice Stream B corresponding to rapid subglacial lake filling, caused enhanced speed up of the ice stream in 2082. This large speedup occurs in parallel with a large slow down of upstream ice (Fig. 3.21b,d), allowing for extreme localized thinning at the onset of the ice stream of more than 10 m in one year (Fig. 3.21a). Other noticeable areas of ice thinning occur at the boundaries between ice speedup and ice slowdown, which often occur in areas with subglacial lakes.

Lakes which cause local driving stress increases and upstream driving stress decreases result in ice speedup and localized thinning of ice. This thinner ice furthers the overburden hydraulic potential low of the subglacial lake resulting in further water accumulation. This runaway positive feedback loop is stopped when a significant speedup of downstream ice increases the cavity opening rate and the lake drains to fill them. Though this positive feedback loop blows up in Ice Stream B the lakes in CD are for the most part stable. Most of the major subglacial lakes of CD are deeper than in C due to the shift in the lake equilibrium depth from ice thinning. Conversely, if lakes cause local driving stress decreases then slower ice resulting in ice thickening will raise the overburden hydraulic potential low resulting in less water accumulation. Such processes can be observed in the subglacial lakes of Ice Stream B. The lake depth in CD is consistently larger than that of C leading up to the flooding of the 2080s (Fig. 3.22), after which, rapid drainage in CD allows the model to maintain a much shallower lake, with one of the lakes completely

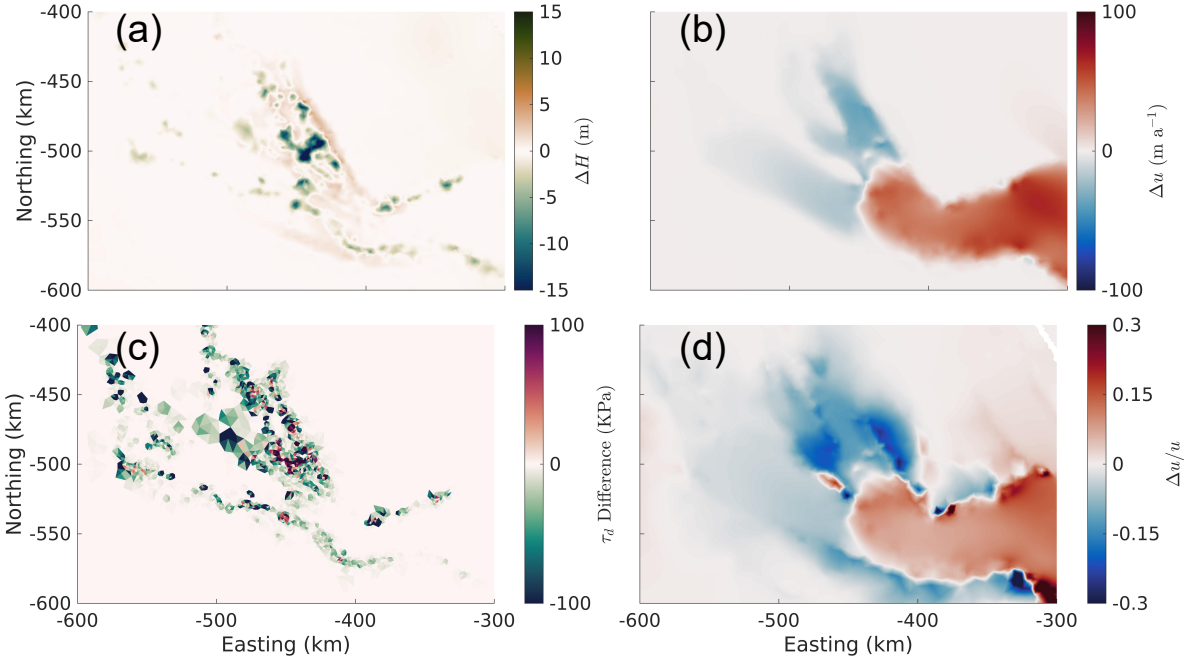

Figure 3.21: Speedup of Ice Stream B during 2082 in CD (2082.1 to 2082.9). (a) Change in ice thickness (m); (b) change in ice speed (m a^{-1}); (c) difference in computing driving stress with and without h_l (KPa); (d) relative change in ice speed.

draining (Fig. 3.22b). The enhanced drainage of the lakes in CD can be attributed to the large ice speedup of Ice Stream B (Fig. 3.21b), which increased the cavity opening rate surrounding the lakes, forcing them to drain.

3.3.4 Full coupling

FC, which includes both variable melt as in CM and a hydrology layer driving stress contribution as in CD, displays ice speed patterns with characteristics from both CM and CD but without instability. Ice Stream A does not have the pulse of ice speed from activation of the hydrologic system at the ice stream onset as in CM (Fig. 3.21a). Ice Stream B displays minimal speedup, comparable to that of C and CM (Fig. 3.21b), and does not flood to the same extent as any of the other coupled models. Ice Stream D displays comparable variability in FC as it does in C or CD, but only in the first half of the simulation. In the second half of the simulation there is minimal ice speed variability as in

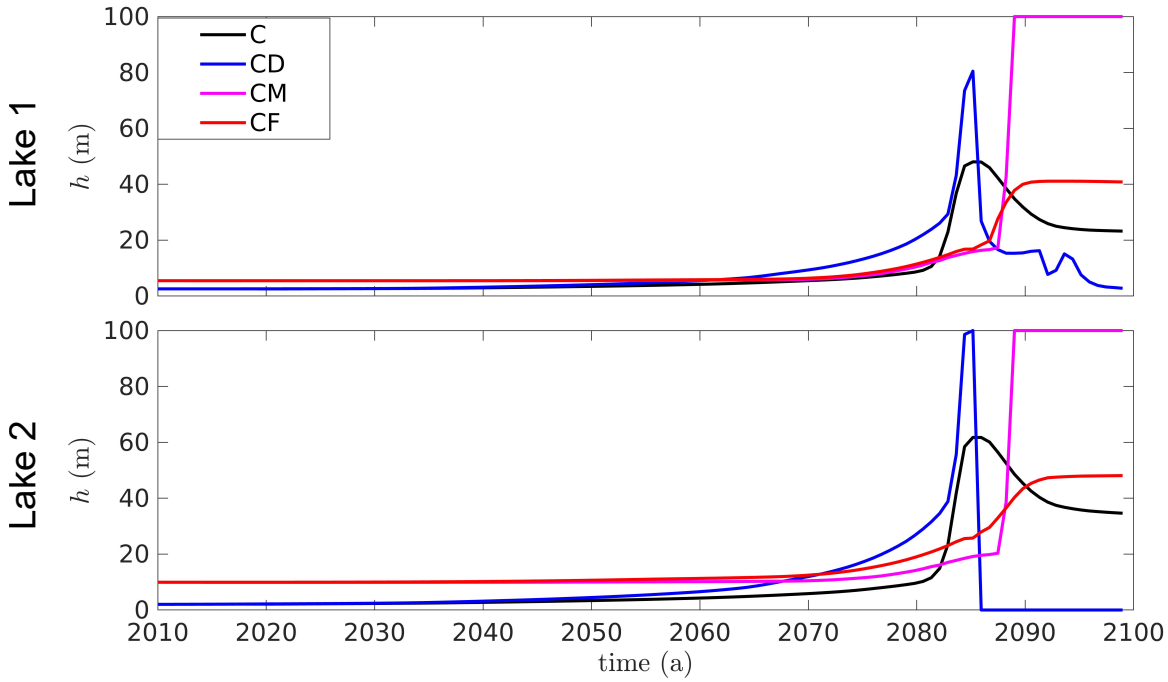

Figure 3.22: Lake depth for two lakes underneath Ice Stream B in C, CD, CM, and FC. (a) depth of upstream lake (m); depth of downstream lake (m).

CM (Fig. 3.21c). Ice Stream E has the same trends in ice speed in FC and CM with small discrepancies in ice speed arising from ice speed variability of the two models (Fig. 3.21d). Byrd Glacier behaves similar in C, CM, CD, and FC with a general trend of increasing ice speed and small positive perturbations in this trend (Fig. 3.21e).

The general stability of FC in comparison to CM and CD suggests that the altered driving stress in combination with the variable melt rate generates a negative feedback loop, which smooths ice speed trends. The reduced ice speedup in ice streams A and B in FC can be attributed to these feedback mechanisms as there is a reduction in subglacial lake area underneath the ice streams as well. The only time FC has less stability than the other models is in the first half of the simulation in Ice Stream D, where FC has enhanced ice speed variability. This suggests the possibility of a positive feedback mechanism, which acts to destabilize ice speed trends.

Unlike the subglacial lakes under Ice Stream B in C and CD, the lakes in FC don't drain after they fill in the 2080s. Rather, they move to a new equilibrium depth over a timescale which is longer than that of the lake fill in C and CD (Fig. 3.22). This can be

interpreted as the extension of the feedback mechanisms which cause ice motion stability in FC. The longer timescales associated with lake depth evolution in FC allows for the lake depth to not overshoot causing lake drainage as in C and CD.

FC gives hydrology results that differ from those of C and HM2K1, and ice flow results that differ from those of IS2 and C. The Siple Coast ice streams of FC by the end of the model run are faster than those of C and slower than those of IS2, trends which propagate into the ice shelf (Fig. 3.23a,b). The fraction of flotation in FC is generally smaller than in HM1K1 (Fig. 3.23c), and the hydrology sheet is generally not as thick (Fig. 3.23e). These results are likely a consequence of the increased sheet conductivity of FC compared to HM1K1. Despite the generally thinner hydrology sheet, the subglacial lakes under Ice Stream B are deeper in FC than HM1K1. The fraction of flotation in FC is generally larger than in C in the slow moving regions of the domain, but larger than in C under ice streams A and B (Fig. 3.23d). Similarly, the hydrology sheet is generally thicker in FC than in C, especially in the slow moving regions of the East Antarctic Ice Sheet (Fig. 3.23f). However, the hydrology sheet is much thinner under Ice Stream B, where C experienced flooding in the last couple decades of the simulation. The vastly different results of the fully coupled model compared to both the coupled model, and the ice flow-only and hydrology-only models displays the importance of capturing the physics behind more processes involved with ice/hydrology feedback moving forwards.

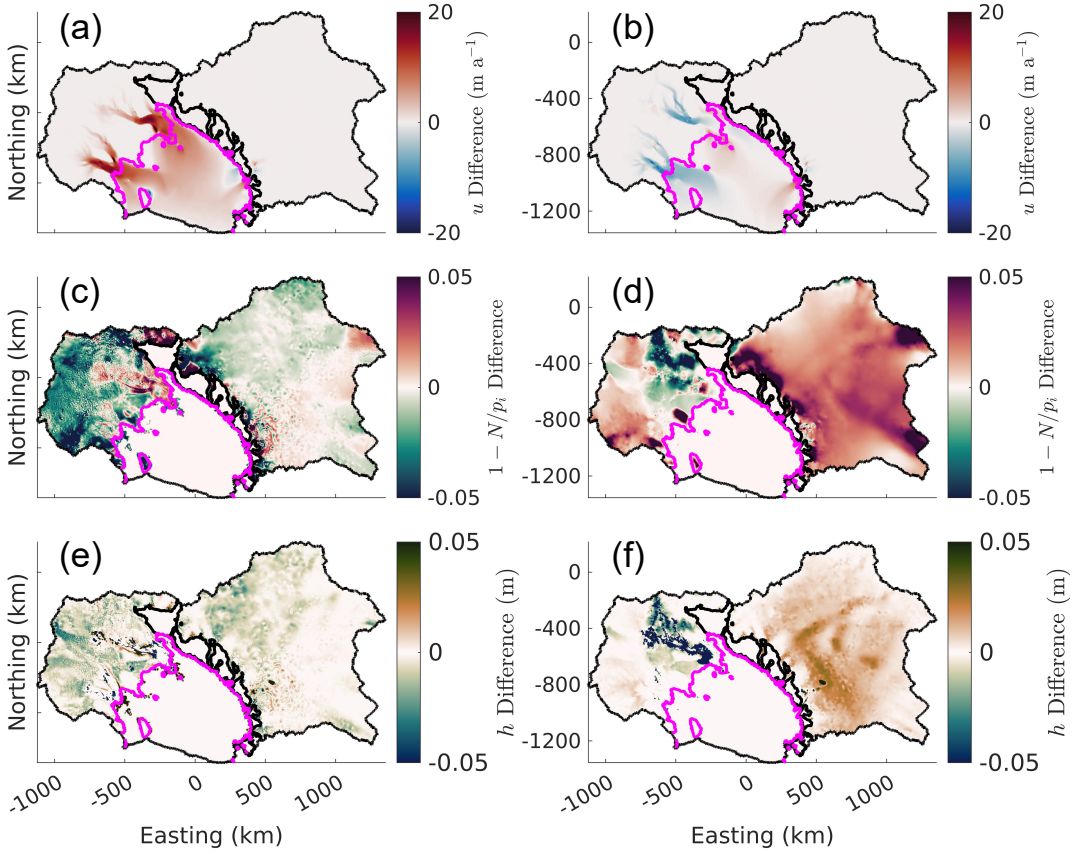

Figure 3.23: Comparison between final outputs of FC, C, IS2, and HM1K1. (a) ice speed difference between FC and IS2 (m a^{-1}); (b) ice speed difference between FC and C (m a^{-1}); (c) fraction of flotation difference between FC and HM2K1; (d) fraction of flotation difference between FC and C; (e) hydrology sheet thickness difference between FC and HM2K1; (f) hydrology sheet thickness difference between FC and C. Black lines are the domain boundary and pink lines are the grounding line.

Chapter 4

Discussion

We discuss here the results of Section 3, model shortcomings, and potential model improvements. In Section 4.1 we discuss modeled ice flow and subglacial hydrologic patterns of the Siple Coast in comparison with past research in the area. In Section 4.2 we discuss the implementation of friction in ice flow models including the impact of various friction laws, effective pressure parameterizations, and ice flow approximations on the evolution of the basal shear stress. In Section 4.3 we discuss the impact of additional coupling components and identify ice/hydrology feedback mechanisms. We close with Section 4.4, discussing potential future improvements for GlaDS.

4.1 Siple Coast

Here, we discuss the modeled ice flow and subglacial hydrology patterns of the Siple Coast found during this study in comparison to previous work. We begin with a discussion of ice flow patterns in the Siple Coast ice streams and Byrd Glacier in Section 4.1.1, and continue to discuss subglacial lake locations in Section 4.1.2 and the broader subglacial hydrologic system in Section 4.1.3.

4.1.1 Patterns in ice flow

With the exception of CB, all models suggest that Ice Stream B will slow down over the next couple decades. However, the models disagree with how long the slow down will last, with the onset of subsequent speedup ranging from 2025 in CS2Z3 to 2082 in the ice flow models;

Ice Stream B does not speed up in IS2-control during the 90 year simulation. Stearns et al. (2005) observed the ice dynamics of Ice Stream B from 1987 to 1997 using interferometric satellite radar (InSAR), and found a slowdown of 2.9-4.1 $\mathrm{m\,a^{-2}}$. This previous slow down observed by Stearns et al. (2005) is much greater than the future slowdown predicted in our models, which don't quite slow down by 20 $\mathrm{m\,a^{-1}}$ by 2082 (0.2 $\mathrm{m\,a^{-2}}$). Catania et al. (2012) noted that the rate of slow down observed by Stearns et al. (2005) would result in the complete stagnation of Ice Stream B by 2070-2080. The discrepancy between the rate of slow down observed by Stearns et al. (2005) and our modeled rate of slow down may be a consequence of the initialization procedure underestimating the initial ice speed of Ice Stream B by in some places up to 100-150 $\mathrm{m\,a^{-1}}$ (Fig. 4.1a). Bougamont et al. (2015) modeled the ice dynamics of the Siple Coast 250 years into the future and found a slowdown of Ice Stream B, which did not stagnate or speed up over the course of their 250 year simulation. Their setup did not include a surface mass balance forcing scenario, which agrees with the prolonged slowdown experienced in IS2-control and highlights the potential importance of future surface mass balance forcing in the region. Given observations from Stearns et al. (2005), modeling from Bougamont et al. (2015), and our modeling, it is likely that Ice Stream B will continue to slow down for the coming decades.

The ability of the Schoof friction law to speed up Ice Stream B, despite the prediction of a strong Weertman sliding regime inside the ice stream suggests that the basal shear stress in the ice stream onset – where the sliding regime was more Iken – has a stronger control on ice stream evolution than the basal shear stress within the ice stream. The speedup of Ice Stream A in CM due to the activation of the subglacial hydrologic system at the ice stream onset, and the speedup of Ice Stream B in CD due to increased driving stress at the ice stream onset further this notion. This finding agrees with that of Winberry et al. (2007), who observed ice speed using GPS tracking near the onset of Ice Stream D, and found the migration of the ice stream onset has a significant control on the ice stream speed.

Catania et al. (2012) and Bougamont et al. (2015) both suggested that the Kamb Ice Stream will reactivate following the slow down and possible stagnation of Ice Stream B. Bougamont et al. (2015) found that the Kamb Ice Stream reactivation would occur 100 years into their model run, suggesting that a Kamb Ice Stream reactivation may not occur in the 90 year simulation of this study. Despite this, the subglacial hydrologic system under the Kamb Ice Stream activated in CB. Yet, no models had Kamb display ice speeds of more than 30 $\mathrm{m\,a^{-1}}$ by the end of the simulation. The lack of a Kamb Ice Stream reactivation despite the apparent subglacial hydrologic reactivation in CB may be a consequence of overestimating upglacier basal friction, and the dependence of the basal shear stress on the sliding speed even with a pressurized subglacial hydrologic system in the Budd friction

law. Elsworth and Suckale (2016) modeled the affect of the efficiency of the subglacial hydrologic system on the ice motion of Kamb Ice Stream and found that the subglacial water pressure has a large control on ice motion in the Kamb Ice Stream. This implies that pressurized subglacial hydrologic system in CB should result in the reactivation of Kamb. Bougamont et al. (2015) found that the initial reactivation of the Kamb Ice Stream was due to an increase in driving stress, with an active subglacial hydrologic system following as a result of the ice stream reactivation. However, the implementation of basal friction used by Bougamont et al. (2015) does not have an ice speed dependence, which would ease in the Kamb Ice Stream reactivation compared to using the Budd friction law.

In all model outputs, Byrd Glacier experiences tremendous speedup in excess of $100\,\mathrm{m\,a^{-1}}$ from its starting value, accompanied by thickening of ice. Byrd Glacier has been observed to have minimal change in ice speed (Van Der Veen et al., 2014) with fluctuations occurring from subglacial lake drainage events (Stearns et al., 2008). The speedup of Byrd Glacier in all models can be understood as a model initialization problem, with Byrd's starting speed more than $100\,\mathrm{m\,a^{-1}}$ below observed values in all models. Byrd's confinement to a trough results in high lateral friction areas (Van Der Veen et al., 2014), which are interpreted as high basal friction areas in the ice flow model. This high friction tends to greatly underestimate ice speed at the sidewalls of Byrd, with less of an underestimation in the Byrd interior. Similarly in the Siple Coast, at ice stream boundaries there is a large gradient in modeled friction resulting in a large overestimation of ice speed at the ice stream margins and an underestimation in the ice stream interior (Fig. 4.1). The failure of the ice flow model to capture the high lateral shear in these regions results in a poor model spinup, which can dominate ice flow trends. The temporal ice flow variability and the sensitivity of GlaDS to an evolving ice sheet make the time chosen for the model to relax somewhat subjective. Future work in model initialization, although beyond the scope of this work, is critical in glacier modeling.

4.1.2 Subglacial lakes

Subglacial lakes formed in all models where GlaDS was run, with the lakes underneath Ice Stream B and Byrd Glacier being the most robust against a higher sheet conductivity. In the lower sheet conductivity runs and the coupled runs, subglacial lakes also formed under ice streams D and E. Lakes did not form under Ice Stream A or the Kamb Ice Stream in any of the models with a hydrology component, and lakes only formed in the interior of the East Antarctic Ice Sheet in the HM2K1 simulation, where there was available melt water in the subglacial hydrological system and a low enough sheet conductivity that it did not drain out of the system. Comparing against known locations of subglacial lakes

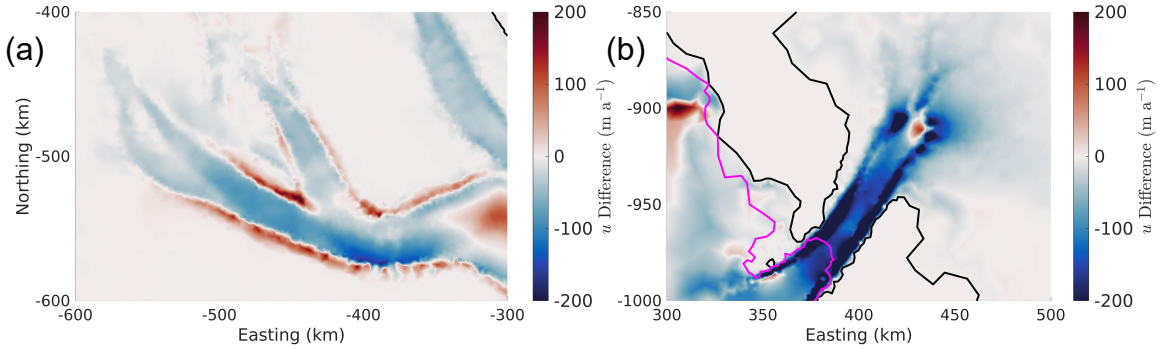

Figure 4.1: Difference between model initialization (applied in all ice flow and coupled runs) ice speed and observed ice speed from (Morlighem et al., 2020). (a) Ice Stream B; (b) Byrd Glacier. Black lines are the domain boundary and pink lines are the initial grounding line.

from Livingstone et al. (2022), there are both lakes from Livingstone et al. (2022) that do not appear in our models, and lakes in our models that do not appear in Livingstone et al. (2022). Lakes that appear in both our models and Livingstone et al. (2022) lie underneath ice streams B and E in the Siple Coast. Livingstone et al. (2022) found lakes under Ice Stream A and the Kamb Ice Stream (Kim et al., 2016), which did not appear in our models, and our models suggested the existence of lakes under Ice Stream D, which were not observed by Livingstone et al. (2022). Livingstone et al. (2022) also predicted a large number of lakes in the interior of both the East and West Antarctic ice sheets, which only appear in our models when the sheet conductivity is lowered below $10^{-3}\,\mathrm{m}^{7/4}\,\mathrm{kg}^{-1/2}$, which far over-predicts ice speeds in the ice sheet interior.

The lakes under Ice Stream B had long fill/drain cycles, changing in depth on the order of tens of meters. This is larger than ice surface elevation anomalies modeled and observed from Carter et al. (2013), which were on the order of one meter. These lakes under Ice Stream B were not reoccurring. However, the lakes under ice streams D and E experienced timescales of fill and drain that were comparable to the timescales suggested by Carter et al. (2017), with unpredictable patterns in the coupled models. The lake depth changes in these models were also comparable to those from Carter et al. (2013). The fill/drain cycles observed under ice streams D and E were a consequence of a temporally variable hydraulic potential field on length scales much larger than the width of subglacial lakes, causing multiple subglacial lakes to fill and drain simultaneously. Such lake dynamics are not suggestive of the interconnected nature of upstream lakes draining into downstream lakes observed by Siegfried et al. (2016) downstream of ice streams A and B in the Whillans

Ice Plain.

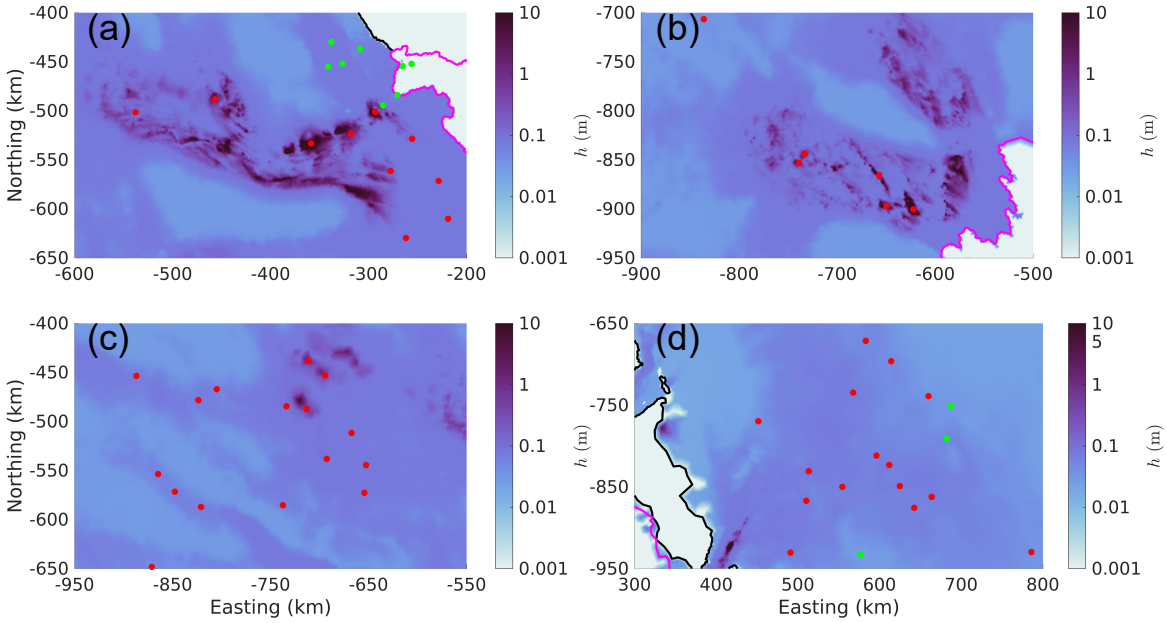

Figure 4.2: Maximum hydrology sheet thickness from HM1K1 and observed subglacial lake locations from Livingstone et al. (2022). (a) ice streams A and B; (b) ice streams D and E; (c) West Antarctic Ice Sheet interior, upstream of Ice Stream B; (d) East Antarctic Ice Sheet interior, upstream of Byrd Glacier. Red dots are observed active subglacial lakes and green dots are observed stable subglacial lakes. Black lines are the domain boundary and pink lines are the grounding line. Two observed lakes in (a) appear in the ocean demonstrating errors in ice and bed geometry from Morlighem et al. (2020).

The discrepancy between known and modeled subglacial lake locations could be a consequence of errors in ice geometry and bed topography data from Morlighem et al. (2020). Lakes occur in regions where there are hydraulic potential lows, which are highly sensitive to ice thickness and bed elevation gradients. Areas where subglacial lakes are predicted by our models but are not yet observed may just require further observation. Of note, is the absence of Lake Vostok in our model, which has an observed depth of over 500 m (Kapitsa et al., 1996). The bed topography data from Morlighem et al. (2020) was created using observed ice speed and thickness data, and using mass conservation to extrapolate the data over the ice sheet. The bed elevation from this process fails to account for the existence of large layers of subglacial water and places the glacier bed where the surface

of a hypothetical subglacial lake should be. The observed ice thickness/bed elevation data would also fail to account for subglacial water layers, as radar reflects off the surface of subglacial water and does not make it to the glacier bed. For most subglacial lakes with minimal depth this is not usually an issue. However, when it comes to deep subglacial lakes, such as Lake Vostok, hundreds of meters of bed uplift from basal water eliminate hydraulic potential lows. Stable lakes identified by Livingstone et al. (2022) as lakes that have approximately equal inflow and outflow and are primarily detected by radio-echo sounding (RES), therefore may not be observed in our models due to an overestimation of bed elevation from Morlighem et al. (2020), which smooths out hydraulic potential lows. Indeed none of the stable subglacial lakes from (Livingstone et al., 2022) appear in our models. Active lakes that have a maximum lake depth at the time of surface elevation observation and radar surveys will also overestimate bed elevation and may not appear in our models. Additionally the nature of using mass conservation and sparse ice thickness measurements to determine bed topography results in both ice thickness and bed elevation errors, to which subglacial lake locations are highly sensitive. The absence of observed lakes in our models is therefore expected, but modeled lakes that are yet to be observed may still exist, and warrant inspection.

4.1.3 A soft bed hydrologic system

Channels formed in the Siple Coast ice streams and in the outlet glaciers of the TM. Channels underneath the Siple Coast ice streams don't follow a main discharge path, with channels of comparable discharge forming on element edges close to each other but flowing in different directions. Such channelization is inconsistent with our understanding of Alpine glacier and Greenland-style channelized drainage, which favours an arborescent channel system with larger channels growing at the expense of smaller ones (Shreve, 1972). The low ice surface slopes of the Siple Coast, which generate small hydraulic potential gradients may be in part responsible for this tortuous channel system. Carter et al. (2017) modeled subglacial lake drainage and determined that for fill/drain cycles to occur on time scales associated with Siple Coast subglacial lakes – a couple of years – channels incised into sediment (sediment canals) instead of ice are needed. Underlying the Siple Coast ice streams is a soft till layer (Blankenship et al., 1986; Engelhardt et al., 1990), which could conceivably allow for the growth of such sediment canals. GlaDS assumes a hard glacier bed and the formation of R-channels as opposed to sediment canals; assumptions which are inaccurate under the Siple Coast ice streams. However, the large areas of hydrology sheet thickness close to the typical bedrock bump height may be indicative of a water saturated till layer and the somewhat tortuous nature of the channel system may be indicative of the

existence of sediment canals as opposed to R-channels. The need for the maximum channel area to be lowered to $100\,\mathrm{m}^2$ to avoid blowing up the hydrology sheet from channel melt under Ice Stream B further suggests the existence of smaller sediment canals underneath the Siple Coast ice streams as opposed to large R-channels. Complex subglacial hydrology modeling has thus far primarily considered hard glacier beds (Werder et al., 2013; Sommers et al., 2018; Schoof, 2010). However, the development of soft bed complex subglacial hydrology models may be necessary to better describe the subglacial conditions of the Siple Coast.

4.2 Implementation of friction in ice flow models

As two-way coupling of ice dynamics models with complex subglacial hydrology models such as GlaDS and SHAKTI becomes more prevalent, it is important to consider the impact of different friction laws on the evolution of the basal shear stress. In Section 4.2.1 we examine how the basal shear stress changes with respect to changes in basal sliding speed and effective pressure for the Schoof, hydrology-modified Schoof, and Budd friction laws. We address the shortcomings of the present implementation of friction in ice flow models, and the desired qualities that a new friction law should have to address these shortcomings. We present one such friction law, which has these desired properties. In the absence of a two-way coupled model, which may be necessary given computational limitations, we discuss how various effective pressure parameterizations affect the evolution of the basal shear stress, and develop a parameterization to incorporate temporally variable effective pressure in ice flow-only models in Section 4.2.2. Finally, in Section 4.2.3 we discuss the impact of the SSA on the basal sliding speed, and present a parameterization of the basal sliding speed, which may be used to better incorporate the effects of vertical shear on the basal shear stress in two-dimensional ice flow models.

4.2.1 Impact of friction law on an evolving ice sheet

The denominator of the Schoof and the hydrology-modified Schoof friction laws of Eq. (2.22) and Eq. (2.27) can be written as $(1 + \xi)^m$ where ξ is a dimensionless parameter, which determines the sliding regime of the friction law. For the Schoof friction law ξ is given by Eq. (4.1) and for the hydrology-modified schoof friction law ξ is given by Eq. (4.2).

$$\xi = \left(\frac{C_s^2}{C_{\max} N}\right)^{1/m} u_b. \tag{4.1}$$

$$\xi = \left(\frac{\zeta}{N}\right)^{1/m} u_b. \tag{4.2}$$

For the Schoof friction law when $\xi << 1$ then $\tau_b = C_s^2 u_b^m$ and the friction law is in a Weertman sliding regime and when $\xi >> 1$ then $\tau_b = C_{\max} N$ and the friction law is in an Iken sliding regime. For the hydrology-modified Schoof friction law when $\xi << 1$ then $\tau_b = C^2 u_b^m$ and the friction law is in a Weertman sliding regime and when $\xi >> 1$ then $\tau_b = C^2 N/\zeta$ and the friction law is in an Iken sliding regime (C^2/ζ is the equivalent of $C_{\max}$ for Schoof).

The basal shear stress changes with respect to changes in effective pressure and basal sliding speed as given in Eq. (4.3).

$$d\tau_b = \frac{\partial \tau_b}{\partial u_b} du_b + \frac{\partial \tau_b}{\partial N} dN, \tag{4.3}$$

where $d\tau_b$ is an infinitesimal change in the basal shear stress, du_b is an infinitesimal change in the basal sliding speed, and dN is an infinitesimal change in the effective pressure. For the Schoof and hydrology-modified Schoof friction laws $\frac{\partial \tau_b}{\partial u_b}$ is given by Eq. (4.4), and for the Budd friction law it is given by Eq. (4.5).

$$\frac{\partial \tau_b}{\partial u_b} = \frac{m \tau_b}{u_b (1 + \xi)}. \tag{4.4}$$

$$\frac{\partial \tau_b}{\partial u_b} = \frac{m \tau_b}{u_b}. \tag{4.5}$$

The Budd friction law therefore always responds to changes in basal sliding speed as if it is in a Weertman sliding regime (assuming $m = 1/n$), whereas the Schoof and hydrology-modified Schoof friction laws behave in a Weertman sliding regime in the limit where ξ

goes to 0. In the limit where ξ goes to $+\infty$ the basal shear stress does not change with respect to changes in the basal sliding speed as is expected with an Iken sliding regime.

For the Schoof and hydrology-modified Schoof friction laws $\frac{\partial \tau_b}{\partial N}$ is given by Eq. (4.6) and for the Budd friction law it is given by Eq. (4.7).

$$\frac{\partial \tau_b}{\partial N} = \frac{\tau_b \xi}{N(1+\xi)}. \tag{4.6}$$

$$\frac{\partial \tau_b}{\partial N} = \frac{r\tau_b}{N}. \tag{4.7}$$

The Budd friction law always behaves as if it is in an Iken sliding regime (assuming $r = 1$), whereas the Schoof and hydrology-modified Schoof friction laws behave as if they are in an Iken sliding regime in the limit where ξ goes to $+\infty$. When ξ goes to 0 the basal shear stress has no dependence on the effective pressure as is expected in a Weertman sliding regime.

In the context of uncoupled or one-way coupled models where the effective pressure is held constant, the Budd friction law will produce identical results to the Weertman friction law given the same initial basal shear stress, as $\frac{\partial \tau_b}{\partial u_b}$ in Eq. (4.5) has no dependence on N. While these laws should properly capture the subglacial processes in a Weertman sliding regime with low velocity and high effective pressure, the basal shear stress will be oversensitive to changes in basal sliding speed in regions that are in an Iken sliding regime. Two-way coupling with the Budd friction law will mean that the basal shear stress will respond to changes in effective pressure as if it is in an Iken sliding regime everywhere. The subglacial processes captured by the model are no longer valid in a Weertman sliding regime as they were in the uncoupled/one-way coupled model, and the subglacial processes captured in an Iken sliding regime are not valid either, as the basal shear stress still responds to changes in basal sliding speed as if it is in a Weertman sliding regime. When two-way coupled, the Budd friction law will tend to underestimate friction when the system should be in a Weertman sliding regime and overestimate friction when the system should be in an Iken sliding regime. This is because when in a Weertman sliding regime a positive (negative) change in ice speed will cause the effective pressure to decrease (increase) and consequently lower (raise) the basal shear stress. Such underestimations in basal shear stress are responsible for the upstream migration of the Siple Coast ice stream onsets in CB. When in an Iken sliding regime a positive (negative) change in ice speed will raise

(lower) the basal shear stress where such a contribution should be nonexistent. However, such contributions from the ice speed in an Iken sliding regime should be negligible, as changes in ice speed should be small comparatively to changes in effective pressure in such regions ($\Delta u/u << \Delta N/N$), and the basal shear stress depends linearly on N but depends on u to the 1/3 power. In the Budd law, a change in fraction of flotation from 0.99 to 0.98 or vice versa will change the basal shear stress by a factor of two, something that would require a change in the ice speed by a factor of 8, which is unrealistic in fast flowing regions. Only when the starting ice speed is sufficiently low will the effects of the basal shear stress overestimation be observed. Such is the case in CB where the Kamb ice stream saw a hydrologic activation in the absence of an ice stream reactivation.

Even when uncoupled or one-way coupled, the Schoof and hydrology-modified Schoof friction laws will produce different results from both each other and the Budd friction law given the same initial basal shear stress, as a result of a spatially variable initial ξ. When ξ is small these laws will behave in the same manner as the Budd and Weertman laws, however, when ξ is large the basal shear stress will change very little with respect to changes in the basal sliding speed. If ξ is determined correctly then the Schoof and hydrology-modified Schoof friction laws will capture the correct subglacial processes in a Weertman sliding regime. In an Iken sliding regime there will not be much change in the basal shear stress when the effective pressure is held constant, which is a step up from the Budd law, but two-way coupling is required to capture the proper subglacial processes present in an Iken sliding regime. However, such discrepancy between the ice flow models with various friction laws was largely unobserved in this study due the high dependence of ice stream evolution on the ice stream onset, which had comparable values of ξ for both the Schoof and hydrology-modified Schoof friction laws.

The success of a regularized Coulomb friction law in capturing how the basal shear stress evolves in time is dependent on how it determines ξ. For the Schoof friction law, ξ is dependent on the choice of C_s, $C_{\max}$, and N, while u_b is given by the ice flow model and m is set equal to $1/n$ throughout the entire domain. C_s is often determined using inversion techniques to match simulated and observed ice speeds, $C_{\max}$ is often taken to be some constant between 0.18 and 0.84 throughout the entire domain, and N is usually taken from a subglacial hydrology model or parameterized. The choice to have a spatially constant $C_{\max}$ means that $C_{\max}$ may be underestimated (overestimated) in different parts of the domain, leading ξ to be smaller (larger) than it should be. Furthermore, where $C_{\max}$ is underestimated there may not be enough basal shear stress to match simulated to observed ice surface speeds. In regions where $C_{\max}$ is underestimated and ξ is overestimated the effective pressure can have a large impact on the sliding speed by the same reasoning that the two-way coupled Budd friction law will tend to underestimate the basal shear stress in

areas which should be in a Weertman sliding regime.

Compared to the Schoof friction law, the hydrology-modified Schoof friction law is able to more accurately predict the sliding regime of the glacier based on the degree of cavitation at the glacier bed. It follows the assumption that the hydrology sheet is in steady state, which will break down when there is a fast transition between Iken and Weertman sliding regimes. Not neglecting an evolving hydrology sheet, u_b/N^n is given by Eq. (4.8).

$$\frac{u_b}{N^n} = \frac{\ell_r}{h_r - h}\left(\frac{1}{N^n}\frac{\partial h}{\partial t} + \tilde{A}h\right). \tag{4.8}$$

If there is a transition from a Weertman (Iken) to an Iken (Weertman) sliding regime, ξ will be overestimated (underestimated) and the basal shear stress will be underestimated (overestimated) during the transition. In this sense, the hydrology-modified Schoof friction law will amplify transitions between Weertman and Iken sliding regimes.

In the hydrology-modified Schoof friction law it is C which is important for determining the basal shear stress in a Weertman sliding regime and C^2/ζ (the $C_{\max}$ equivalent), which is important for determining the basal shear stress in an Iken sliding regime. As a consequence of the ratio of C^2 and C^2/ζ being fixed in the hydrology-modified Schoof friction law, the initial sliding regime of the model affects the extent to which the basal shear stress can change in a transition between sliding regimes. This is to say that if one region has more friction in a Weertman sliding regime than another region in a Weertman sliding regime, than it will also have more friction when both regions are in Iken sliding regimes. This does not sound unreasonable, but C is ultimately supposed to be a proxy for the ratio of bedrock protrusion size and spacing (Weertman, 1957), and ζ/C^2 is supposed to be a proxy for the maximum upglacier slope of bedrock obstacles (Schoof, 2005), two ideas which exist independent of each other. This is a problem unique to the hydrology-modified Schoof friction law, as typical regularized Coulomb friction laws give the ability to chose C and $C_{\max}$ independent of each other while giving up the ability to have a sliding regime dependent on the degree of cavitation at the glacier bed in a spatially consistent fashion. In this study it was found that when using the hydrology-modified Schoof friction law with variable melt input, either the inability to choose both C and $C_{\max}$ or a value of ζ that was too small led to a failure to model ice stream activation. The overestimation of $C_{\max}$ in a Weertman-turned-Iken sliding regime led to a small change in ice speed despite a large change in the subglacial hydrologic system.

In order to choose both C and $C_{\max}$ and have a sliding regime uniformly dependent on u_b/N^n throughout the entire domain, a new form of friction law must be used. One such choice is given in Eq. (4.9).

$$\tau_b = C_{\max} N \left(\frac{\xi}{1+\xi} \right) + C^2 u_b^m \left(\frac{1}{1+\xi} \right), \quad \xi = \alpha \frac{u_b}{N^n}. \tag{4.9}$$

Here, α controls the degree of cavitation, which switches the system between Weertman and Iken sliding regimes. In the limit where $\xi \to 0$ the first term vanishes and the second term becomes $C^2 u_b^m$ as we want in a Weertman sliding regime. In the limit where $\xi \to +\infty$ the second term vanishes and the first term becomes $C_{\max} N$ as we want in an Iken sliding regime. The partial of the basal shear stress with respect to the effective pressure is given by Eq. (4.10) and the partial of the basal shear stress with respect to the ice speed is given by Eq. (4.11).

$$\frac{\partial \tau_b}{\partial N} = C_{\max} \left(\frac{\xi}{1+\xi} \right) \left(1 - \frac{n}{1+\xi} \right) + \frac{n C^2 u_b^m \xi}{N} \frac{1}{(1+\xi)^2}. \tag{4.10}$$

$$\frac{\partial \tau_b}{\partial u_b} = \frac{C_{\max} N}{u_b} \frac{\xi}{(1+\xi)^2} + C^2 u_b^{m-1} \frac{m + (m-1)\xi}{(1+\xi)^2}. \tag{4.11}$$

From these equations we can see that in the limit where $\xi \to 0$, the basal shear stress does not respond to changes in effective pressure and $\frac{\partial \tau_b}{\partial u_b} = m\tau_b / u_b$ as is expected in a Weertman sliding regime. In the limit where $\xi \to +\infty$ we see that the basal shear stress does not respond to changes in ice speed and $\frac{\partial \tau_b}{\partial N} = \tau_b / N = C_{\max}$ as is expected in an Iken sliding regime.

The friction law presented here has the ability for the user to chose both C and $C_{\max}$ as with the Schoof friction law, and has a spatially consistent cavitation-dependent sliding regime as the hydrology-modified Schoof friction law. Furthermore, the split up of the friction law into explicit Weertman and Iken sliding terms allows for easy evaluation of which process is more dominant in the model at any given time. Indeed, the friction law is a linear combination of Weertman and Iken sliding terms, with weighting coefficients that sum to one. Yet, choosing the correct value of both C and $C_{\max}$ simultaneously is a problem regardless of whether using this new friction law or the Schoof friction law. Without access to time series data where the ice sheet displays the full range of sliding regimes at every point in the domain, only C or $C_{\max}$ can be estimated. It is for this reason that we suggest in general the use of the hydrology-modified Schoof friction law,

with a possibly larger value of ζ. While the logic of holding the ratio of C^2 to $C_{\max}$ fixed is not well founded from an understanding of bedrock protrusions, it allows for the ability to estimate both C^2 and $C_{\max}$ together. Previous studies using the Schoof friction law (McArthur et al., 2023; Brondex et al., 2017, 2019) have held $C_{\max}$ constant at the expense of incorrectly determining the initial sliding regime of the glacier.

A current requirement to stabilize coupled subglacial hydrology and ice flow models is the use of an effective pressure cap. This cap is necessary to avoid unrealistically large ice speeds, which arise in areas with very low effective pressure. However, such a cap halts the ability for the effective pressure to alter the basal shear stress in a strong Iken sliding regime and limits the physics captured in our models. This problem can be addressed by adding a minimum friction term ($\tau_{\min}$) and removing the effective pressure cap in any of the friction laws. In the friction law presented above, such a term can be added within the Iken sliding term or as a seperate term. If $\tau_{\min}$ is added within the Iken sliding term then Eq. (4.10) and Eq. (4.11) become Eq. (4.12) and Eq. (4.13) respectively.

$$\frac{\partial \tau_b}{\partial N} = \left(\frac{\xi}{1+\xi}\right)\left(C_{\max} - \frac{n(\tau_{\min} + C_{\max}N)}{N(1+\xi)}\right) + \frac{nC^2 u_b^m \xi}{N}\frac{1}{(1+\xi)^2}. \tag{4.12}$$

$$\frac{\partial \tau_b}{\partial u_b} = \frac{\tau_{\min} + C_{\max}N}{u_b}\frac{\xi}{(1+\xi)^2} + C^2 u_b^{m-1}\frac{m+(m-1)\xi}{(1+\xi)^2}. \tag{4.13}$$

As $\xi \to 0$ we still find $\partial\tau_b/\partial N = 0$ and $\partial\tau_b/\partial u_b = m\tau_b/u_b$. As $\xi \to +\infty$ we find $\partial\tau_b/\partial N = C_{\max}$, and $\partial\tau_b/\partial u_b = 0$.

As two-way coupling of ice flow to subglacial hydrology models becomes more prevalent moving forwards, it is crucial that the glaciological modeling community addresses the shortcomings of the present implementation of friction in ice flow models discussed here. Validation of these friction laws may be performed by modeling past periods of changing ice motion and comparing against observations.

4.2.2 Subglacial conditions in the absence of two-way coupling

If modeling ice flow without any subglacial hydrological data, an effective pressure parameterization must be used in an effective pressure dependent friction law. Though no such parameterizations were examined in this work, they are frequently used in ice flow modeling (Åkesson et al., 2021; Yu et al., 2018) and the importance of the effective pressure and

the glacier sliding regime identified in this study warrants an analysis of how to implement these ideas in a computationally inexpensive manner. A common parameterization for N is to assume $N = \phi_0 = \rho_i g H + \rho_w g B$ (McArthur et al., 2023; Åkesson et al., 2021; Yu et al., 2018) or to assume $N = \phi_0$ for $B \leq 0$ and $N = p_i$ for $B > 0$ (Brondex et al., 2017, 2019). This latter parameterization will have low effective pressure close to the grounding line where the ice is close to the flotation criteria ($\phi_0 = 0$). With this parameterization, ice that is close to the grounding line will be in an Iken sliding regime and will transition to a Weertman sliding regime further inland. McArthur et al. (2023) proposed an empirical parameterization of effective pressure based on the idea that water pressurizes under thick ice. Such a parameterization is more likely to have Iken sliding regimes in topographic lows with thicker ice.

Given the importance that the sliding regime plays in the implementation of basal friction, it is constructive to parameterize the sliding regime, and as a consequence the effective pressure, when running an uncoupled ice flow model. In this way, it can be ensured that fast flowing regions of the domain are put into an Iken sliding regime and slow regions are put into a Weertman sliding regime. Such a parameterization may consider ξ as a function of u_b and τ_b, however, a concrete implementation of such a parameterization is beyond the scope of this work.

With all of these parameterizations for the effective pressure or sliding regime discussed so far, it is assumed that the effective pressure is to be held temporally constant so that the sliding regime only responds to changes in ice speed. However, the Brondex et al. (2017, 2019) parameterization and the McArthur et al. (2023) empirical parameterization can be implemented to account for the effects of an evolving ice sheet geometry, as they both have a dependence on the ice thickness. As shown in Section 3.3, changes in ice speed often have little impact on the sliding regime and the basal shear stress when in Iken sliding regimes and in the transition between Weertman and Iken sliding regimes. Therefore, the future implementation of effective pressure parameterizations in ice flow-only models should look to include temporal changes in the effective pressure due to an evolving ice sheet.

However, unless running simulations over centennial to millennial timescales, the ice thickness is unlikely to change on appreciable scales ($\Delta H / H << 1$) and consequently the evolving ice sheet will have little impact on the effective pressure parameterization. An effective pressure parameterization that has an explicit dependence on the basal sliding speed, which changes on shorter timescales than the ice sheet geometry is needed to better capture the effects of a two-way coupled subglacial hydrology and ice flow model. Such a parameterization should have a high flotation fraction when the ice is fast or when ice is thick, with thinner and slower ice going to some lower flotation fraction representative of an inactive subglacial hydrologic system.

To demonstrate how these concepts can be implemented in an effective pressure parameterization, we present a phenomenological effective pressure parameterization with explicit dependence on the basal sliding speed and the ice thickness. Working off similar principals to McArthur et al. (2023) we can assume that in an inactive subglacial hydrologic system there is a minimum flotation fraction f_0. The floation fraction (f) can then have values between f_0 and 1, determined by some function of the ice thickness and the basal sliding speed, $\psi(u_b, H)$. Such a parameterization of the flotation fraction would take the form of Eq. (4.14).

$$f(u_b, H) = f_0 + (1 - f_0)\psi(u_b, H). \tag{4.14}$$

Saturation terms, which go to 1 as H or u get large can be used to ensure that there is a large flotation fraction for thick ice and fast ice. Such saturation terms may take the form $H^r/(H_c^r + H^r)$ and $u_b^s/(u_c^s + u_b^s)$, where H_c is a constant ice thickness, u_b is a constant ice speed, and r and s are some exponents for the ice thickness and ice speed saturation terms, respectively. H_c and u_c control at what values of H and u_b, respectively, the subglacial hydrologic system becomes active and the flotation fraction transitions quickly to higher values. r and s control the rate of said transition. To ensure that thin fast ice and thick slow ice are both pressurized, we can describe ψ as a linear combination of the two saturation terms with weighting coefficients. When the ice is thick and slow the ice thickness saturation weight should be large, and when the ice is thin and fast the ice speed saturation weight should be large. Weighting coefficients that fit this description are given in Eq. (4.15) for the ice thickness and ice speed terms respectively.

$$\frac{(H/H_c)^r}{(H/H_c)^r + (u_b/u_c)^s}, \quad \frac{(u_b/u_c)^s}{(H/H_c)^r + (u_b/u_c)^s}. \tag{4.15}$$

These coefficients sum to 1, ensuring that $\psi \leq 1$ and $f \leq 1$. ψ is then given by Eq. (4.16).

$$\psi = \frac{1}{(H/H_c)^r + (u_b/u_c)^s} \left(\frac{(H/H_c)^{2r}}{1 + (H/H_c)^r} + \frac{(u_b/u_c)^{2s}}{1 + (u_b/u_c)^s} \right). \tag{4.16}$$

It follows that the effective pressure parameterization is given by $N = p_i(1 - f) = p_i(1 - f_0)(1 + \psi)$. Finding appropriate values for r, s, H_c, and u_c and testing the validity of such

a parameterization against two-way coupled models is beyond the scope of this work. Yet, the implementation of a temporally variable effective pressure parameterization with ice speed dependence in an ice flow-only friction law is a step towards better implementing subglacial conditions in ice flow-only models. It is however, not a substitute for two-way coupled models. While this parameterization will enhance the change in the basal shear stress caused by changes in ice motion, it will fail to capture the processes involved when changes in the effective pressure and ice speed counteract each other to alter the basal shear stress. Such processes exist in the coupled models where Ice Stream B initially slowed down while the effective pressure decreased, highlighting the importance of two-way coupled models.

Future work on testing effective pressure parameterizations should compare results against outputs from established subglacial hydrology models such as GlaDS and SHAKTI. Of note is that the parameterization presented here is likely only applicable to Antarctic glaciers. In Greenland large volumes of surface melt in the Boreal summer cause the subglacial system to change on timescales much faster than those of Antarctica. An effective pressure parameterization tailored towards Greenland would likely need to include a surface air temperature dependence.

4.2.3 The affect of vertical shear on friction

The SSA neglects vertical shear of ice, overestimating basal sliding speeds, particularly in Weertman sliding regimes and in ice stream onsets. Consequently, changes in basal shear stress with respect to changes in ice speed are likely overestimated in strong Weertman sliding regimes, where changes in ice motion are likely a result of changes in ice deformation, not basal sliding. This could overestimate changes in the basal shear stress when using the SSA compared to a full Stokes or higher order model. In ice stream onsets, where the transition from ice creep to basal sliding is made, the comparative changes in basal sliding are likely underestimated when using the SSA, which may underestimate changes in the basal shear stress. To remedy this, a parameterization for the basal sliding speed can be used in the friction law, to approximate the effects of vertical shear, and more accurately predict how changes in ice motion affect the basal shear stress.

Such a parameterization may be made by considering one dimensional ice flow with a constant ice thickness, surface, and bed, and a constant ice rigidity. A Dirichlet boundary condition can be applied to the ice surface so that ice surface speed (u_s) is given by the modeled ice speed, and a Neumann boundary condition can be applied to the glacier base, through the basal shear stress. We use a cartesian coordinate system so that ice moves in

the positive x direction with z being the vertical coordinate equal to 0 at the glacier base and H at the glacier surface. We assume ice flows only in the x direction, so that the full Stokes equations are reduced to Eq. (4.17) with boundary conditions given by Eq. (4.18). A schematic of the described system is given in Fig. (4.4).

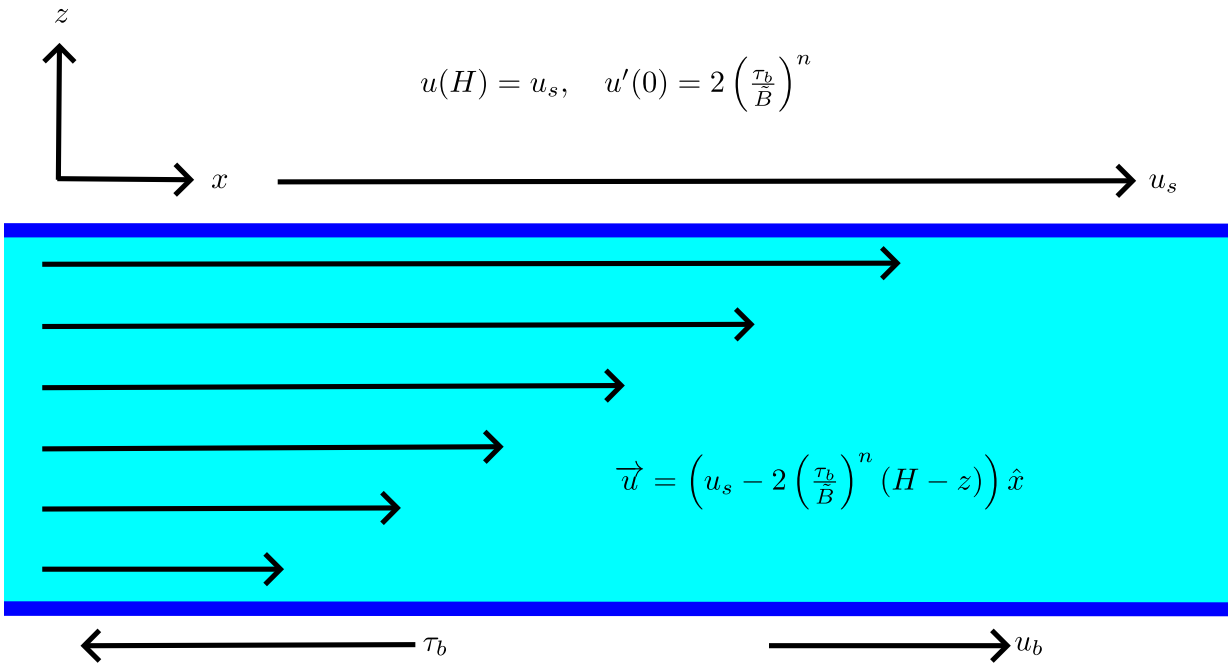

Figure 4.3: One dimensional ice flow with an imposed ice surface speed and basal shear stress.

$$\frac{\partial}{\partial z}\left(\mu\frac{\partial u}{\partial z}\right) = \frac{\partial}{\partial z}\left(\frac{\tilde{B}}{2^{1/n}}\left(\frac{\partial u}{\partial z}\right)^{\frac{1}{n}}\right) = 0. \tag{4.17}$$

$$u(H) = u_s, \quad u'(0) = 2\left(\frac{\tau_b}{\tilde{B}}\right)^n. \tag{4.18}$$

Eq. (4.17) reduces to $\frac{\partial^2 u}{\partial z^2} = 0$, giving $u = C_1 + C_2 z$. The coefficients C_1 and C_2 can be found by applying the boundary conditions to get Eq. (4.19).

$$u = u_s - 2\left(\frac{\tau_b}{\tilde{B}}\right)^n (H - z). \tag{4.19}$$

It follows that the basal sliding speed is given by Eq. (4.20)

$$u_b = u_s - 2H\left(\frac{\tau_b}{\tilde{B}}\right)^n. \tag{4.20}$$

Through this parameterization we can better estimate the basal sliding speed and its effect on the evolution of the basal shear stress. The assumptions made in this parameterization are only valid in areas with no surface or bed slope, meaning that the basal sliding speed predicted from this parameterization will be less accurate in areas with large gradients in ice surface and/or bed elevation. Care must be taken when using this parameterization to ensure that the basal sliding speed doesn't fall below zero in areas with high basal shear stress, thick ice, or low ice rigidity. Such regions should be capped with a minimum basal sliding speed. The cubic dependence on the ratio of the basal shear stress to the ice rigidity suggest that such a parameterization requires good estimates of both the basal shear stress and the ice rigidity over the grounded portion of the domain. Given the high dependence of the ice rigidity on temperature (Eq. 1.7), we suggest the use of a steady state thermal model to more accurately constrain ice rigidity before using this parameterization. This parameterization can be tested through a comparison with basal sliding speeds from full Stokes or higher order models.

4.3 Additional coupling components and feedback

In an attempt to understand various feedback mechanisms between the subglacial hydrological system and the ice sheet, and the relevance of these feedback mechanisms in two-way coupled models, models with additional coupling components were tested. In Section 4.3.1 we discuss the impact of variable melt on coupling and identify a negative feedback mechanism, which stabilizes the subglacial hydrologic system. In Section 4.3.2 we discuss the impact of subglacial lake geometry on the ice sheet and identify feedback mechanisms that control the lake depth. In Section 4.3.3 we discuss the stability of the fully coupled model and the negative feedback mechanism between ice geometry and basal melt that allowed for such stability.

4.3.1 Impact of variable melt on hydrologic stability

The melt calculated from Eq. (2.8) has contributions from melt from geothermal heat flux and melt from the production of frictional heat. For this study, the geothermal heat flux was kept temporally constant and the frictional heat was allowed to vary as the basal shear stress and ice speed evolved over the course of the simulation. Because the SSA depth averages ice speed, the ice speed used in computing frictional melting of ice will be consistently overestimated in regions where basal sliding is not the dominant factor controlling ice speed. This overestimation of the basal sliding speed will typically occur in Weertman sliding regimes where deformation is the dominant factor controlling ice motion (Cuffey and Paterson, 2010). Overestimation of the basal sliding speed combined with the everywhere-positive geothermal heat flux allows for a basal melt production that is generally larger than that from the InitMIP Antarctica control run final time step (Seroussi et al., 2019), which used a thermal model. Because of this, the effective pressure is generally lower and the sliding regime is generally more Iken in CM and FC compared to the constant melt coupled models. As a result, the basal shear stress and consequently the ice speed are more sensitive to an evolving hydrological system in CM and FC.

In the limit where the model is in a Weertman sliding regime, the frictional melt will be computed as $C^2 u_b^{m+1}$ with a 4/3 power dependence on the basal sliding speed assuming $n = 3$. In the limit where the model is in an Iken sliding regime the frictional melt will be computed as $\zeta N u_b / C^2$, with a linear dependence on the basal sliding speed. It can be shown that the power dependence of τ_b on u_b for a given ξ is given by $1 + m/(1 + \xi)$ making a sharp transition from 4/3 to 1 at $\xi \approx 1$, giving a slightly larger dependence of melt production on u_b for smaller values of ξ. However, we see from this that all regions of the domain can provide melt water production variability due to evolving basal shear stress and ice speed fields.

In a Weertman sliding regime there is limited feedback between basal melt production and ice speed. Faster (slower) ice will result in an increase (decrease) of melt in the subglacial hydrological system, however, the limited dependence of the basal shear stress on the effective pressure in a Weertman sliding regime means this won't further effect ice motion. The feedback mechanisms between basal melt production and ice speed in an effective pressure dependent sliding regime are more complicated to analyse. A positive (negative) perturbation in basal shear stress will increase (decrease) the amount of melt in the subglacial hydrological system, which will lower (raise) the effective pressure and basal shear stress. This is a negative feedback loop, which is depicted in Fig.(**??**a). However, it neglects the affect of the basal shear stress on ice motion and the affect of the ice motion on the melt water production. Given that the basal shear stress of ice stream onsets seems

to have a larger impact on ice stream motion than the basal shear stress within the ice stream (Section 3.3.1), we can assume that such a negative feedback loop may occur in an ice stream where there is an Iken sliding regime. However, as the sliding regime is progressively less Iken closer to the ice stream onset, this feedback becomes less strong. As ice speeds up (slows down) as the result of lowered (raised) basal shear stress, it will work to increase (decrease) the basal shear stress. In the Schoof and hydrology-modified Schoof friction laws the change in the basal shear stress in response to changes in effective pressure and basal sliding speed is given by Eq. (4.21).

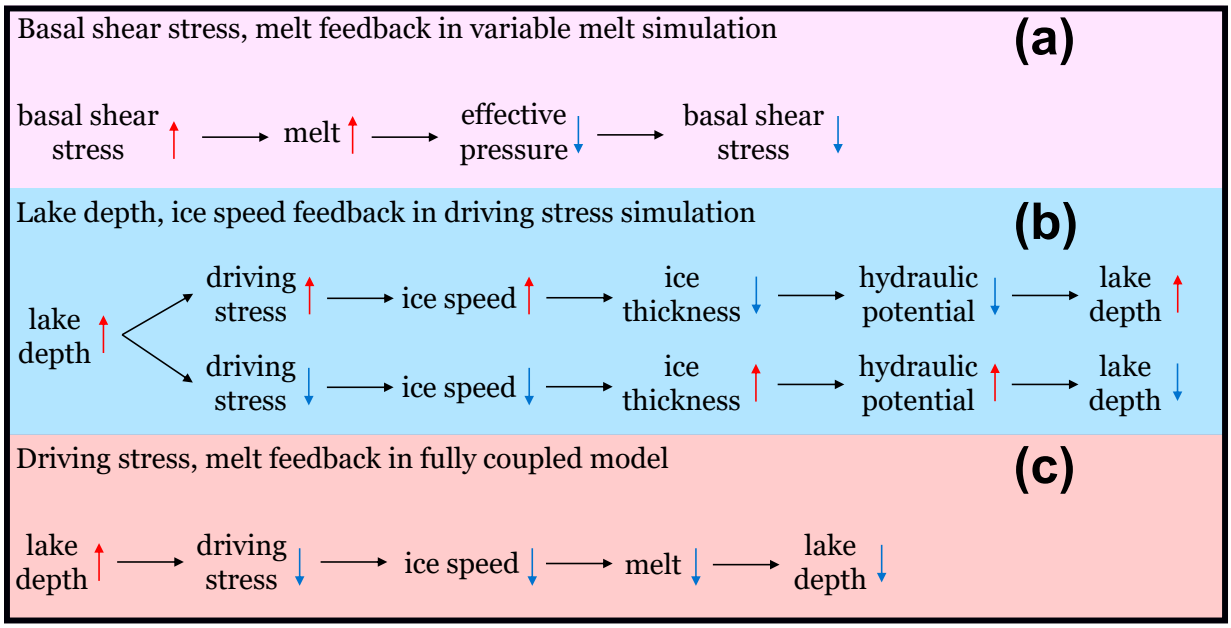

Figure 4.4: Feedback mechanisms from additional coupling components. (a) a feedback mechanism between subglacial lake depth and ice motion in CD; (b) a negative feedback mechanism between basal shear stress and effective pressure in CM and FC; (c) a feedback mechanism between glacier driving stress and subglacial lake depth in FC.

$$\frac{d\tau_b}{\tau_b} = \frac{m}{1+\xi}\frac{du_b}{u_b} + \frac{\xi}{1+\xi}\frac{dN}{N}. \tag{4.21}$$

The conditions for the change in ice speed to overtake the change in effective pressure with regards to their impact on the basal shear stress is then given by Eq. (4.22).

$$\left|\frac{du_b}{u_b}\right| > \frac{\xi}{m}\left|\frac{dN}{N}\right|. \tag{4.22}$$

Given that comparative changes in effective pressure are much greater than comparative changes in ice speed in fast flowing regions, we see that $\xi << 1$ for the contribution from changes in ice speed to overtake the contribution from changes in effective pressure in the evolution of the basal shear stress. The negative feedback mechanism, which stabilizes the basal shear stress and the effective pressure should then be present far into the ice stream onset. Indeed, this negative feedback loop is observed in CM and FC to stabilize the ice speed variability in ice streams D and E.

4.3.2 Impact of lake geometry on driving stress

The driving stress computed considering h_l is in general smaller than when only the surface slope is considered. Subglacial lakes occur in hydraulic potential lows, which are characterized by dips in surface slopes and bed slopes. Assuming a fraction of flotation f and negligible hydraology sheet thickness, the hydraulic potential is given by $\phi = \phi_0 - N = \rho_i g(fS + (\rho_{fw}/\rho_i - f)B)$, meaning that the surface slope plays a much larger role than the bed slope in the hydraulic potential gradient for typical values of f. It is therefore expected that lakes which occur in locations that have dips in the ice sheet surface will lower the glacier driving stress as they gain water. The fact that the ice surface plays such a large role in determining subglacial lake location to begin with explains why the driving stress is typically smaller when computed considering h_l – many lakes occur in locations with surface dips. Isolated areas of increased driving stress due to h_l occur where deep subglacial lakes can overcome the ice surface depression creating a local high in the ice surface, or where bed gradients are sufficiently large enough to create hydraulic potential lows.

A lake in equilibrium will satisfy $\partial h/\partial t = 0$, which implies that $N = 0$. To have $N = 0$ we require $h = (\phi - \phi_0)/(\rho_{fw} g)$, meaning that the lake equilibrium depth is determined by the hydraulic potential and the overburden hydraulic potential fields. Lakes which lower the glacier driving stress will slow and thicken ice, making ϕ_0 larger and consequently lowering the equilibrium lake depth. This creates a negative feedback loop, which acts to stabilize lake depth. Pattyn (2008) modeled ice flow over subglacial lakes in hydrostatic equilibrium with the overlying ice, and found that surface slope is the dominant factor controlling subglacial lake stability. They found that lakes with smaller surface slopes

tended to be more stable, which agrees with our findings here. When a filling lake increases glacier driving stress the ice speeds up and thins, lowering ϕ_0 and consequently raising the equilibrium lake depth. This positive feedback loop is stopped when downstream accelerating ice increases the cavity opening rate and water is transferred down glacier. Such processes were observed in CD where the deep lakes under Ice Stream B were deeper than in C up to their drainage, which left them shallower than in C. The positive feedback loop involved with the significant speedup of Ice Stream B in CD emphasizes the impact that subglacial lakes can have on the evolution of the ice sheet driving stress and advocates the incorporation of a hydrology layer component in the driving stress of two-way coupled models. The feedback loops identified here are depicted in Fig. (**??**b).

The incorporation of h_l into the driving stress in the SSA assumes that the ice surface is uplifted elastically by a distance h_l. In reality, the ice should experience flexure, which will smooth out the contribution of h_l to the surface slope of the glacier. In regions where adding water to a subglacial lake decreases the driving stress of the glacier, the driving stress will be underestimated leading to a smaller equilibrium depth of the lake. Likewise, in areas where adding water to a subglacial lake increases the driving stress of the glacier, the driving stress will be overestimated leading to a larger equilibrium lake depth. Therefore, the choice to exclude the effects of ice flexure will create lakes that are either too deep or too shallow. This may exaggerate systems where water may concentrate in a few key subglacial lakes, or where it tends to spread out amongst a large number of subglacial lakes. However, it does not invalidate the existence of the feedback mechanisms identified in this section.

The relationship between temporally variable basal conditions and ice surface elevation changes is complicated, and often involves an important dynamic thickening/thinning component. Sergienko et al. (2007) found that changes in subglacial lake depth will be less pronounced on the ice surface than at the ice base due to dynamic thickening/thinning of ice brought on by a changing driving stress. Sergienko et al. (2007) also found that changes in basal friction can have a much larger impact on ice motion than changing subglacial lake depth and are hence another important factor in ice surface elevation due to dynamic thickening/thinning. Sergienko and Hulbe (2011) found that patterns in basal friction had a large impact on the location of subglacial lakes, with sticky spots of high basal friction supplying melt water to fill a subglacial lake. Hydraulic potential lows would be generated upstream and downstream of the sticky spots due to spatial patterns in ice flow over the sticky spot. These would provide possible areas for subglacial lake formation. Including the impact of lake depth in ice surface elevation will help us better model these relationships between ice surface elevation, ice flow patterns, and subglacial conditions.

4.3.3 Melt/driving stress feedback

The fully coupled model, including variable melt input and driving stress contributions from subglacial lakes, showcases more stability than when each coupling process is implemented separately. This is a consequence of negative feedback mechanisms, which act to maintain a steady state system against small perturbations in the subglacial hydrological system and the ice sheet. When there is a subglacial lake that reduces upglacier driving stress when water is added, then a small increase (decrease) in lake depth will reduce (raise) upglacier driving stress, slowing down (speeding up) ice. This will decrease (increase) melt water production and drain (fill) the subglacial lake. This negative feedback loop (depicted in Fig. **??**c) acts with the negative feedback loop that keeps the basal shear stress and melt water production rate stable to further stabilize both the subglacial hydrological system and the ice sheet. When there is a subglacial lake that increases driving stress when water is added, then a small increase (decrease) in lake depth will speed up (slow down) ice, increasing (decreasing) melt water production and filling (draining) the lake. This is a positive feedback loop, however, it is unlikely to be observed given that the effective pressure has comparatively larger changes than ice speed and the basal shear stress has a similar dependency on ice speed and effective pressure in an Iken sliding regime. An increase/decrease in melt water production in the scenario described above will influence the effective pressure, which will likely have a larger impact on the melt water production rate than the change in ice speed from the perturbation in the driving stress. The change in melt production due to changes in ice speed and effective pressure is given by Eq. (4.23).

$$\frac{dm_s}{m_s} = \frac{1+m+\xi}{1+\xi}\frac{du_b}{u_b} + \frac{\xi}{1+\xi}\frac{dN}{N}. \tag{4.23}$$

The requirement for changes in ice speed to have a larger impact on melt water production than changes in effective pressure is then given by Eq. (4.24).

$$\left|\frac{du_b}{u_b}\right| > \frac{\xi}{1+m+\xi}\left|\frac{dN}{N}\right|. \tag{4.24}$$

By the same arguments of Section 4.3.1, the negative feedback mechanisms between the glacier driving stress and the melt water production should be present far into the ice stream onset.

4.4 Future GlaDS improvements

Here, we discuss the limitations of the GlaDS hydrology model and potential model improvements. In Section 4.4.1 we discuss the need for a temporally variable boundary condition in two-way coupled models with an evolving ice sheet. In Section 4.4.2 we discuss the equations governing lake evolution in GlaDS and how to better model lake depth. In Section 4.4.3 we discuss the process of cavity opening due to sliding and present a new cavity opening rate with the potential to incorporate the macro porous nature of linked cavity systems.

4.4.1 Boundary conditions

The GlaDS model domain is determined by finding the hydrologic catchment assuming overburden hydraulic potential ($\phi = \phi_0$) with ice sheet geometry from Morlighem et al. (2020). Because of this, the boundary condition for the initial GlaDS steady state run is taken to be zero Neumann flux, meaning that no water leaves or enters the domain. While this is suitable for constant ice sheet geometry and velocity, it does not hold up when an evolving ice sheet is considered as is the case in two-way coupled ice/hydrology modeling. In reality, altered ice sheet geometry and velocity may result in the inflow and outflow of water to the model domain, also known as water piracy. However, the model framework needs to have a temporally constant boundary condition meaning that water piracy at the domain boundary is not captured in the model. In this study, elements on the domain boundary which accumulated water above the typical bedrock bump height were recognized as areas where water should be exiting the domain and a Dirichlet boundary condition equal to the hydraulic potential at the most recent time step was applied in these regions; the rest of the boundary had zero Neumann flux. These changes in boundary conditions were implemented four times over the 90 year simulation at 2020, 2040, 2060, and 2080. In studies such as this, which run way two-way coupled ice/hydrology models over a portion of a larger ice body, the development of a temporally variable boundary condition should be considered. Though we recognize that the boundary conditions applied in this study may not accurately model the water content of the domain, the development of such a temporally variable boundary condition is beyond the scope of this work.

4.4.2 Lake equations

In GlaDS, the evolution of the hydrology sheet thickness is governed locally by opening due to sliding over a cavitated bed and closing due to ice creep. Eq. (2.4) is valid assuming that

$h \leq h_r$ and $N > 0$. When $h > h_r$ the opening term is set to 0, as there is no longer ice/bed contact so there is no opening due to sliding over cavitation. When $N < 0$ the closing rate term changes sign and acts as an opening rate term. Though hydraulic jacking where water lifts up ice is expected in areas where there is negative effective pressure (Röthlisberger and Iken, 1981), the viscous creep form of the closing turned opening rate when $N < 0$ does not have a physical basis. Rather, this term is kept active when $N < 0$ to function as an opening rate term so that subglacial lakes are allowed to form in the model.

Assuming a non steady state hydrologic system, when N first drops below zero the lake fill rate should be small, as $|N|$ is small. As N decreases the lake will fill faster as it has a cubic dependence on N (assuming $n = 3$). The lake fill rate will slow down and the lake will eventually reach equilibrium as N increases once more as a result of computing it at the water surface. The lake reaches equilibrium when $N = \phi_0 - \phi + \rho_{fw} g h = 0$ meaning that the equilibrium lake depth is dependent on the hydraulic potential field. This means that in a near steady state hydrologic system for an ice sheet geometry and ice velocity field which are slowly changing, lake depth will change as a result of changes in the hydraulic potential field and the ice geometry, as discussed in Section 4.3.2. Lake fill and drainage from such changes in ice geometry on scales larger than the subglacial lake width may raise and lower lake depth of multiple subglacial lakes simultaneously. These trends in lake depth variability created from a local evolution of lake depth as implemented in GlaDS may overwhelm possible trends in lake fill and drainage through subglacial lake hydrological networks such as those observed in the Siple Coast (Siegfried et al., 2016).

To generate subglacial lakes without relying on negative effective pressure, different equations/processes are needed to describe the evolution of the hydrology sheet thickness. Dow et al. (2018) included melt from dissipation of potential energy in the evolution of the hydrology sheet thickness, implemented in a fashion very similar to the channel equations. This allows the hydrology sheet to grow above the typical bedrock bump height – creating a subglacial lake – while maintaining a positive effective pressure. The inclusion of melt from dissipation of potential energy is a feature that is often associated with efficient drainage systems (Walder, 1986), with its inclusion in a linked cavity system often causing instability in the hydrology sheet (Werder et al., 2013). Indeed, if this process was included in the distributed sheet equations of this study, it is likely that much of the Siple Coast ice streams would experience such instability as they already have a hydrology sheet thickness that is close to the typical bedrock bump height.

Without the inclusion of melt from dissipation of potential energy, the GlaDS sheet equations were only created to consider the case where $h < h_r$. In this study we elected to use the negative effective pressure to turn the hydrology sheet closing rate into an opening rate and halted this process by computing the effective pressure at the water surface. In

reality such a negative effective pressure would cause hydraulic jacking and elastic uplift of ice, not ice creep, so the lake evolution equations are not physically valid and different equations describing the evolution of the hydrology sheet when $h > h_r$ may be considered. Lakes drain when the hydraulic potential low is filled, sending water away from the lake. The likely overestimation of lake depth variability in the models of this study compared to those observed by Carter et al. (2013) suggests that the hydraulic potential is underestimated for the given hydrology sheet thickness. Assuming a steady state lake, $\phi = \phi_0 + \rho_{fw} g h$, so ϕ has a linear dependence on h in this study. Future implementations of GlaDS may consider quadratic/cubic, or non polynomial relations between ϕ and h and forms of the opening rate that are unlike that of ice creep. The spatial nature of lake drainage, its larger impact on the ice sheet compared to the normal hydrologic system, and the need for GlaDS to have a local hydrology sheet evolution emphasize the difficulty of finding physics based lake equations. While this study has brought to light potential feedback mechanisms between lake dynamics and ice sheet dynamics, future modeling studies with a primary focus on subglacial lake evolution are needed to improve our implementation of subglacial lake processes in complex subglacial hydrology modeling moving forwards.

4.4.3 Cavity opening

In GlaDS, the hydrology sheet opening rate due to sliding over cavitation is given by $u_b(h_r - h)/\ell_r$ when $h < h_r$. This form of cavity opening rate was adopted by SHAKTI (Sommers et al., 2018), while Schoof (2010) used a cavity opening rate $h_r u_b$ (the dimensions are different since Schoof was considering a conduit). Neither Werder et al. (2013) or Schoof (2010) provide an explanation of their choice of cavity opening rate, something we wish to investigate here.

Considering a system of linked cavities in one dimension with bedrock bump heights h_r and spacing ℓ_r, then at each bump the cavity will close at a rate $u_b h_{\min}$ on the stoss side of the bump, where $h_{\min}$ is the hydrology sheet thickness on the stoss side of the bump; and open at a rate $u_b h_r$ on the lee side of the bump (Fig. 4.5a). Averaging over the cavity spacing, the hydrology sheet opening rate becomes $u_b(h_r - h_{\min})/\ell_r$. Over the length of the cavity the hydrology sheet thickness gradually decreases from h_r to $h_{\min}$ as the cavity closes due to viscous creep of ice. Assuming a constant rate of ice creep, the average hydrology sheet within the cavity (h) should be related to h_r and $h_{\min}$ by $h = (h_r + h_{\min})/2$ for $h_{\min} > 0$ (Fig. 4.5a). The cavity opening rate in terms of the hydrology sheet thickness should then be given by Eq. (4.25).

$$\omega_s = \begin{cases} u_b h_r/\ell_r & h < h_r/2 \\ 2u_b(h_r - h)/\ell_r & h_r/2 \leq h \leq h_r \\ 0 & h > h_r \end{cases}. \tag{4.25}$$

When $h < h_r/2$ a negative $h_{\min}$ is nonphysical and there is no closure on the stoss side of bedrock obstacles (Fig. 4.5b). For $h \geq h_r/2$ this is twice the cavity opening rate currently implemented in GlaDS, and for $h < h_r/2$ this is between one and two times the cavity opening rate implemented in GlaDS. For $h < h_r/2$ closure due to creep would only occur along a length $2h\ell_r/h_r$ so the creep closure rate will need to be multiplied by a factor $2h/h_r$ when $h < h_r/2$. If the hydrology sheet opening rate was changed to the above formulation, the overall larger hydrology sheet opening rate for a given hydrology sheet thickness should work to reduce the ability of GlaDS to store water in the distributed sheet system assuming the same effective pressure field. This can be remedied to match better with our current sheet opening implementation through tuning the sheet conductivity. Despite the comparatively smaller opening rate for smaller cavities in Eq. (4.25), the cavity closing rate is also comparatively smaller, meaning that with tuning of the sheet conductivity Eq. (4.25) should produce very similar results to Eq. (2.5).

Eq. (4.25) still fails to account for the macro scale porosity of the linked cavity system, implying that bedrock bumps are infinitesimally small. Assuming a porosity λ, the hydrology sheet can be areally averaged so that the average hydrology sheet thickness is related to the average hydrology sheet thickness in the cavities ($\tilde{h}$) as $h = \lambda\tilde{h}$. The cavity opening rate written in terms of the hydrology sheet thickness would then be given by Eq. (4.26), and the cavity closing rate for $h < h_r\lambda/2$ will be multiplied by a factor $2h\ell_r/(h_r\lambda)$.

$$\omega_s = \begin{cases} u_b h_r/\ell_r & h < h_r\lambda/2 \\ 2u_b(h_r - h/\lambda)/\ell_r & h_r\lambda/2 \leq h \leq h_r\lambda \\ 0 & h > h_r\lambda \end{cases}. \tag{4.26}$$

Care must be taken with the inclusion of porosity. After $h > h_r\lambda$ the hydrology sheet should be flooded above the bedrock protrusions and porosity will no longer be a factor. This will affect the hydrology layer thickness, which will be computed as $h_l = h - h_r\lambda$ for $h > h_r\lambda$.

Possible testing of Eq. (4.25) and Eq. (4.26) may be done on synthetic domains against Eq. (2.5). Other potential cavity opening equations should be tested in a similar manner.

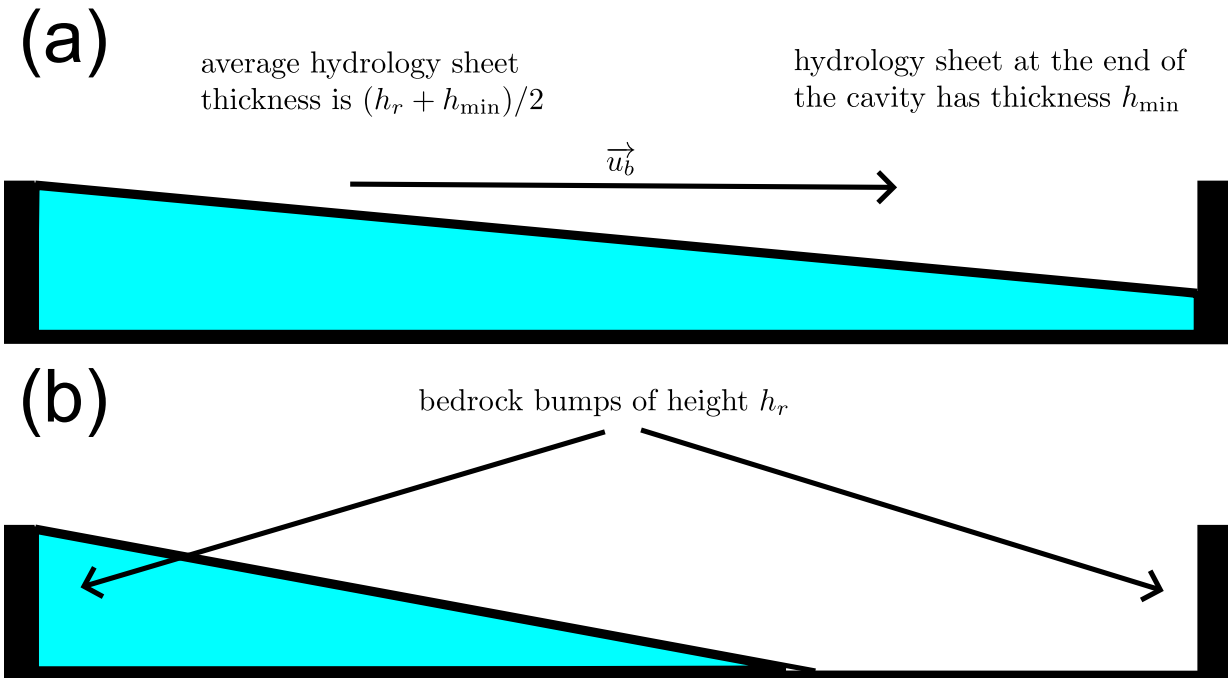

Figure 4.5: Cavity opening schematic. (a) a cavity with $h > h_r/2$; (b) a cavity with $h < h_r/2$.

Chapter 5

Conclusions

5.1 Project overview and key findings

The goal of this study was to identify Antarctic feedback mechanisms between the subglacial hydrological system and the ice sheet. The importance of the complex relationship between subglacial hydrology and ice dynamics has long been understood (Budd et al., 1979). However, Antarctic ice dynamics modeling to date has largely ignored the impacts of an evolving subglacial hydrologic system. Studies which have included a subglacial hydrologic component in ice flow modeling have done so using simplified subglacial hydrology models, not the recently developed two-dimensional subglacial hydrology models with both inefficient and efficient drainage components (Werder et al., 2013; Sommers et al., 2018). To more accurately understand the past, present, and future of the Antarctic Ice Sheet and how it relates to the larger climate system, two-way coupling between subglacial hydrology and ice flow models is necessary.

This study assesses the importance of incorporation of subglacial hydrologic processes in ice flow modeling through subglacial hydrology and ice flow modeling of the Ross Sea subglacial hydrologic catchment. GlaDS implemented in ISSM was used as the subglacial hydrology model and the SSA along with a mass transport model was used as the ice flow model. Friction was implemented in the ice flow model using three different effective pressure dependent friction laws. First, the Budd friction law, which is a power law that has a linear dependence on effective pressure. Second the Schoof friction law, and third, a form of the Schoof friction law that we modified to have a sliding regime that is spatially consistent with the degree of cavitation at the glacier bed – that we refer to as the hydrology-modified Schoof friction law. The Schoof and hydrology-modified Schoof

friction laws are regularized Coulomb friction laws, which transition continuously between Weertman (ice motion due to regelation and enhanced creep) and Iken (basal motion due to slip over the glacier bed) sliding regimes based on the basal sliding speed and the effective pressure. Steady state hydrology models were run with varying sheet conductivity and melt inputs. Transient ice flow and two-way coupled hydrology/ice flow models were run from years 2010 to 2100 with an SSP585 surface mass balance forcing scenario. The two-way coupling involved using the effective pressure from GlaDS in the friction law of the ice flow model and using the ice speed from the ice flow model in the cavity opening rate in GlaDS. On top of the standard two-way coupling we tested two additional coupling components; first we took the ice speed from the ice flow model and used it to compute frictional melting of ice in GlaDS and second we took the hydrology sheet thickness from GlaDS and used it to alter the driving stress of the ice flow model. Finally, a model with all coupling components was run.

The subglacial hydrological outputs from the GlaDS and coupled models suggest a soft sediment subglacial hydrological system in the Siple Coast ice streams. The hydrology sheet thickness was close to the typical bedrock bump height, which may be indicative of a water saturated till layer. R-channels formed within the ice streams, but the channel system was somewhat tortuous as opposed to the arborescent system normally associated with channelized drainage in alpine and Greenland glaciers (Shreve, 1972; Nienow et al., 2017). This may be a consequence of the low surface and bed slopes of the Siple Coast ice streams failing to create large enough hydraulic potential gradients for arborescent channel systems to form. Given that the hydrology sheet under the ice streams is suggestive of a water saturated till layer, which is consistent with the idea that the sediment under the Siple Coast ice streams is soft till (Blankenship et al., 1986; Engelhardt et al., 1990), R-channels may not be the primary source of efficient drainage under these ice streams. Sediment canals incised in the sediment underlying the glacier may dominate these regions, which agrees with the conclusions of Carter et al. (2017). Subglacial lakes formed in the GlaDS and coupled models underneath all Siple Coast ice streams except Ice Stream A, in the Byrd trough, and in the interior of the West Antarctic Ice Sheet upstream of Ice Stream B. A few of the subglacial lakes under ice streams B and E matched with observed subglacial lake locations (Livingstone et al., 2022). However, there were many modeled subglacial lake locations that have not yet been observed and many observed subglacial lakes that did not show up in the models. It is likely that the unmodeled lakes are a result of errors in bed and surface topography data from Morlighem et al. (2020), which fail to account for the existence of large subglacial water layers. Modeled lakes that are yet to be observed should be considered in future subglacial lake observation studies.

It was found that the ice stream onset had a large control over the ice stream dynamics.

The basal shear stress in the ice stream onsets changed primarily due to an evolving effective pressure field as opposed to changes in ice speed. The coupled models therefore produced vastly different ice stream behaviour than the ice flow models, which behaved similarly despite the use of various friction laws. The sliding regime of the Schoof and hydrology-modified Schoof friction laws had a large impact on ice flow. Ice stream onsets that had sliding regimes that were modeled as more Iken had larger responses to changes in effective pressure than sliding regimes that were modeled as more Weertman. The spatially constant estimate of Iken's bound in the Schoof friction law led to ice streams that were modeled to be strongly Weertman and a Byrd Glacier side wall that was modeled to be more Iken, creating large ice speedup episodes of the Byrd Glacier. The coupled model with the Budd friction law was shown to have unrealistic ice speedup upglacier of the Siple Coast ice streams, as a result of the basal shear stress responding to changes in effective pressure as if it is in an Iken sliding regime throughout the entire domain. The Kamb Ice Stream became hydrologically activated in the coupled run with the Budd friction law, but did not speed up as a result of large upglacier friction and the basal shear stress responding to changes in ice speed as if it is everywhere in a Weertman sliding regime. A similar hydrologic activation without an ice speedup occurred upglacier of Ice Stream A in the coupled model with variable melt as a result of an overestimation of Iken's bound.

Through the variety of two-way coupled simulations including the simulations with additional coupling components, a number of ice/hydrology feedback mechanisms were identified. It was found that models with faster ice streams had generally higher effective pressure as a result of increased cavity opening, suggesting the existence of a negative feedback mechanism between ice speed and effective pressure. However, when changes in ice speed and effective pressure were rapid this feedback mechanism broke down. In those cases faster ice was accompanied by lower effective pressure, suggesting a positive feedback loop where pressurized water speeds up ice, which further pressurizes water as a result of dynamic thinning emphasizing hydraulic potential lows. A negative feedback mechanism was identified in the variable melt simulations, where the variable melt allowed for the basal shear stress and effective pressure fields to stabilize each other. In the simulation with the inclusion of lake geometry in the driving stress computation two feedback mechanisms were identified, which control the depth of subglacial lakes. Where increases in subglacial lake depth decrease upglacier driving stress, a negative feedback mechanism was identified, which lowered the equilibrium lake depth and slowed ice. Where increases in lake depth increase driving stress, a positive feedback mechanism was identified, which raised the equilibrium lake depth and sped up ice. Finally, in the model with all the coupling components a negative feedback mechanism was identified between the subglacial lake depth and melt water production, which stabilized lake depth.

5.2 Next steps

In light of the findings of this study and the methodological problems that arose from implementing ideas novel to the field, there is a lot of future work to be done to better represent the role of subglacial processes in ice flow models.

The identification of the importance the sliding regime plays in a regularized Coulomb friction law, and the necessity to independently choose friction parameters representative of ice flow in Iken and Weertman sliding regimes to model the activation and deactivation of fast flowing regions suggests the need for a new friction law. A phenomenological friction law with a cavitation dependent sliding regime and independent Iken and Weertman sliding parameters was proposed in this study. However, it is not a unique choice and its validity has not yet been tested. Furthermore, geophysical observations of the ice sheet in both Iken and Weertman sliding regimes over the entire ice sheet are necessary to properly constrain the Weertman and Iken sliding parameters of this hypothetical new friction law.

Given that the basal shear stress is much more sensitive to changes in effective pressure in fast flowing regions, two-way coupled ice flow/subglacial hydrology models that have an evolving effective pressure field incorporate the physics of the subglacial system much better than ice flow-only models. However, it can be difficult and computationally more expensive to couple a complex subglacial hydrology model to an ice flow model. In the absence of a subglacial hydrology model, a temporally variable parameterization of the effective pressure will improve the subglacial physics captured by ice flow-only models. One such parameterization with dependence on the basal sliding speed and ice thickness was proposed in this study, but it lacks validity testing. Work on developing an improved effective pressure parameterization can greatly enhance the outputs from large/computationally expensive ice sheet models moving forwards.

The dependence of the basal shear stress and the melt from frictional heat on the basal sliding speed warrants a parameterization of the basal sliding speed to be used in two dimensional depth averaged ice flow models such as the SSA. A physics based paramterization was proposed considering the one dimensional flow of a glacier with constant surface and bed elevation subject to a Dirichlet boundary condition of the ice surface speed at the glacier surface and a Cauchy boundary condition of the basal shear stress at the ice base. The parameterization had a cubic dependence on the ratio of the basal shear stress to the ice rigidity, meaning it should be used only when both the ice rigidity and the basal shear stress can be constrained over the grounded portion of the domain. This suggests the use of a thermal model to better constrain ice rigidity.

The GlaDS domain is typically taken to be a subglacial hydrologic catchment, assuming

overburden hydraulic potential. The obvious boundary condition is then to apply zero Neumann flux so that no water leaves or enters the domain. If applying constant ice geometry and ice speed as is the case when GlaDS is run on its own, then this application of boundary condition is not an issue. However, in an evolving ice sheet, this boundary condition fails to capture the effects of water piracy, sometimes pooling water near the domain boundary and releasing it in floods further into the model run. This study updated the GlaDS boundary conditions four times over the 90 year simulation to account for the affects of water piracy, but future GlaDS modeling on the catchment scale should consider the development of a temporally variable boundary condition.

The local evolution of the hydrology sheet thickness in GlaDS creates subglacial lakes with equilibrium lake depths that rise and fall with changes in the hydraulic potential and overburden hydraulic potential fields. Changes in such fields on length scales that are longer than the width of subglacial lakes can raise and lower lake depth of multiple subglacial lakes simultaneously, when they should be hydraulically linked with one lake draining into another. The solution to better representing lake dynamics in GlaDS is so far unclear, and is an important area of research moving forwards, given the relevant feedback mechanisms between subglacial lakes and the ice sheet. The lake equations used in this study produced hydraulic potentials that varied linearly with the hydrology sheet thickness, which seems to have led to the overestimation of lake depths. A tentative step forwards would be to consider equations with a stronger dependence on the hydrology sheet thickness, potentially quadratic or cubic.

The hydrology sheet opening rate in GlaDS and SHAKTI uses a heuristic relation describing sliding over a linked cavity system. In an attempt to better describe this opening rate, we considered sliding with constant speed over bedrock obstacles with uniform height and spacing, with a spatially constant creep closure. We arrived at a similar equation for the opening rate that is one to two times greater than that currently implemented in GlaDS. We adapted our new opening rate to include the effects of a macro porous linked cavity system. The assumptions behind our new opening rate are simplistic, but given the heuristic nature of the opening rate currently implemented in complex subglacial hydrology models an analysis of how different cavity opening equations effects the subglacial hydrologic system is an area worthy of future work.

The work presented here is critical for the future implementation of subglacial hydrologic processes in ice flow modeling. The importance of the sliding regime was identified and a regularized Coulomb friction law with a spatially consistent dependence of the sliding regime on the degree of cavitation at the glacier bed was developed. The inclusion of melt input from frictional melting of ice and the subglacial lake geometry altering the glacier driving stress provided additional feedback mechanisms, which do not occur with

standard two-way coupled ice/hydrology modeling. The identification of model shortcomings and the suggestion of potential model improvements will shape the way we approach ice/hydrology modeling moving forwards.

References

Adusumilli, S., Fricker, H. A., Medley, B., Padman, L., and Siegfried, M. (2020). Interannual variations in meltwater input to the southern ocean from antarctic ice shelves. *Nature Geoscience*, 13(9):616–620.

Åkesson, H., Morlighem, M., O'Regan, M., and Jakobsson, M. (2021). Future projections of petermann glacier under ocean warming depend strongly on friction law. *Journal of Geophysical Research: Earth Surface*, 126(6):e2020JF005921.

Anderson, R. S., Anderson, S. P., MacGregor, K. R., Waddington, E. D., O'Neel, S., Riihimaki, C. A., and Loso, M. G. (2004). Strong feedbacks between hydrology and sliding of a small alpine glacier. *Journal of Geophysical Research: Earth Surface*, 109(F03005):1–17.

Arnold, N. and Sharp, M. (2002). Flow variability in the scandinavian ice sheet: modelling the coupling between ice sheet flow and hydrology. *Quaternary Science Reviews*, 21(4):485–502.

Blankenship, D. D., Bentley, C. R., Rooney, S. T., and Alley, R. B. (1986). Seismic measurements reveal a saturated porous layer beneath an active antarctic ice stream. *Nature*, 322(6074):54–57.

Bougamont, M., Christoffersen, P., Price, S. F., Fricker, H. A., Tulaczyk, S., and Carter, S. P. (2015). Reactivation of kamb ice stream tributaries triggers century-scale reorganization of siple coast ice flow in west antarctica. *Geophysical Research Letters*, 42(20):8471–8480.

Brondex, J., Gagliardini, O., Gillet-Chaulet, F., and Durand, G. (2017). Sensitivity of grounding line dynamics to the choice of the friction law. *Journal of Glaciology*, 63(241):854–866.

Brondex, J., Gillet-Chaulet, F., and Gagliardini, O. (2019). Sensitivity of centennial mass loss projections of the Amundsen basin to the friction law. *The Cryosphere*, 13(1):177–195.

Budd, W. F., Keage, P. L., and Blundy, N. A. (1979). Empirical studies of ice sliding. *Journal of Glaciology*, 23(89):157–170.

Carter, S., Fricker, H., and Siegfried, M. (2013). Evidence of rapid subglacial water piracy under whillans ice stream, west antarctica. *Journal of Glaciology*, 59(218):1147–1162.

Carter, S. P., Fricker, H. A., and Siegfried, M. R. (2017). Antarctic subglacial lakes drain through sediment-floored canals: theory and model testing on real and idealized domains. *The Cryosphere*, 11(1):381–405.

Catania, G., Hulbe, C., Conway, H., Scambos, T., and Raymond, C. (2012). Variability in the mass flux of the ross ice streams, west antarctica, over the last millennium. *Journal of Glaciology*, 58(210):741–752.

Chu, V. W. (2014). Greenland ice sheet hydrology: A review. *Progress in Physical Geography*, 38(1):19–54.

Cook, S. J., Christoffersen, P., and Todd, J. (2022). A fully-coupled 3D model of a large Greenlandic outlet glacier with evolving subglacial hydrology, frontal plume melting and calving. *Journal of Glaciology*, 68(269):486–502.

Cuffey, K. and Paterson, W. (2010). *The Physics of Glaciers*. Elsevier Science.

de Fleurian, B., Werder, M. A., Beyer, S., Brinkerhoff, D. J., Delaney, I., Dow, C. F., Downs, J., Gagliardini, O., Hoffman, M. J., Hooke, R. L., et al. (2018). Shmip the subglacial hydrology model intercomparison project. *Journal of Glaciology*, 64(248):897–916.

Dow, C., McCormack, F., Young, D., Greenbaum, J., Roberts, J., and Blankenship, D. (2020). Totten Glacier subglacial hydrology determined from geophysics and modeling. *Earth and Planetary Science Letters*, 531:115961.

Dow, C., Werder, M., Babonis, G., Nowicki, S., Walker, R., Csatho, B., Morlighem, M., Dow, C. F., Werder, M. A., Babonis, G., Nowicki, S., Walker, R. T., Csatho, B., and Morlighem, M. (2018). Dynamics of Active Subglacial lakes in Recovery Ice Stream. *Journal of Geophysical Research*, 123(4):837–850.

Dow, C. F. (2022). The role of subglacial hydrology in antarctic ice sheet dynamics and stability: a modelling perspective. *Annals of Glaciology*, 63(87-89):49–54.

Dow, C. F., Ross, N., Jeofry, H., Siu, K., and Siegert, M. J. (2022). Antarctic basal environment shaped by high-pressure flow through a subglacial river system. *Nature Geoscience*, 15(11):892–898.

Ehrenfeucht, S., Morlighem, M., Rignot, E., Dow, C. F., and Mouginot, J. (2023). Seasonal acceleration of petermann glacier, greenland, from changes in subglacial hydrology. *Geophysical Research Letters*, 50(1):e2022GL098009.

Elsworth, C. W. and Suckale, J. (2016). Rapid ice flow rearrangement induced by subglacial drainage in west antarctica. *Geophysical Research Letters*, 43(22):11,697–11,707.

Engelhardt, H., Humphrey, N., Kamb, B., and Fahnestock, M. (1990). Physical conditions at the base of a fast moving antarctic ice stream. *Science*, 248(4951):57–59.

Flowers, G. E. (2015). Modelling water flow under glaciers and ice sheets. *Proceedings of the Royal Society A: Mathematical, Physical and Engineering Sciences*, 471(2176):20140907.

Flowers, G. E., Björnsson, H., Pálsson, F., and Clarke, G. K. C. (2004). A coupled sheet-conduit mechanism for jökulhlaup propagation. *Geophysical Research Letters*, 31(5):L05401.

Flowers, G. E. and Clarke, G. K. C. (2002). A multicomponent coupled model of glacier hydrology 1. theory and synthetic examples. *Journal of Geophysical Research: Solid Earth*, 107(B11):ECV 9–1–ECV 9–17.

Fountain, A. G. and Walder, J. S. (1998). Water flow through temperate glaciers. *Reviews of Geophysics*, 36(3):299–328.

Fowler, A. C. (1987). A theory of glacier surges. *Journal of Geophysical Research: Solid Earth*, 92(B9):9111–9120.

Frederikse, T., Landerer, F., Caron, L., Adhikari, S., Parkes, D., Humphrey, V. W., Dangendorf, S., Hogarth, P., Zanna, L., Cheng, L., and Wu, Y.-H. (2020). The causes of sea-level rise since 1900. *Nature*, 584(7821):393–397.

Gagliardini, O., Cohen, D., Råback, P., and Zwinger, T. (2007). Finite-element modeling of subglacial cavities and related friction law. *Journal of Geophysical Research*, 112(F2):F02027.

Gilbert, J. C. and Lemarechal, C. (1989). Some numerical experiments with variable-storage quasi-newton algorithms. *Mathematical Programming*, 45(3):407–435.

Glen, J. W. and Perutz, M. F. (1955). The creep of polycrystalline ice. *Proceedings of the Royal Society of London. Series A. Mathematical and Physical Sciences*, 228(1175):519–538.

Hansen, P. C. (2001). The L-curve and its use in the numerical treatment of inverse problems. In *Computational Inverse Problems in Electrocardiology*, number 5 in Advances in Computational Bioengineering, pages 119–142. WIT Press, Southampton.

Hooke, R. L. (2019). *Water flow in and under glaciers: Geomorphic implications*, page 199–255. Cambridge University Press.

Hughes, T., Sargent, A., and Fastook, J. (2011). Ice-bed coupling beneath and beyond ice streams: Byrd glacier, antarctica. *Journal of Geophysical Research: Earth Surface*, 116(F3):F03005.

Iken, A. (1981). The effect of the subglacial water pressure on the sliding velocity of a glacier in an idealized numerical model. *Journal of Glaciology*, 27(97):407–421.

Iken, A. and Bindschadler, R. A. (1986). Combined measurments of subglacial water-pressure and surface velocity of Findelengletsher, Switzerland. *Journal of Glaciology*, 32(110):101–119.

Joughin, I., Das, S. B., King, M. A., Smith, B. E., Howat, I. M., and Moon, T. (2008). Seasonal speedup along the western flank of the greenland ice sheet. *Science*, 320(5877):781–783.

Kamb, B. (1987). Glacier surge mechanism based on linked cavity configuration of the basal water conduit system. *Journal of Geophysical Research: Solid Earth*, 92(B9):9083–9100.

Kapitsa, A. P., Ridley, J. K., Robin, G. d. Q., Siegert, M. J., and Zotikov, I. A. (1996). A large deep freshwater lake beneath the ice of central east antarctica. *Nature*, 381(6584):684–684.

Kessler, M. A. and Anderson, R. S. (2004). Testing a numerical glacial hydrological model using spring speed-up events and outburst floods. *Geophysical Research Letters*, 31(L18):L18503.

Khan, S. A., Choi, Y., Morlighem, M., Rignot, E., Helm, V., Humbert, A., Mouginot, J., Millan, R., Kjær, K. H., and Bjørk, A. A. (2022). Extensive inland thinning and speed-up of northeast greenland ice stream. *Nature*, 611(7937):727–732.

Kim, B.-H., Lee, C.-K., Seo, K.-W., Lee, W. S., and Scambos, T. (2016). Active subglacial lakes and channelized water flow beneath the kamb ice stream. *The Cryosphere*, 10(6):2971–2980.

Kittel, C. (2021). Kittel et al. (2021), The Cryosphere : MAR and ESMs data.

Kittel, C., Amory, C., Agosta, C., Jourdain, N. C., Hofer, S., Delhasse, A., Doutreloup, S., Huot, P.-V., Lang, C., Fichefet, T., and Fettweis, X. (2021). Diverging future surface mass balance between the antarctic ice shelves and grounded ice sheet. *The Cryosphere*, 15(3):1215–1236.

Larour, E., Seroussi, H., Morlighem, M., and Rignot, E. (2012). Continental scale, high order, high spatial resolution, ice sheet modeling using the ice sheet system model (issm). *Journal of Geophysical Research: Earth Surface*, 117(F1):F01022.

Livingstone, S. J., Li, Y., Rutishauser, A., Sanderson, R. J., Winter, K., Mikucki, J. A., Björnsson, H., Bowling, J. S., Chu, W., Dow, C. F., Fricker, H. A., McMillan, M., Ng, F. S. L., Ross, N., Siegert, M. J., Siegfried, M., and Sole, A. J. (2022). Subglacial lakes and their changing role in a warming climate. *Nature Reviews. Earth & Environment*, 3(2):106–124.

MacAyeal, D. R. (1989). Large-scale ice flow over a viscous basal sediment: Theory and application to ice stream b, antarctica. *Journal of Geophysical Research*, 94(B4):4071–4087.

McArthur, K., McCormack, F. S., and Dow, C. F. (2023). Basal conditions of denman glacier from glacier hydrology and ice dynamics modeling. *The Cryosphere*, 17(11):4705–4727.

McCormack, F. S., Roberts, J. L., Kulessa, B., Aitken, A., Dow, C. F., Bird, L., Galton-Fenzi, B. K., Hochmuth, K., Jones, R. S., Mackintosh, A. N., and McArthur, K. (2023). Assessing the potential for ice flow piracy between the totten and vanderford glaciers, east antarctica. *The Cryosphere*, 17(11):4549–4569.

Morlighem, M., Rignot, E., Binder, T., Blankenship, D., Drews, R., Eagles, G., Eisen, O., Ferraccioli, F., Forsberg, R., Fretwell, P., et al. (2020). Deep glacial troughs and stabilizing ridges unveiled beneath the margins of the Antarctic ice sheet. *Nature Geoscience*, 13:132–137.

Mouginot, J., Rignot, E., Scheuchl, B., and Millan, R. (2017). Comprehensive annual ice sheet velocity mapping using landsat-8, sentinel-1, and radarsat-2 data. *Remote Sensing*, 9(4):364.

Mouginot, J., Scheuchl, B., and Rignot, E. (2012). Mapping of ice motion in antarctica using synthetic-aperture radar data. *Remote Sensing*, 4(9):2753–2767.

Nardi, L., Sorror, C., Badran, F., and Thiria, S. (2009). Yao: A software for variational data assimilation using numerical models. In *Computational Science and Its Applications – ICCSA 2009*, pages 621–636, Berlin, Heidelberg. Springer Berlin Heidelberg.

Nienow, P. W., Sole, A. J., Slater, D. A., and Cowton, T. R. (2017). Recent advances in our understanding of the role of meltwater in the greenland ice sheet system. *Current Climate Change Reports*, 3(4):330–344.

Nye, J. (1973). Water at the bed of a glacier. In *International Glaciological Society*, pages 189–194.

Nye, J. F. (1952). The mechanics of glacier flow. *Journal of Glaciology*, 2(12):82–93.

Nye, J. F. (1976). Water flow in glaciers: Jökulhlaups, tunnels and veins. *Journal of Glaciology*, 17(76):181–207.

Parizek, B. R. and Alley, R. B. (2004). Implications of increased greenland surface melt under global-warming scenarios: ice-sheet simulations. *Quaternary Science Reviews*, 23(9):1013–1027.

Pattyn, F. (2008). Investigating the stability of subglacial lakes with a full stokes ice-sheet model. *Journal of Glaciology*, 54(185):353–361.

Poinar, K., Dow, C. F., and Andrews, L. C. (2019). Long-term support of an active subglacial hydrologic system in southeast greenland by firn aquifers. *Geophysical Research Letters*, 46(9):4772–4781.

Pritchard, H. D., Arthern, R. J., Edwards, L. A., and Vaughan, D. G. (2009). Extensive dynamic thinning on the margins of the greenland and antarctic ice sheets. *Nature*, 461(7266):971–975.

Reist, A. (2005). Mathematical analysis and numerical simulation of the motion of a glacier.

Rignot, E., Jacobs, S., Mouginot, J., and Scheuchl, B. (2013). Ice-shelf melting around antarctica. *Science*, 341(6143):266–270.

Rignot, E., Mouginot, J., and Scheuchl, B. (2011). Ice Flow of the Antarctic Ice Sheet. *Science*, 333(6048):1427–1430.

Rignot, E., Mouginot, J., and Scheuchl, B. (2017). Measures insar-based antarctica ice velocity map, version 2 [data set]. boulder, colorado usa. nasa national snow and ice data center distributed active archive center. Accessed 06-10-2021.

Rignot, E., Mouginot, J., Scheuchl, B., and Jeong, S. (2022). Changes in antarctic ice sheet motion derived from satellite radar interferometry between 1995 and 2022. *Geophysical Research Letters*, 49(23):e2022GL100141.

Röthlisberger, H. (1972). Water pressure in intra- and subglacial channels. *Journal of Glaciology*, 11(62):177–203.

Röthlisberger, H. and Iken, A. (1981). Plucking as an effect of water-pressure variations at the glacier bed. *Annals of Glaciology*, 2:57–62.

Schoof, C. (2005). The effect of cavitation on glacier sliding. *Proceedings of the Royal Society. A, Mathematical, Physical, and Engineering Sciences*, 461(2055):609–627.

Schoof, C. (2010). Ice-sheet acceleration driven by melt supply variability. *Nature*, 468(7325):803–806.

Sergienko, O. V. and Hulbe, C. L. (2011). 'sticky spots' and subglacial lakes under ice streams of the siple coast, antarctica. *Annals of Glaciology*, 52(58):18–22.

Sergienko, O. V., MacAyeal, D. R., and Bindschadler, R. A. (2007). Causes of sudden, short-term changes in ice-stream surface elevation. *Geophysical Research Letters*, 34(L22):L22503.

Seroussi, H., Nowicki, S., Simon, E., Abe-Ouchi, A., Albrecht, T., Brondex, J., Cornford, S., Dumas, C., Gillet-Chaulet, F., Goelzer, H., Golledge, N. R., Gregory, J. M., Greve, R., Hoffman, M. J., Humbert, A., Huybrechts, P., Kleiner, T., Larour, E., Leguy, G., Lipscomb, W. H., Lowry, D., Mengel, M., Morlighem, M., Pattyn, F., Payne, A. J., Pollard, D., Price, S. F., Quiquet, A., Reerink, T. J., Reese, R., Rodehacke, C. B., Schlegel, N.-J., Shepherd, A., Sun, S., Sutter, J., Van Breedam, J., van de Wal, R. S. W., Winkelmann, R., and Zhang, T. (2019). initMIP-Antarctica: An ice sheet model initialization experiment of ISMIP6. *The Cryosphere*, 13(5):1441–1471.

Shiklomanov, I. A. (1993). *Water in crisis : a guide to the world's fresh water resources*. Oxford University Press, New York.

Shreve, R. L. (1972). Movement of water in glaciers. *Journal of Glaciology*, 11(62):205–214.

Siegfried, M. R., Fricker, H. A., Carter, S. P., and Tulaczyk, S. (2016). Episodic ice velocity fluctuations triggered by a subglacial flood in west antarctica. *Geophysical Research Letters*, 43(6):2640–2648.

Sommers, A., Rajaram, H., and Morlighem, M. (2018). Shakti: Subglacial hydrology and kinetic, transient interactions v1.0. *Geoscientific Model Development*, 11(7):2955–2974.

Stearns, L. A., Jezek, K. C., and Van Der Veen, C. (2005). Decadal-scale variations in ice flow along whillans ice stream and its tributaries, west antarctica. *Journal of Glaciology*, 51(172):147–157.

Stearns, L. A., Smith, B. E., and Hamilton, G. S. (2008). Increased flow speed on a large east antarctic outlet glacier caused by subglacial floods. *Nature Geoscience*, 1(12):827–831.

van de Wal, R. S. W., Boot, W., van den Broeke, M. R., Smeets, C. J. P. P., Reijmer, C. H., Donker, J. J. A., and Oerlemans, J. (2008). Large and rapid melt-induced velocity changes in the ablation zone of the greenland ice sheet. *Science*, 321(5885):111–113.

Van Der Veen, C., Stearns, L., Johnson, J., and Csatho, B. (2014). Flow dynamics of byrd glacier, east antarctica. *Journal of Glaciology*, 60(224):1053–1064.

van Wessem, J. M., van de Berg, W. J., and van den Broeke, M. R. (2023). Data set: Monthly averaged RACMO2.3p2 variables; Antarctica.

Verjans, V. and Robel, A. (2024). Accelerating subglacial hydrology for ice sheet models with deep learning methods. *Geophysical Research Letters*, 51(2):e2023GL105281.

Walder, J. and Hallet, B. (1979). Geometry of former subglacial water channels and cavities. *Journal of Glaciology*, 23(89):335–346.

Walder, J. S. (1982). Stability of sheet flow of water beneath temperate glaciers and implications for glacier surging. *Journal of Glaciology*, 28(99):273–293.

Walder, J. S. (1986). Hydraulics of subglacial cavities. *Journal of Glaciology*, 32(112):439–445.

Weertman, J. (1957). On the sliding of glaciers. *Journal of Glaciology*, 3(21):33–38.

Weertman, J. (1972). General theory of water flow at the base of a glacier or ice sheet. *Reviews of Geophysics*, 10(1):287–333.

Werder, M. A., Hewitt, I. J., Schoof, C. G., and Flowers, G. E. (2013). Modeling channelized and distributed subglacial drainage in two dimensions. *Journal of Geophysical Research*, 118:2140–2158.

Winberry, J. P., Anandakrishnan, S., and Smith, A. M. (2007). Changes in speed near the onset of bindschadler ice stream, west antarctica. *Annals of Glaciology*, 46:83–86.

Yu, H., Rignot, E., Seroussi, H., and Morlighem, M. (2018). Retreat of Thwaites Glacier, West Antarctica, over the next 100 years using various ice flow models, ice shelf melt scenarios and basal friction laws. *The Cryosphere*, 12(12):3861–3876.